# Two-Phase Flow, Three-Dimensional Approach for Saltating Particles near the Bed at Finite Reynolds Numbers

By

PATRICIO ALEJANDRO MORENO CASAS
B.S. (Universidad de Santiago de Chile, Santiago, Chile) 2002
M.Sc. (University of Tennessee, Knoxville) 2004

DISSERTATION

Submitted in partial satisfaction of the requirements for the degree of

DOCTOR OF PHILOSOPHY

in

Civil and Environmental Engineering

in the

OFFICE OF GRADUATE STUDIES

of the

UNIVERSITY OF CALIFORNIA

DAVIS

Approved:

_____________________________________

Fabian A. Bombardelli, Chair

_____________________________________

Robert D. Guy

_____________________________________

David H. Schoellhamer

Committee in Charge

2014

# ABSTRACT

Recent theoretical and numerical models for the motion of saltating particles close to stream beds (mainly two-dimensional) can be analyzed by three sub-models: a) a set of equations describing the particle “free flight,” b) a sub-model to calculate the post-collision particle velocity, and c) a mathematical representation of the bed roughness. In this work, a new three-dimensional (3D), theoretical/numerical model for bed-load motion is presented, discussing in particular different and novel versions of the above sub-models. Special focus is given to the assessment and analysis of generalized sub-models for the post-collision velocities and the bed-roughness representation. The free-flight sub-model includes the effect of several forces over the particle translation and also addresses the particle rotation. The post-collision velocity and rotation sub-model features the conservation of linear and angular momentum during the rebound, and it enables a straightforward extension to inter-particle collisions. An extension to 3D of the bed roughness representation is introduced by using geometric considerations between the moving particle and the bed, together with stochastic parameters. Simulation results are compared with results of other bed-representation sub-models found in the literature and with data, in terms of statistically meaningful parameters. It is shown that the proposed model is in good agreement with experimental data in the sand size range. An assessment of the importance of forces in the description of particle motion is also presented.

The importance of particle-particle collisions in sediment saltation in the bed-load layer is also analyzed herein by means of numerical simulation. The particle saltation theoretical/numerical model follows a Lagrangian approach, and addresses the motion of sediment particles in an open channel flow described by a logarithmic velocity profile. The model is validated with experimental data obtained from the literature. In order to evaluate the

importance of the phenomenon, simulations with and without particle-particle collisions were carried out. Results for two different sediment concentrations are presented, namely 0.13% and 2.33%. For each concentration of particles, three different flow intensities were considered, and trajectories of two different particle sizes, within the sand range, were computed. Changes in particle rotation, particle velocity, and angle of trajectory before and after particle-particle collisions appear to be relatively important at lower shear stresses, whereas they decrease in significance with increasing flow intensities. Analyses of the evolution in time of the second order moment of particle location suggest that inter-particle collisions introduce transverse diffusion in saltating particles.

When numerically integrating the equation describing the motion of a particle in a carrier fluid, the computation of the Basset (history) force becomes by far the most expensive and cumbersome, as opposed to forces such as drag, virtual mass, lift, buoyancy and Magnus. The expression representing the Basset force constitutes an integro-differential term whose standard integrand is singular when the upper integration limit is enforced. These shortcomings have led some researchers to disregard the contribution of the Basset force to the total force, even in those cases where it may yield to important errors in the determination of particle trajectories. This work is devoted to review four recent contributions associated with the computation of the Basset force, and to compare their proposals to diminish the inherent problems of the term integration. All papers, except one, use variants of a window-based approach; the most recent contribution, in turn, employs a specialized quadrature to increase the accuracy of the computation. Besides discussing the nature of the particular techniques utilized to overcome the singularity problem of the standard kernel, an analysis was carried out to compare CPU computation times, rates of convergence and accuracy of the approximations versus a known analytic solution. All methods provide sound solutions to the issues associated with the computation of the Basset force; further a road map to select the best solution for each given problem is provided.

# TABLE OF CONTENTS

# LIST OF FIGURES

# LIST OF TABLES

# ACKNOWLEDGEMENTS

I would like to thank the guidance, dedication and support of Professor Fabian Bombardelli. From what he has shown me, I have built the foundation of what is to come, and future looks bright. I also want to thank professors Robert Guy and David Schoellhamer, who have helped me to achieve this goal of becoming a Doctor.

I also want to thank my parents, Marcela and Ricardo, my brothers, Felipe and Matias, and of course my little sister, Macarena, I have you all in my heart.

Most importantly, I want to show my gratitude to my little family. Carolina and Maximiliano. Everything I am, everything I do is because of you. You are the light of my life.

# CHAPTER 1

# INTRODUCTION

## 1.1. MOTIVATION AND PROBLEM STATEMENT

Sediment transport is a very important phenomenon with practical implications regarding water-quality in estuaries and rivers, and management, protection and sustainability of infrastructure. It affects natural streams, oceans, lakes, and industrial activities. Scour and erosion may cause serious problems with transportation infrastructure such as roads, highways and bridges. Scour and erosion are the most common cause of bridge failure during floods (Julien, 2010). Sedimentation of particles in waterways, harbors, and ports reduces the effective water depth for navigation, and it decreases the storage capacity of reservoirs. Sediment can be considered as a pollutant itself, but it also acts as carrier and repository of pollutants (heavy metals, radioactive waste, pesticides, pathogens, and in general organic and non-organic compounds), rising environmental water-quality inconveniences due to transport and resuspension (Julien, 2010). The control and management of sediment in natural environments and in industrial applications is costly (González, 2008) and it demands time and effort from industry, local and federal administrations around the world. Unfortunately, sediment transport processes are not completely understood. Thus, a better understanding of sediment transport processes is of great importance in the global water system (Takeuchi, 2004).

The transport of sediment by water varies widely between fine clay to large boulders (García, 2008). The initiation of motion of sediment particles is parametrized to occur when the shear stress of the flow applied to motionless bed particles is larger than their critical shear stress. Sediment transport is usually categorized as suspended load and bed-load (Greimann et al., 1999; García, 2008). Commonly, sand and gravel move near the bed (bed-load), while silt and clays move away from the bed (suspended load); the bed-load layer confines to a few grain diameters (Julien, 2010). At low shear stresses; the motion of particles are mainly described as sliding and rolling; however, with a small increase of shear stress particles will start to jump and collide with the bottom wall, in an unsuspended motion close to the bed (García, 2008). The latter mode is called saltation, and it is the most common type of bed-load motion until shear stress magnitudes reach a limit where grain flow (also known as sheet flow) dominates (García, 2008).

Saltation has been the subject of experimental and numerical studies for several decades. Particular interest has been given to saltation of sand particles due to wind erosion on Earth, sand transport on Mars, snowdrift and bed-load particles in water flows. Insightful information from laboratory experiments of particle saltation in water streams have been generated over the last decades by Lee (1993), Hu and Hui (1996), Niño et al. (1994a), Lee and Hsu (1994), Niño and García (1998a), Lee et al. (2006), and Wang et al. (2004).

Although experimental information has been instrumental in understanding the mechanics of particle saltation, to the best of our knowledge no experimental comprehensive data of particle motion in a turbulent flow has been published to date, due to the difficulty of performing such task with today's measurement technologies. Only empirical expressions of bulk bed load transport rates are available, with their inherit limitations to specific ranges of flow and particle characteristics.

Numerical simulations of sediment transport as bedload have been developed over time with relative success (Wiberg and Smith, 1985; Niño and García, 1994; Lee and Hsu, 1994; Schmeeckle and Nelson, 2003; Lukerchenko et al., 2006; Lee et al., 2006; González, 2008;

Bombardelli et al., 2008; Lukerchenko et al., 2009a,b; Loth and Dorgan, 2009; Bialik et al., 2012; Moreno and Bombardelli, 2012), mainly focusing on saltation statistics such as jump height and length (Fig. 1.1). Yet their accuracy is still limited (Duan et al., 2004) due to the lack of knowledge of the interaction between the carrier flow and the moving particles at small scales (Hanratty et al., 2003). Thus, further advances in this subject are needed in order to better understand the physics and complex processes at a micro-scale level.

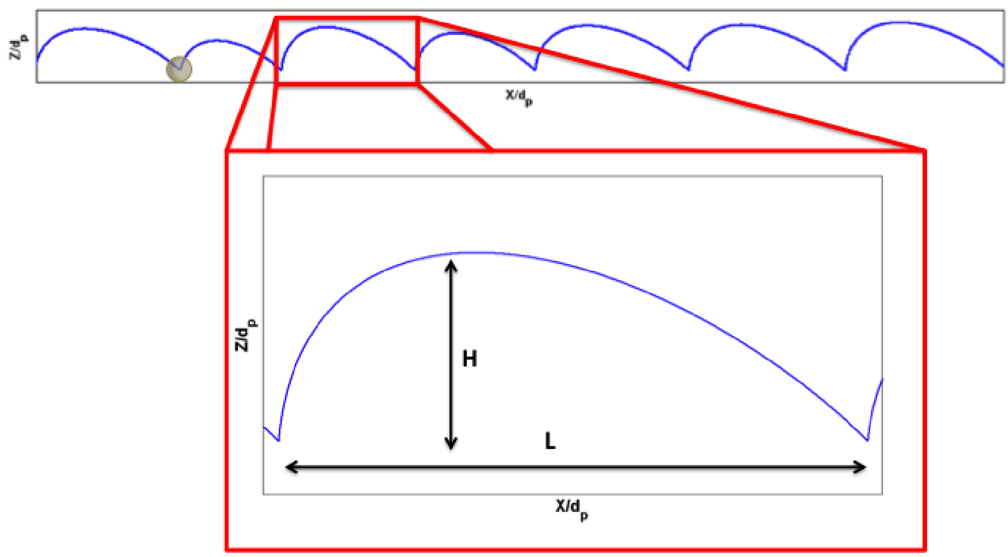


**Figure 1-1: Particle saltation trajectory and statistics. *H* represents the jump height, and *L* the jump length. The wall-normal and stream-wise axes are normalized by the particle diameter $d_p$.**

The first particle saltation models were two dimensional in nature, although saltation is essentially a three dimensional (3D) mechanism (Lukerchenko et al., 2009a); therefore, a better understanding and prediction of the phenomenon could be in principle attained using 3D models. All model approaches mentioned herein consider the saltation phenomenon as an Eulerian-Lagrangian problem, where the flow has an Eulerian treatment as a continuum (Eulerian), and the particles are tracked in a Lagrangian way through the application of Newton's second law (linear momentum equation). Some models have considered all three dimensions (Schmeeckle and Nelson, 2003; Lee et al., 2006; Harada and Gotoh, 2006; González, 2008; Lukerchenko et al., 2009a; Bialik et al., 2012). Many of the models neglect the contribution of the Basset force, mainly due to the complications present when trying to compute the Basset term. The Basset force addresses the delay in the development of the boundary layer in a particle moving through a fluid due to the changes in relative acceleration over time, and it has been neglected due to the complications regarding its computation (Crowe et al., 2011). Armenio and Fiorotto (2001) found that the Basset force is important when the particle Reynolds number ($\mathrm{Re}_p = w_s\, a / \nu$, where $w_s$ represents the particle fall (limit) velocity, $a$ is the radius of the particle and $\nu$ depicts the kinematic viscosity of the fluid) is of the order or smaller than 1, for a large range of density ratios. Despite this finding, many researchers still disregard the contribution of the Basset force.

Most of the previous models in 2 and 3D use an averaged velocity representation of the flow, instead of solving the actual flow with its time dependance. This velocity representation is known as the logarithmic law of the wall (Kundu and Cohen, 2008). An attempt to include turbulent fluctuations of the flow has been suggested by Schmeeckle and Nelson (2003), Gonzáles (2008), Bialik (2011), Moreno et al. (2011), and Bialik et al. (2012). Schmeeckle and Nelson (2003) included turbulence fluctuations, but through empirical relations obtained experimentally, while Bialik (2011) and Bialik et al. (2012) applied spectral functions to account for velocity fluctuation. Thus, to achieve more realistic predictions, numerical simulations of particles saltating near the bed should consider a general 3D turbulent flow representation that mimics the natural conditions of open-channel flows (González, 2008). Several levels of coupling can be applied to the numerical simulations: one-way coupling, where the particles' effect on the flow dynamics is negligible; two-way coupling, where particles do affect the flow dynamics; three-way coupling, where there are inter-particle hydrodynamic effects; and four-way coupling, where inter-particle collisions are important. González (2008) pioneered the application of a fully turbulent flow to the saltation motion of particles, yet using one-way coupling. One-way coupling neglects the influence of particles in the hydrodynamics of the flow, and therefore the modification of turbulence due to the presence of particles is not accounted for.

Particle-particle collisions (four-way coupling), also known as inter-particle collisions, are another important aspect on particle saltation. The importance of this type of interaction will depend on the concentration of sediments moving as bedload, the intensity of the flow, the size of the particles, their shape and density. For the case of sands saltating near a bed channel, the first attempt to analyze its importance was carried out by Bialik (2011). However, the latter work was only 2D and particle rotation was neglected.

The work presented herein represents the first stage towards a 3D, two and four-way coupling, fully turbulent Eulerian-Lagrangian model, where the first stage would be to validate the Lagrangian particle tracking model regarding jump characteristics from experimental values (in the sands range) and particle diffusion in the stream and the span-wise direction.

## 1.2. RESEARCH DESCRIPTION AND OBJECTIVES

The main objective of this study is to gain a fundamental understanding of the micro scale mechanics of saltating particles, their interaction with other particles, pertaining to dilute mixtures (concentrations of less than 5% by volume approximately) in open channel flows. From this, we aim at contributing to a more complete theoretical/numerical framework for sediment bed-load motion. From the previous statement, a series of specific goals can be enumerated as follows:

1. Develop and validate a 3D Eulerian-Lagrangian model to simulate particle saltation near the bed at high Re.
2. Gain more understanding of particle saltation at different flow intensities.
3. Analyze the effects on particle scattering due to particle collision with the bed and particle-particle interaction.
4. Study and compare the recent advancements on the computation of the Basset force for future upgrades of the particle saltation model.

The main outcome of this study lies on the detailed analysis of the physical mechanisms occurring at micro scales in saltating particles subjected to an averaged turbulent water flows in a open channel, as an intermediate step to achieve two-way coupling between the turbulent flow and the saltating particles.

## 1.3. DISSERTATION PLAN

This dissertation is composed of six chapters, where a literature review is presented, followed by a series of three papers, and ending with the conclusions chapter. In the paragraphs below a description of each of these five chapters is presented.

Chapter 2 presents a literature review of the existing particle saltation models, available wall-particle and particle-particle collision algorithms, and bed roughness representations. Treatment of the flow as part of the two-phase approach is also discussed. Finally, the most recent experimental data available for validation is presented.

Chapter 3 is a paper submitted to *Hydrological Processes*. The paper describes the three-dimensional two-phase flow generalize algorithm for particle saltation near the bed using a logarithmic velocity profile, discussing the different sub-models used to emulate the particle "free flight" and collisions with the bed, including descriptions of the particle angular and linear velocities for every time step. An assessment of existing and novel sub-models for bed representation is carried out. A validation of the particle saltation model is accomplished by comparing simulation results with experimental data for two different particle sizes within the sand range. Finally validation for particle scattering in the stream and span-wise directions is achieved using a well-known conceptual model for diffusion of bed-load particles.

Chapter 4 is a paper published in *Acta Geophysyca* (Moreno and Bombardelli, 2012) that focuses on the importance of particle-particle collisions in sediment saltation using a logarithmic velocity profile. The model is first validated with experimental data. In order to evaluate the inter-particle collisions, simulations with and without considering collisions among sediment grains are presented for two different particle sizes (sands), two different initial particle concentrations, and three flow intensities. At the end of the analyses the evolution in time of the second-order moment of particle position is studied to establish the contribution of particle-particle collisions as a source of particle scattering.

Chapter 5 presents a comparison of the most recent approaches to compute the Basset history force. In this chapter an analysis of the problematic related to the numerical integration of the Basset integro-differential term are discussed, i.e., singularity of the kernel, computational time and memory, and accuracy in time. The comparison of the recent methodologies is carried out using a test integral with a known solution.

Although chapters 3 to 5 have their own conclusion section, the overall conclusion for the whole dissertation is presented in Chapter 6. In this final chapter a summary of the contributions of this study and guidelines for the future work are presented.

## 1.4 LIST OF PUBLICATIONS

Specific findings of this thesis have been communicated through a book chapter, posters and papers published in or submitted to several international proceedings and journals.

**Book Chapters**

- Bombardelli, F.A., and P.A. Moreno (2012), “Exchange at the bed sediments-water column interface”, Fluid mechanics of environmental interfaces, Second Edition, C. Gualtieri, and D.T. Mihailovic eds., Taylor & Francis, London, UK, Chap. 8, pages 221-253.

**Paper, Abstracts and Posters in Conferences**

- Bombardelli, F.A., A.E. González, and P.A. Moreno (2010), Numerical simulation of spheres moving and colliding close to bed streams, with a complete characterization of turbulence. In: Proceedings of River Flow 2010, Braunschweig, Germany, 777-784.
- Moreno, P.A., F.A. Bombardelli, A.E. González, and V.M. Calo (2011), Three dimensional model for particle saltation close to stream beds, including a detailed description of the particle interaction with turbulence and inter-particle collisions. In: Proceedings of World Environmental and Water Resources Congress ASCE 2011, Palm Springs, CA, USA, 2075-2084.
- Moreno, P.A., and F.A. Bombardelli (2012), 3D Lagrangian model of particle saltation in an open channel flow with emphasis on particle-particle collisions. In: Poster presented at 2012 Fall Meeting, AGU, San Francisco, CA, USA.

- Moreno, P.A., and F.A. Bombardelli (2013), Analysis of particle diffusion due to inter-particle collisions in bed-load motion by means of a 3D numerical model. In: Proceedings of International Association of Hydro-Environment Engineering and Research (IAHR), Beijing, China.
- Moreno-Casas, P.A., and F.A. Bombardelli (2014), Computation of the particle Basset force: Comparison of recently published techniques. In: Proceedings of the Fourteen Pan-American Congress of Applied Mechanics (PACAM), Santiago, Chile.

**Papers Published, Submitted or to be Submitted to International Journals**

- Moreno, P.A., and F.A. Bombardelli (2012), 3D numerical simulation of particle-particle collisions in saltation mode near stream beds, Acta Geophysica, 60: 1661-1688.
- Bombardelli, F.A., P.A. Moreno-Casas, A.E. González, and R. Moniz (2014), Generalized algorithms for particle motion and collision with stream beds, *submitted to Hydrological Processess*, 2014.

# CHAPTER 2

# LITERATURE REVIEW

In this chapter a review on what is available in literature regarding Lagrangian particle saltation models is presented. Previous works applying the two-phase flow theory in two and three dimensions are summarized and compared. All models presented here treat the flow using an Eulerian description, while tracking the particles Lagrangianly. Differences in the application of modeled forces, the treatment of the flow, particle size, treatment of the wall collisions and the consideration of particle-particle collisions are discussed. The experimental data available for validation of the models are also examined.

## 2.1. PARTICLE SALTATION MODELS

Particle saltation motion modeled as a two-phase flow implies the interaction of a carrier phase, in this case water, with a disperse phase, sediment particles. The saltation models that will be discussed herein treat the flow or the carrier phase in an Eulerian framework, i.e., the analysis of the motion of the fluid flow focuses on a specific location or window in space through which the fluid travels as time passes (Kundu and Cohen, 2008). At the same time the saltating sediment particles will be treated in a Langrangian framework, i.e., each particle will be followed individually as it moves through space and time (Kundu and Cohen, 2008). A two-phase flow approach requires separate equations describing the motion of the carrier phase and the disperse phase.

For a rigorous treatment of the computational simulation of particle saltation, one would have to establish a very fine computational mesh, small enough to solve the Navier-Stokes equations at the surface of each saltating particle. However, this task is impossible to achieve given the limited capabilities of today's computers to solve the Navier-Stokes equations for high Reynolds numbers. Therefore a different approach must be taken. An alternative method would be to use a point-particle approach, which will allow the simulation of thousands or millions of particles at high Reynolds numbers (Prosperetti and Tryggvason, 2007). The point-particle approach treats each sediment grain as points while the exchange of momentum between the particle and the surrounding fluid is modeled, rather than solved directly. Point-particle models generally assume a flow that is incompressible, and moving particles that do not experience any type of mass or energy exchange at the grain surface (Prosperety and Tryggvason, 2007). Thus, for the dispersed phase only the equations for the conservation of momentum need to be established.

A particle moving in saltation mode is constantly hopping and colliding with the bed. Between collisions the particle moves due to its interaction with the hydrodynamic forces exerted by the flow that are counteracted by the action of gravity trying to pull the moving grains down towards the stream bed. To characterize this stage of the particle motion, an equation representing the hydrodynamic forces and the action of gravity needs to be considered. This equation should incorporate all forces that might be important in the saltation process. When the particle collides with the bed or another particle, the momentum exchange between the particle and the bed or between particles should be computed. All these aspects, together with the treatment of the flow, are reviewed in this chapter for existing saltation models, in two and three dimensions.

## 2.2. ASSESSMENT OF FORCES CONSIDERED IN SALTATION MODELS

In order to describe the motion of a saltating particle, Newton's Second Law is applied. This law states that the changes in time of the particle momentum will be determined by the sum of all the external forces acting on the grain. Three types of forces affect the moving particle: gravity, shear stress and pressure forces; the latter two inflicted by the surrounding fluid on the surface of the particle. The gravity force is included in the linear momentum equation of a saltating particle as submerged gravity, while the shear stress and pressure forces are represented by: the quasi-steady drag force, the unsteady drag or Basset force, lift forces, and the virtual or added mass force. The Basset force, also known as the history force, addresses the temporal delay in the development of the boundary layer surrounding the particle as a consequence of changes in the relative velocity (Crowe et al., 2011). The lift forces can be decomposed in to two parts depending of the source of the lifting effect: the gradients of velocity or the particle rotation. The type of lift caused by the gradients of velocity will be called lift force hereafter, whereas the type of lift caused by the particle rotation is known as the Magnus force. The virtual or added mass force represents the work exerted by the particle to accelerate the surrounding fluid while moving (Crowe et al., 2011). Several authors have ignored the contribution of some of these forces. Table 2-1 summarizes which forces have been incorporated on different saltation models.

**Table 2-1: Summary of saltation models for particle motion in two (2D) and three (3D) dimensions (dim). Assessment of flow representation, forces, particle diameter ($d_p$), material, consideration of particle-particle collisions (PP collisions) and particle rotation.**

| Author/dim | Year | Flow representation | Forces | $d_p$ (mm) | Particle Material | PP collisions | Rotation |
|---|---|---|---|---|---|---|---|
| Sekine & Kikkawa 3D | 1992 | Logarithmic expression | dr, sw, vm | 0.3-0.6 | Natural sediment | No | No |
| Lee & Hsu 2D | 1994 | Logarithmic expression | dr, sw, vm, lf, Mg | 1.36-2.47 | Natural sediment | No | Yes |
| Niño & García 2D | 1994 | Logarithmic expression | dr, sw, vm, lf, Bs, Mg | 15-31 | Natural sediment | No | No |
| Niño & García 2D | 1998b | Logarithmic expression | dr, sw, vm, lf, Bs, Mg | 0.5-0.8 | Natural sediment | No | Yes (empirical) |
| Lee et al. 2D | 2000 | Logarithmic expression | dr, sw, lf | 6 | Natural sediment | No | No |
| Yeganeh et al. 2D | 2000 | K-e | dr, sw, vm | 5 | Glass beads | No | Yes |
| Schmeeckle and Nelson 3D | 2003 | Experimental measurements | dr, sw, vm | 2-7 | Natural sediment | No | Yes |
| Shabani et al. 3D | 2005 | Logarithmic expression | dr, sw, vm | 0.05 | Natural sediment | Yes (sfm) | Yes |
| Harada & Gotoh 3D | 2006 | Logarithmic expression + Monte Carlo Method for turbulence | dr, sw, vm | Sand range | Natural sediment | Yes (sfm) | Yes |
| Lee et al. 2D | 2006 | Logarithmic expression | dr, sw, lf | 0.039-0.068 | Natural sediment | No | No |
| Lukerchenko et al. 2D | 2006 | Logarithmic expression | dr, sw, vm, lf, Bs, Mg | 15 | Natural sediment | No | Yes |
| Lukerchenko et al. 3D | 2009a | Logarithmic expression | dr, sw, vm, lf, Bs, Mg | 0.5 - 6 | Natural sediment | No | Yes |
| Yeganeh et al. 3D | 2009 | Logarithmic expression + 3D turbulent intensities | dr, sw, vm | 2 | Natural sediment | Yes (sfm) | Yes |
| Bialik 2D | 2011 | 2D turbulence generator | dr, sw, vm, lf, Bs | 0.53 -1.36 | Natural sediment | Yes (hsm) | No |
| Bialik et al. 3D | 2012 | 3D turbulence generator | dr, sw, vm, lf | 2 | Natural sediment | No | No |

Where: sfm=soft sphere model, hsm=hard sphere model, $d_p$=particle diameter, dr=drag, sw=submerged weight, vm=virtual mass, lf=lift, Bs=Basset, and Mg=Magnus.

Most of the models presented in Table 2.1 consider drag, submerged weight and virtual mass as the only forces acting on the saltating particle. Basset and Magnus forces are usually neglected, sometimes without solid justification. Although many works have disregarded the Basset force in their saltation models (Sekine and Kikkawa, 1992; Le and Hsu, 1994; Lee et al., 2000; Yeganeh et al., 2000; Schmeeckle and Nelson, 2003, Shabani et al., 2005; Harada and Gotoh, 2006; Lee et al., 2006; Bialik et al., 2012), there is evidence (Niño and García, 1994) that the Basset force is important for sands up to $R_p = 100$ (where $R_p = \left(R\, g\, d_p^3\right)^{0.5} / \nu$ is the explicit particle Reynolds number, $R$ is $\left(\rho_s / \rho\right) - 1$, $\rho$ and $\rho_s$ denote fluid and particle density, respectively, $g$ is the acceleration of gravity, and $\nu$ is the kinematic viscosity of water). When the Basset force is disregarded for sand particles, the characteristics of the jump (height and length) are drastically under predicted (Fig. 2 in Niño and García 1998b) and may cause large errors in the overall simulation. Mordant and Pintot (2000) also found that the Basset force need to be included in particle tracking models for $\mathbf{Re}_p$ smaller than 4,000 (where $\mathrm{Re}_p = w_s\, d_p / \nu$ is the particle Reynolds number, $w_S$ is the particle fall (limit) velocity). Armenio and Fiorotto (2001) also found that the Basset force is important for particles with $\mathrm{Re}_p$ equal or smaller than 1, for a large range of density radios. The Basset force is usually disregarded since is by far the most expensive (regarding computational time and memory) force to compute.

## 2.3. PARTICLE-WALL COLLISIONS

The numerical study of particle collisions with the wall is generally separated into two aspects: a) the particle rebound, and b) the representation of the bed roughness. A particle rebound sub-model allows the computation of the post-collision angular and linear velocities of the saltating particle from the angular and linear velocities right before the collision with the wall. Added to this, the loss of energy during the particle semi-elastic collision is taken into account using restitution and friction coefficients. The representation of the irregularities embedded in the bed of any natural stream is considered through random and geometrical expressions. The latter allows variability in the particle jump heights and lengths, as well as in the overall grain scattering.

Several works have presented expressions to compute the post-collision velocities (Matsumoto and Saito, 1970a; Tsujimoto and Nakagawa, 1983; Tsuji et al., 1985; Niño and García, 1994; Lukerchenko et al., 2009a). From these, the equations proposed by Tsuji et al. (1985) and Niño and García (1994) have been widely used. While the work by Tsuji et al. allows for the computation of the post-collision velocities in the three dimensions, the expressions proposed by Niño and García need to be extended from two to three dimensions. In addition, the beauty of the equations from Tsuji et al. is that they could be easily extended to account for collisions among particles.

One way to represent the bed roughness and the irregular shape of the bed particles is to completely describe the complexities and details of the bed in the model (particle shapes and bed geometry), as done by Sekine and Kikkawa (1992) and Scotti (2006). However this approach is computationally expensive. On the other hand, it is possible to avoid the complete description of the bed by incorporating the randomness of the bed roughness right at the moment of collision

(Tsuji et al., 1985; Sommerfeld, 1992; Tsuji et al., 1987; Niño and García, 1992). Tsuji et al. (1987) and Sommerfeld (1992) characterized the irregularities of the bed using a virtual wall, with an inclination that would randomly change at each collision. In Tsuji et al.'s work the inclination was normally distributed between -4º and 4º, while Sommerfeld assumed a uniform distribution with the same range of angles. Niño and García (1992) presented a geometric expression that related the incidence angle of collision of the saltating particle, with the angle formed by the tangent at the collision point at the bed particle, and a parameter $r$ that was randomly computed at every collision (see section 3.2.3 for definition of the parameter $r$).

## 2.4. PARTICLE-PARTICLE COLLISIONS

For particle-particle collisions two models are generally considered: a) the hard sphere model, and b) the soft sphere model. The hard sphere model considers the linear and angular momentum exchanges between colliding particles relating pre and post-collision velocities explicitly using restitution and friction coefficients (Crowe et al., 2011). The hard sphere model contemplates only collisions between two particles (binary collisions), which is a good approach for low particle concentrations. The soft sphere approach uses mechanical elements, such as springs to model multi-particle collisions, to estimate the post-collision velocities. It is not limited to binary collisions only, and therefore it becomes very useful when computing particle motion at higher concentrations. However, the computation time is much longer than the hard sphere model (Crowe et al., 2011).

The hard sphere model has been used in many gas-solid applications (Sommerfeld, 1992, 2003; Lun and Liu, 1996; Yamamoto et al., 2001; Kartushinsky and Michaelides, 2004; Ten Cate et al., 2004), and in two particle saltation models (Bialik, 2011; Moreno and Bombardelli, 2012).

For higher concentrations (sheet flow for example, where a highly concentrated layer or sheet of particles is transported) the soft sphere approach has been a useful tool to include particle-particle collisions in the model (Yeganeh et al., 2000; Schabani et al., 2005; Harada and Gotoh, 2006; Yeganeh et al., 2009). Although these works have included particle saltation in their bed-load models, they primarily focused in sheet flow. To the best of the author's knowledge, the only studies of particles exclusively moving in saltation mode that included particle-particle collisions are Bialik (2011), which is 2D, and the one presented in this thesis by Moreno and Bombardelli (2012), which is 3D.

Multi-particle simulations can be computationally expensive, depending on the number of particles simulated, the forces considered in the particle momentum equations, and how the flow is represented. Thus, considering particle-particle collisions may cause an extra computational burden to the overall simulation. Most of the particle saltation models have disregarded this type of collisions without clear-cut evidence (see Table 2-1), assuming that grains are dispersed enough (very low concentration) that the effect of particle-particle collisions is negligible. Therefore, studies to assess the importance of the contribution of collisions among particles to the overall sediment transport as saltation are required. In Chapter 4 this task is undertaken using the hard sphere model through the extension of the Tsuji et al. (1985) rebound algorithm (also used for collisions with the bed) as presented by Crowe et al. (2011).

## 2.5. REPRESENTATION OF THE FLOW

Most saltation models treat the flow as a logarithmic velocity profile, also known as the law of the wall (see Table 2-1). The law of the wall is an approximation to the average behavior of turbulence in open channels. This is a unidirectional steady-state representation of the flow (stream-wise direction only) that neglects the fluctuations of velocities in all directions.

Therefore, the interactions between turbulence and sediments, and vice versa, are disregarded. Consequently, to improve the prediction capability of numerical simulations for bed-load transport, it is necessary to provide a velocity field capable of reproducing the turbulence characteristic of natural open-channel flows (González, 2008). Some attempts to incorporate the effects of turbulence in saltation models have been presented by some authors (Yeganeh et al., 2000; Schmeeckle and Nelson, 2003; Harada and Gotoh, 2006; Yeganeh et al., 2009; Bialik, 2011; Bialik et al., 2012). However some of them are 2D, others use a mixture of the logarithmic profile and terms for turbulent intensities in the three directions, the K-ε closure model, turbulence generators that model a turbulent flow using the Monte Carlo method, and finally the use of instantaneous velocities in the three directions obtained from near-bed experimental measurements. So far no Large Eddy Simulation (LES) or Direct Numerical Simulation (DNS) approach has been carried out to solve the flow (for high Reynolds numbers) at the same time as the particle trajectories are being computed by the saltation model, in what is called a two-way coupled approach.

## 2.6. EXPERIMENTAL DATA FOR VALIDATION

The most recent experimental works regarding particle saltation are shown in Table 3-2, in Chapter 3. Therein, the works by Niño et al. (1994), Lee (1993), Lee and Hsu (1994), Niño and García (1998a,b) and Lee et al. (2006) are summarized and compared for: particle diameter, number of jumps, shear velocity (as a measurement of flow intensity), and jump statistics.

The most common properties presented by experimental works are the averaged jump height ($H$), length ($L$) and particle velocity in the stream-wise direction ($\bar{u}_p$). Only two of the experimental works measured the averaged span-wise particle rotation (or angular velocity).

Besides the average (mean) values, some of the publications give the standard deviation of the jump statistics. The experiments were carried out for sands ( $d_p$= 0.0625 – 2 mm) and gravels ( $d_p$= 2 – 64 mm), which are the most common type of sediment transported in saltation mode in natural streams (García, 2008).

Four sets of values for the restitution ( $e$ ) and friction ( $f$ ) coefficients (see Chapter 3 for definition) have been gathered for the present thesis: a) Niño and García (1998a), b) Schmeeckle et al. (2001), c) Tsuji et al. (1987), and d) Shen et al. (1989). Table 3-3, in Chapter 3, shows all four data sets. The values for Niño and García and Schmeeckle et al. were obtained from experiments in turbulent channels with natural sediments. Tsuji et al. considered polystyrene particles moving in a gas flow, and Shen et al. obtained the friction and restitution coefficients for non-spherical particles.

# CHAPTER 3

# GENERALIZED ALGORITHMS FOR PARTICLE MOTION AND COLLISION WITH STREAM BEDS

## 3.1. INTRODUCTION

Collisions of particles with a rigid - or semi rigid - wall occur in many natural and man-made processes, ranging from “saltation” of sand grains in deserts on Earth and the motion of sand dunes on Mars (Thorne et al., 1988; Sagan and Bagnold, 1975; White, 1982; Iversen and White, 1982) to particle-laden flows in pipes (Sommerfeld, 1992). In addition to the above airflows, these collisions become extremely important in the description of the transport of sediment particles as bed-load in streams.

Close to the bottom of open channels, the sediment particles may move in various modes such as sliding, rolling and saltating (Francis, 1973; Abbott and Francis, 1977). According to observations by different authors, the percentages of the total number of particles moving in each mode depend upon the particle size, $d_p$, and the shear stress, expressed through the Shields parameter $\tau_* = \tau_0 / \left[ \left( \rho_s - \rho \right) g \, d_p \right]$, where $\tau_0$ corresponds to the bed shear stress, $\rho_S$ and $\rho$ denote the density of the sediment and water, respectively, and $g$ is the acceleration of gravity. As $\tau_*$ increases, the amount of particles sliding and rolling drastically lessens, while the fraction of particles in saltation mode increases (Hu and Hui, 1996). Since $\tau_*$ is important in most natural conditions, saltation is considered to be the main form of bed-load motion in streams (Einstein, 1950; Sekine and Kikkawa, 1992; Lee et al., 2000; García, 2008).

The saltation motion can be analyzed via two main separate stages: 1) the “free flight” of the particle through the flow field, away from the wall, and 2) the collision of the particle with the bed. In the first stage, the particle trajectory is defined by the interplay of diverse hydrodynamic forces acting on the saltating grain. Sub-models for this stage have been based on the momentum equation (Newton's second law; Crowe et al., 2011) for the particle, and have been extensively studied by several researchers in the context of particles moving in boundary layers in general, and particles moving close to streambeds in particular (Maxey and Riley, 1983; Wiberg and Smith, 1985; Auton et al., 1988; Mei et al., 1991; Niño and García, 1994; Lee and Hsu, 1994; Schmeeckle and Nelson, 2003; Lukerchenko et al., 2006; Lee et al., 2006; González et al., 2006; González et al., 2007; González, 2008; Bombardelli et al., 2008; Lukerchenko et al., 2009a,b; Loth and Dorgan, 2009; Bialik et al., 2012; Moreno and Bombardelli, 2012). From a physical standpoint, there seems to exist a consensus in the scientific community in that models of this type offer a satisfactory description of particle trajectories. Loth and Dorgan (2009), Lukerchenko (2010) and Bombardelli and Moreno (2012) discussed the nature of certain expressions for the forces, and reviewed ways to parameterize the coefficients embedded in the equations. Most sub-models refer to motions in two spatial dimensions (2D); however, a few three-dimensional (3D) models have been presented recently (Schmeeckle and Nelson, 2003; Lee et al., 2006; Harada and Gotoh, 2006; Lukerchenko et al., 2009a, Bialik et al., 2012 and Moreno and Bombardelli, 2012).

The second stage relates to the process whereby the particle hits the bed and eventually rebounds. This stage can in turn be mathematically described through two sub-models: a) a rebound sub-model, and b) a bed-representation sub-model. (Although this classification has not been established in previous papers, the authors believe it helps enormously in understanding the diverse models.) Using equations for the exchange of momentum and energy during the collision, and/or geometrical considerations, several authors have derived expressions for the velocity of a particle after hitting a wall, i.e., expressions for the rebound sub-model (Matsumoto and Saito, 1970a; Tsujimoto and Nakagawa, 1983; Tsuji et al., 1985; Niño and García, 1992; Lukerchenko et al., 2006; Lukerchenko et al., 2009a). Two of these sub-models, proposed by Tsuji et al. (1985), and García and Niño (1992), have been widely used for particles moving not only close to stream beds but also close to walls in different industrial applications (Tsuji et al., 1987, Sommerfeld, 1992; Niño and García, 1998a, b; Sommerfeld and Huber, 1999; Lee et al., 2000; Kartushinsky and Michaelides, 2004; Lee et al., 2006). In turn, the randomness of the collision phenomenon is influenced by the effect of the shape of the bouncing particle and by the intrinsic roughness of the wall. Combined, these two factors create the irregular saltating trajectory that is observed in experiments. In spite of the general agreement on the basic physics behind the collisions, there is still considerable debate (and uncertainty) regarding how to reproduce mathematically the randomness within the particle saltating process, i.e., on the bed-representation sub-model (García and Niño, 1992), thereby providing a realistic approximation of the experimental observations.

To the best of my knowledge, in spite of the fact that a small number of 3D models of particle bed-load motion have been published in recent years, no systematic study has either addressed the accuracy of proposed algorithms of collision with the wall. Further, no paper has addressed the accuracy emanating from the combination of several sub-models and coefficients. Without such knowledge, the predictive capacity of these models is indeed uncertain. Numerous questions arise regarding the rigor of the models:

a) Which formulation for the bed-representation sub-model provides the closest prediction to the experimental data?

b) Can formulations proposed for air-water flows approximate the particle collisions with streambeds?

c) Which values for the friction and restitution coefficients produce better results?

d) How well do models represent the transverse particle motion in a 3D model?

This chapter, therefore, presents an assessment of the accuracy of different collision sub-models and proposes a new collision algorithm based on physical considerations. The performance of each sub-model is compared with experimental data collected by several authors during the last 20 years. The chapter is organized as follows. In Section 3.2, a 3D model to describe the free-flight of a spherical particle in a boundary-layer flow is presented. Then the particle collision sub-models analyzed in this work are introduced, together with the roughness (bed-representation) sub-models. Also in Section 3.2 a 3D roughness sub-model is presented. In Section 3.3 a description of the simulations undertaken and the data used to validate the model is carried out. Finally, results are discussed in Section 3.4, where an assessment of the importance of forces in the particle motion and the capability of the model to reproduce particle diffusion (scattering) are presented.

## 3.2. 3D MODEL

### 3.2.1. Sub-model for particle free flight

A 3D sub-model is proposed herein to describe the particle trajectory and velocity between collisions. This model formally extends the 2D equations for the rate of change of the components of the particle velocity proposed by Niño and García (1994), and combines them with a new treatment (as opposed to Niño and García, 1994) for the rotation of the particle through the equation of angular momentum. It also adopts certain hypotheses to make the problem more tractable.

The sub-model equations provide the dimensionless stream-wise, wall-normal, and span-wise particle velocities ($u_p$, $w_p$, and $v_p$, respectively; Fig. 3-1), considering the particle diameter, $d_p$, as a length scale and the wall-friction (shear) velocity, $u_*$, as a velocity scale:

$$\frac{du_p}{dt} = \alpha \frac{\sin\theta}{\tau_*} - \frac{3}{4}\alpha\, C_D \left(u_p - u_f\right)\left|\vec{u}_r\right| + \alpha\, C_m w_p \frac{du_f}{dz} + \frac{9\alpha}{\sqrt{\pi R_p}\,\tau_*^{1/4}} \int_0^t \frac{d}{d\tau}\left(u_f - u_p\right)\frac{d\tau}{\sqrt{t-\tau}} \tag{3-1}$$

$$\frac{dw_p}{dt} = -\alpha \frac{\cos\theta}{\tau_*} - \frac{3}{4}\alpha\, C_D\, w_p \left|\vec{u}_r\right| + \frac{3}{4}\alpha\, C_L \left(\left|\vec{u}_r\right|_T^2 - \left|\vec{u}_r\right|_B^2\right) - \frac{9\alpha}{\sqrt{\pi R_p}\,\tau_*^{1/4}} \int_0^t \frac{d}{d\tau} w_p \frac{d\tau}{\sqrt{t-\tau}}$$
$$+ \frac{3}{4}\alpha \left|\vec{u}_r\right| \left(\varpi_y - \frac{1}{2}\frac{du_f}{dz}\right) \tag{3-2}$$

$$\frac{dv_p}{dt} = -\frac{3}{4}\alpha\, C_D\, v_p \left|\vec{u}_r\right| - \frac{9\alpha}{\sqrt{\pi R_p}\,\tau_*^{1/4}} \int_0^t \frac{d}{d\tau} v_p \frac{d\tau}{\sqrt{t-\tau}} \tag{3-3}$$

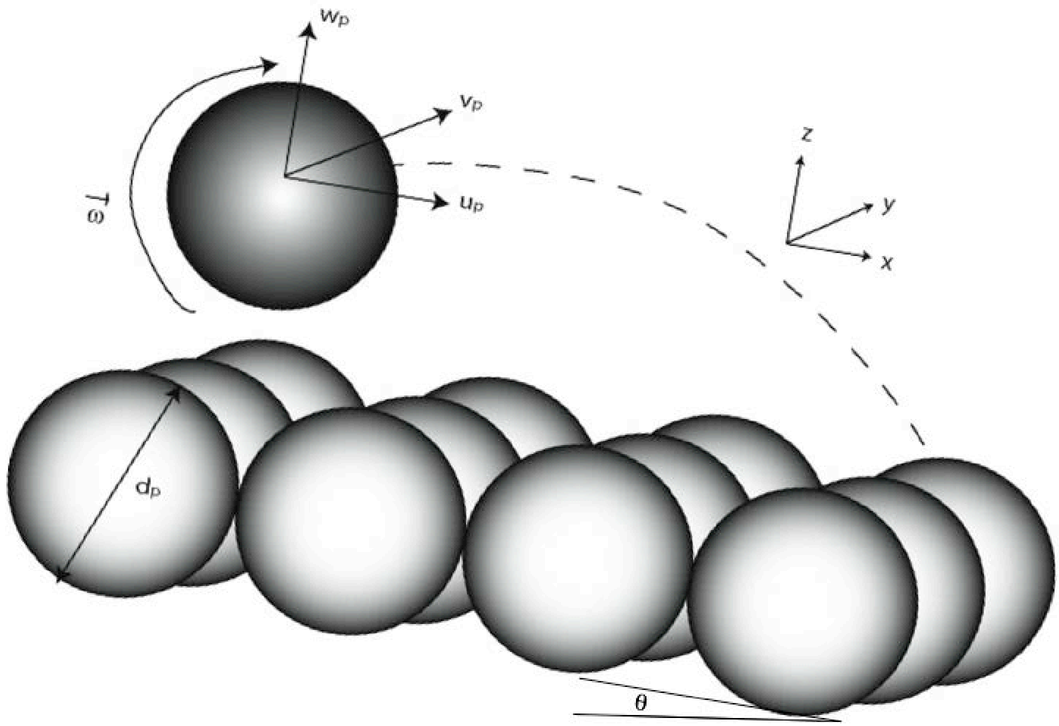


**Figure 3-1: 3D definition sketch for a saltating particle**

In these equations, $C_D$ and $C_L$ denote the drag and lift coefficients, respectively; $\vec{u}_r$, $\vec{u}_{rT}$ and $\vec{u}_{rB}$ are the relative velocity vectors (with respect to the fluid velocity) at the center, top and bottom of the particle, respectively; $u_f$ is the component in the stream-wise direction of the fluid velocity; $\alpha$ is defined as $(1 + R + C_m)^{-1}$, where $C_m$ is the virtual mass coefficient, and $R$ is defined as $\left(\frac{\rho_s}{\rho} - 1\right)$; $\tau_*$ is computed herein as ${u_*}^2/\left(g\ R\ d_p\right)$; $R_p$, the explicit particle Reynolds number, is $\left(R\ g\ {d_p}^3\right)^{0.5}/\nu$ where $\nu$ is the kinematic water viscosity; $\theta$ is the angle of the channel bed with respect to a horizontal plane; $\varpi_y = \underline{\omega}_y d_p/u_*$ denotes the dimensionless component of the particle rotation vector in the transverse direction, where $\underline{\omega}_y$ represents the dimensional particle angular rotation along the span-wise axis; $t$ denotes the time coordinate; $\tau$ is a dummy variable for integration; and $z$ denotes the wall-normal direction. The terms on the right hand side of Eq. (3-1) correspond to the following forces per unit mass: submerged gravitational force, non-linear drag, the remainder of the added-mass force, and the Basset force, respectively. On Eq. (3-2), the terms are: submerged gravitational force, non-linear drag, lift, Basset and Magnus forces, respectively. On Eq. (3-3), the terms represent the drag and Basset forces, respectively. The operator $d(\cdot)/dt$ indicates the material derivative using the particle velocity.

The non-dimensional particle rotation vector, $\vec{\varpi}$ , is in turn given by the following vector equation proposed originally by Yamamoto et al. (2001):

$$\boldsymbol{\frac{d\vec{\varpi}}{dt} = -C_t \frac{15}{16\pi} |\vec{\varpi}_r| \vec{\varpi}_r} \tag{3-4}$$

where $C_t = C_1/\sqrt{R_{eR}} + C_2/R_{eR} + C_3 R_{eR}$ is a non-dimensional coefficient which is a power-law function of the Reynolds number of the rotational motion (Yamamoto et al., 2001); $R_{eR} = d_p^2|\varpi_r|/4\nu$ denotes the Reynolds number for the rotational motion; the coefficients $C_1$ , $C_2$ , and $C_3$ are obtained from the table presented in Yamamoto et al. (2001), and $\vec{\varpi}_r$ is the non-dimensional relative particle rotation vector with respect to the fluid vorticity. Only a few authors have included similar angular velocity to their free-flight models (Lukerchenko et al., 2006; Harada and Gotoh, 2006; Lukerchenko et al., 2009a; Moreno and Bombardelli, 2012).

In order to obtain Equations (3-1) to (3-3) the local mean velocity of the fluid $u_f$ must be specified. The semi-logarithmic law for the mean velocity profile for a turbulent flow was considered, for smooth, rough and transition flow behaviors (Davidson, 2005). The flow field was assumed to be uniform in the transverse and vertical directions. In that the following was considered to simplify the equations: a) since the velocity of the fluid varies only in the stream-wise direction as a function of height ($v_f$ and $w_f$ are uniform), the stream-wise and span-wise components of the lift force are equal to zero; b) for the same reason (only $u_f$ is not uniform) the span-wise and wall-normal components of the virtual mass force are also zero; and c) the stream-wise and wall-normal components of the Magnus force are discarded on grounds that in average the particle relative rotation vector has negligible components other than $\varpi_y$, a fact which was corroborated through many computations (see González, 2008).

Eqs. (3-1) to (3-4) were integrated numerically using the standard fourth-order Runge-Kutta method (Isaacson and Keller, 1966), to obtain the particle linear and angular velocity at every time step. The drag coefficient was computed employing the regression proposed by Yen (1992) as a function of $Re_p$, the particle Reynolds number (the product of the relative velocity between particle and water and the particle diameter, divided by the kinematic viscosity of water). González (2008) compared predictors for the drag coefficient given by Rubey (1933), Shiller and Naumann (1933), Engelund and Hansen (1967), Turton and Levespiel (1986), and Yen (1992). For values of the particle Reynolds number larger than 10, while the last two predictors provide close results to those given by the formulation of Schiller and Naumann (1933), the maximum difference can be as high as 30% between Yen's and Rubey's expressions. The lift coefficient in turn varies within relatively narrow ranges (between 0 and 0.5). In this case, it was considered constant and equal to 0.2, as proposed by Wiberg and Smith (1985). The lift force term is adopted from the work of Wiberg and Smith (1985), and also used in Niño and García (1994). Special care is needed to integrate the Basset force, because the integral is singular at the upper integration limit. The methodology proposed by Bombardelli et al. (2008) (see also González et al., 2006, 2007; and González, 2008) was used to circumvent this problem.

### 3.2.2. Sub-models for particle collision with the bed

As said, a collision model comprises two sub-models: a) a series of equations describing the particle velocity after the rebound and b) a sub-model for the bed roughness (bed representation). Two widely used sub-models for particle rebound have been adopted, as discussed below. One of these models has not been employed much in river mechanics.

***2D model by García and Niño (1992) for particle rebound with the wall***

García and Niño (1992) developed a 2D rebound model based on the ideas of Tsujimoto and Nakagawa (1983), considering a saltating particle that approaches the bed at an angle $\theta_{in}$ and strikes the surface of the bed that faces upstream with an angle $\theta_b$ (see Fig. 3-2 and Appendix 3-A). The model has been used by Niño and García (1994), Niño and García (1998a,b), Lee et al. (2000), Lee et al. (2006), and Lukerchenko et al. (2009a,b), with good agreement with experimental data for natural sediments saltating in a turbulent channel. This model has been extended to 3D by Lee et al. (2006). A limitation of this model is that it does not describe the change on the particle rotation after the collision with the bed. Equations for this model are presented in Appendix 3-A. It is possible to see that the tangential and wall-normal velocity components of the particle before and after the rebound are linked by a friction coefficient and a restitution coefficient, respectively.

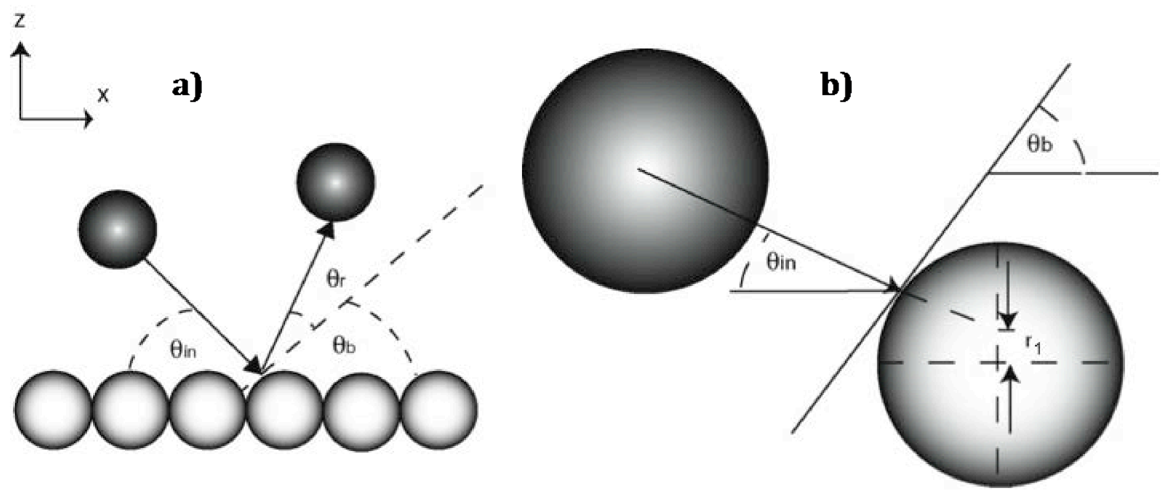


**Figure 3-2: 2D collision of a particle with the bed. The bed is composed by uniformly packed spheres placed one next to each other. The particle diameter $d_p$ is equal for the moving and the resting spheres. a) Side view. b) Detail. Definition of $\theta_{in}$ and $\theta_b$; $\theta_b$ denotes the angle of the plane tangent to the point of impact and the plane of spheres.**

### *3D model by Tsuji et al. (1985) for particle rebound with the wall*

A different 2D rebound model, derived originally by Matsumoto and Saito (1970b) and later extended to 3D by Tsuji et al. (1985), considers the conservation of linear and angular momentum before and after the rebound. The post-collision velocities (see Fig. 3-3), expressed as a function of the particle velocity immediately before the collision, are calculated depending on whether the particle slides on the bed or not. These equations (see Appendix 3-B) are developed for a horizontal contact plane between the flying particle and the bed, and are derived in Crowe et al. (2011). The appeal of this model is that it can be easily extended to simulate the inter-particle collisions, a feature that was also added to the present 3D model for multiple moving particles (see González, 2008 and Moreno and Bombardelli, 2012). Tsuji et al.'s model has been extensively used in pneumatic conveying systems (Tsuji et al., 1987; Sommerfeld, 1992; Sommerfeld and Huber, 1999; Kartushinsky and Michaelides, 2004) but only a few times, to the best of our knowledge, to address the motion of natural sediment particles in a turbulent channel (Lukerchenko et al., 2006; 2009a; Bialik et al., 2012; Moreno and Bombardelli, 2012).

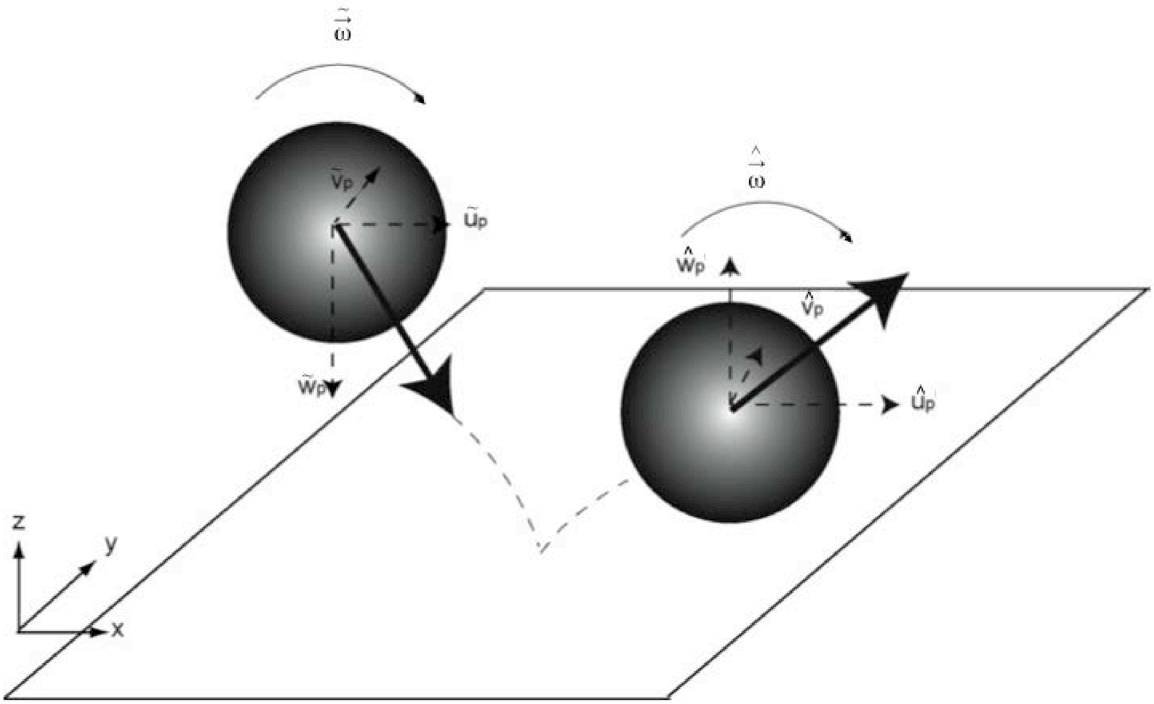


**Figure 3-3: Parameter definition for a 3D particle-wall collision. Tsuji et al. (1985) model. Particle velocities after collision are denoted with the superscript ^, while velocities before collision are denoted with the superscript ~.**

***Models for the treatment of the surface: roughness (bed-representation) sub-models***

To avoid the attenuation of the vertical velocity which otherwise would occur after tens of rebounds, the irregularity of the collision process must be considered (Gordon et al., 1972; Crowe et al., 2011). Several authors have incorporated the effect of the bed roughness into the collision model through the angle between the channel surface and the tangent to the sphere on the bed at the point of contact between the flying particle and the bed, $\theta_b$, mentioned above (Fig. 3-2). In other models the wall has been replaced by a virtual wall where its inclination, $\theta$, has been assumed to be either *uniformly* distributed in the range (-4º, +4º) (Tsuji et al., 1987), or *normally* distributed between -4º and 4º (Sommerfeld, 1992).

García and Niño (1992) formulated a conditional probability density function $p(\theta_b|\theta_{in})$ of an angle $\theta_b$ for a given value of $\theta_{in}$ of collision (see Fig. 3-2). García and Niño (1992) considered that the angle $\theta_{in}$ can vary from a maximum of 30º at the upstream side of the particle to a minimum of -30º at the downstream side of the particle. The set of angles within the range is mapped into a set of values $r_1$ along a vertical line passing through the center of the particle (Fig. 3-2). García and Niño assumed $r_1/d_p$ to be uniformly distributed between 0 and 0.5 and obtained it via a random number generator. During the collision, a geometrical relationship between $\theta_b$, $\theta_{in}$, $d_p$ and $r_1$ can be established:

$$\frac{r_1}{d_p} = \frac{1}{2}[\cos(\theta_b) - \tan(\theta_{in})\sin(\theta_b)] \tag{3-5}$$

### 3.2.3. Bed-representation sub-model

This chapter introduces 3D algorithms to represent the wall roughness, extending the García and Niño (1992) treatment of the bed. The point of contact between the flying particle and the bed now defines an inclination plane, which is specified by using two angles, $\theta_b$ (Fig. 3-2) and $\alpha_b$ (Fig. 3-4).

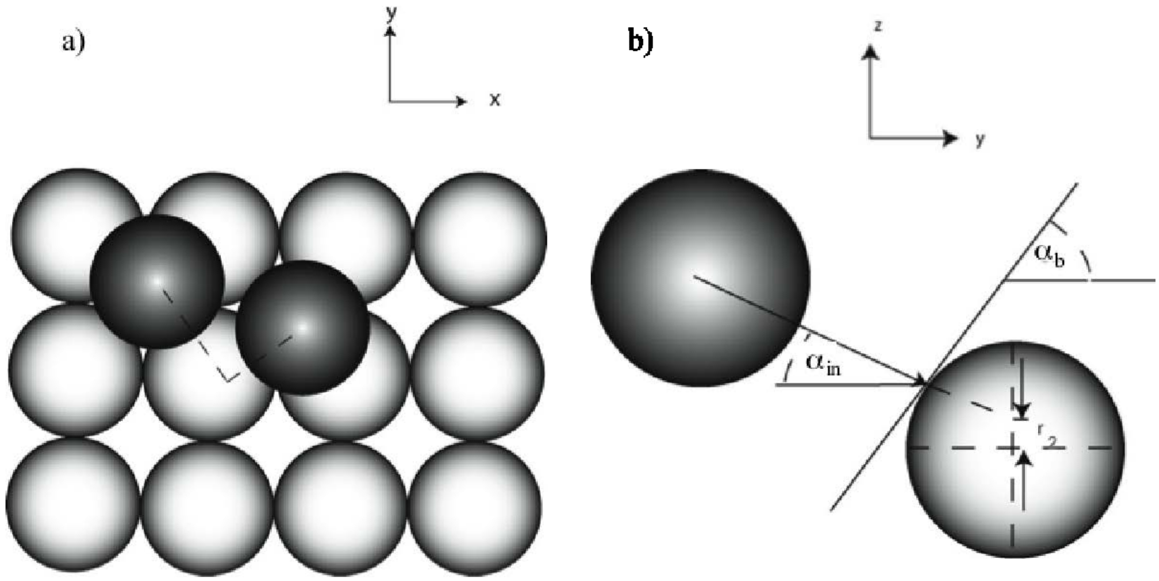


**Figure 3-4: 3D collision of a particle with the bed. The bed is composed by uniformly packed spheres placed one next to each other. The particle diameter $d_p$ is equal for the moving and the resting spheres. a) Top view. b) Side view. Definition of $\alpha_{in}$ and $\alpha_b$.**

For practical purposes the previous bed-representation sub-models will be named as follows: García and Niño (1992) 2D sub-model will be called sub-model R1, Tsuji et al. (1987) sub-model will be called sub-model R2, and Sommerfeld (1992) sub-model will be called sub-model R3. Given the fact that there are no exact and undisputed approximations, five new sub-models are defined. Sub-model R4 assumes that both angles $\theta_b$ and $\alpha_b$ are uniformly distributed between 0º and 30 º, and -30º and 30 º, respectively. The latter angles are determined through random number generators. Sub-model R5 is based on relations similar to Eq. (3-5) which connect $\theta_b$ with $r_1$ and $\theta_{in}$, and $\alpha_b$ with $r_2$ and $\alpha_{in}$ (see Fig. 3-2 and Fig. 3-4), sub-model R6 uses a modification of sub-model R5, while sub-models R7 and R8 use a combination of previous sub-models.

In sub-model R5 the values of $r_1/d_p$ and $r_2/d_p$ are obtained through a random number. These random numbers are uniformly distributed following the procedure presented by García and Niño (1992), which has “some” dependence with the incidence angles $\theta_{in}$ and $\alpha_{in}$, when using Eq. (3-5). In sub-model R6 the values of $r_1/d_p$ and $r_2/d_p$ are obtained by reducing this range depending on the particle conditions right before the collision, defined as $r_{min1}/d_p$ and $r_{max1}/d_p$, and $r_{min2}/d_p$ and $r_{max2}/d_p$, respectively. Both variables ($r_1/d_p$ and $r_2/d_p$) are assumed to be uniformly distributed. These ranges are defined as follows: the minimum values ($r_{min1}/d_p$ and $r_{min2}/d_p$) are equal to 0, and the maximum values ($r_{max1}/d_p$ and $r_{max2}/d_p$) are obtained by replacing the incidence angle ($\theta_{in}$ and $\alpha_{in}$, respectively) in Eq. (3-5) and assuming that the bed contact angles ($\theta_b$ and $\alpha_b$, respectively) are equal to 30º. Then, the values of $r_1/d_p$ and $r_2/d_p$ are obtained (again using Eq. (3-5)) through random number generators between $r_{min1}/d_p$ and $r_{max1}/d_p$, and $r_{min2}/d_p$ and $r_{max2}/d_p$. The latter sub-model thus offers a “stronger” dependence on the incidence angles $\theta_{in}$ and $\alpha_{in}$. Sub-model R7 follows the approach of sub-model R5 for calculating $\theta_b$ and the approach of sub-model R4 for calculating $\alpha_b$. Sub-model R8, instead, follows the approach of sub-model R6 for calculating $\theta_b$ and the approach of sub-model R4 for calculating $\alpha_b$. Table 3-1 summarizes all roughness sub-models described above for the 3D bed representation, which are the sub-models introduced in this work (sub-models R4 to R8).

**Table 3-1: Bed-representation sub-models developed in this study**

| Sub-model for bed-representation | Variables | Range |
|---|---|---|
| R4 | $\theta_b$,<br>$\alpha_b$ | 0° / 30°,<br>-30° / 30° |
| R5 | $r_1/d_p$,<br>$r_2/d_p$ | 0 / 0.5,<br>0 / ±0.5 |
| R6 | $r_1/d_p$,<br>$r_2/d_p$ | $0\ /\ r_{max1}/d_p$,<br>$0\ /\ \pm r_{max2}/d_p$ |
| R7 | $r_1/d_p$,<br>$\alpha_b$ | 0 / 0.5<br>-30° / 30° |
| R8 | $r_1/d_p$,<br>$\alpha_b$ | $0\ /\ r_{max1}/d_p$,<br>-30° / 30° |

## 3.3. DESCRIPTION OF THE EXPERIMENTAL DATA AND SIMULATIONS

### 3.3.1. Analysis of the experimental data available

The most recent experiments containing detailed information on the trajectories of particles saltating in water are those published in Lee (1993), Niño et al. (1994), Lee and Hsu (1994), Niño and García (1998a,b) and Lee et al. (2006). The main characteristics of these experiments are presented in Table 3-2, where $H$ and $L$ represent the dimensionless jump height and length respectively.

The values of the friction ($f$) and restitution ($e$) coefficients highly depend on the material of the saltating particle and on flow conditions; therefore, it is not possible to provide universal values. Table 3-3 summarizes values recommended by different authors, indicating the wide range of values that those numbers may hold.

**Table 3-2: Characteristics of the experimental data of saltating particles**

| Authors | Recording device | Particle size (mm) | Number of jumps considered | $u_*$ (m/s) | Variables obtained |
|---|---|---|---|---|---|
| Niño et al. (1994) | Standard video camera | 15-31 | 80 | 0.14-0.23 | Average and standard deviation of $H$, $L$ and $\overline{u}_p$ |
| Niño and García (1998a,b) | High speed video camera | 0.5-0.8 | 1-2 jumps for 100 particles | 0.021-0.026 | Average and standard deviation of $H$, $L$ and $\overline{u}_p$ |
| Lee et al. (2000) | Standard video camera | 6 | No information available | 0.038-0.054 | Average of $H$, $L$ and $\overline{u}_p$ |
| Lee and Hsu (1994) | Standard video camera | 1.36-2.47 | No information available | 0.036-0.105 | Average of $H$, $L$ and $\overline{u}_p$ |
| Lee et al. (2006) | Standard video camera | 0.6 | No information available | 0.039-0.068 | Average of $H$, $L$ and $\overline{u}_p$ |

**Table 3-3: Sets of values of friction and restitution coefficients**

| Set | Author | Restitution coefficient $e$ | Friction coefficient $f$ |
|---|---|---|---|
| 1 | Niño and García (1994) | $e = 0.75 - 0.25\tau_*/\tau_{*c}$ | 0.89 |
| 2 | Schmeeckle et al. (2001) | 0.65 | 0.1 |
| 3 | Tsuji et al. (1987) | 0.8 | 0.4 |
| 4 | Shen et al. (1989) | 0.95 | 0.3 |

### 3.3.2. Characteristics of the numerical tests

Eight different cases were investigated, as discussed in Table 3-4. Each of these cases was tested with the four sets of values for the friction and restitution coefficients (see Table 3-3). Set 1 represents the values provided by Niño and García's (1994); Set 2 includes the values proposed by Schmeeckle et al. (2001); Set 3 considers the Tsuji et al. (1987) values, and Set 4 includes the values proposed by Shen et al. (1989). In Run A, both the García and Niño (1992) rebound and bed roughness sub-models are employed. The particle free-flight was calculated using the original 2D sub-model provided by the same authors (Niño and García, 1994). In Run B, Tsuji et al. (1985) rebound sub-model was employed, and this sub-model was kept in the remaining runs. The particle free-flight was calculated using the extended 3D sub-model presented in Section 3.2.1 and this sub-model was used in the remaining runs as well. The roughness pattern was defined following Tsuji et al. (1985, 1987), where the angle of the virtual wall, $\theta$, was assumed to be uniformly distributed between -4º and 4º. For Run C, the roughness pattern was defined following Sommerfeld (1992), where the angle $\theta$ was normally distributed between -4º and 4º. For Run D, the roughness pattern was considered with an angle $\theta_b$ uniformly distributed between 0º and 30º (sub-model R4). In Run E, the roughness pattern was defined using sub-model R5. In Run F, the roughness pattern was defined as in sub-model R6, while Run G and H were defined by the roughness sub-models R7 and R8, respectively (see Table 3-4). The particle angular velocity is determined using Eq. (3-4) in Runs D to H.

The numerical models were run for a simulation time long enough to have meaningful statistics of the main representative variables. In order to remove the effect of the initial conditions, the first twenty jumps were not considered in the statistical analysis.

**Table 3-4: Simulation summary**

| Model/Run | Flight sub-model | Rebound sub-model | Roughness sub-model |
|---|---|---|---|
| A | 2D Niño and García (1994) | 2D García and Niño (1992) | R1: García and Niño (1992) |
| B | 3D (Section 3.2.1) | 3D Tsuji et al. (1985) | R2: Tsuji et al. (1987) |
| C | 3D (Section 3.2.1) | 3D Tsuji et al. (1985) | R3: Sommerfeld (1992) |
| D | 3D (Section 3.2.1) | 3D Tsuji et al. (1985) | R4: Section 3.2.3 |
| E | 3D (Section 3.2.1) | 3D Tsuji et al. (1985) | R5: Section 3.2.3 |
| F | 3D (Section 3.2.1) | 3D Tsuji et al. (1985) | R6: Section 3.2.3 |
| G | 3D (Section 3.2.1) | 3D Tsuji et al. (1985) | R7: Section 3.2.3 |
| H | 3D (Section 3.2.1) | 3D Tsuji et al. (1985) | R8: Section 3.2.3 |

## 3.4. RESULTS AND DISCUSSION

### 3.4.1. Verification and validation of the particle flight sub-model. Convergence tests

The solution of the system of Eqs. (3-1) to (3-4) and the collision and bed-representation sub-models were implemented in a Fortran code. The code was firstly verified through comparisons of numerical results with solutions obtained by other packages of software for the diverse sub-models (see González, 2008). Then it was validated through comparisons with experimental results presented in Niño et al. (1994) for gravels, and in Niño and García (1998a) for sands, regarding the free flight of a single particle in a channel. This comparison was also used to assess the convergence of the numerical solution to the time step employed. It was found that the results did not vary with a non-dimensional time step equal or smaller than 0.001. The results of the comparison are presented in Figs. 3-5 and 3-6, obtained with the mesh for the converged solution, confirming that the particle trajectories predicted by the model are very close to the observed ones, within the range of experimental errors. Figs. 3-5 and 3-6 also show the relative importance of the different forces in the definition of the trajectory. Clearly, the Basset and Magnus forces do not exert apparent influence in the prediction for gravels, while they do modify significantly the predictions for sands. This result is in agreement with the findings of Niño and García (1994, 1998a,b) (also reported in González et al., 2006, and Bombardelli et al., 2008). It seems that for a larger size particle the effect exerted by the Basset force is counteracted by its own inertia.

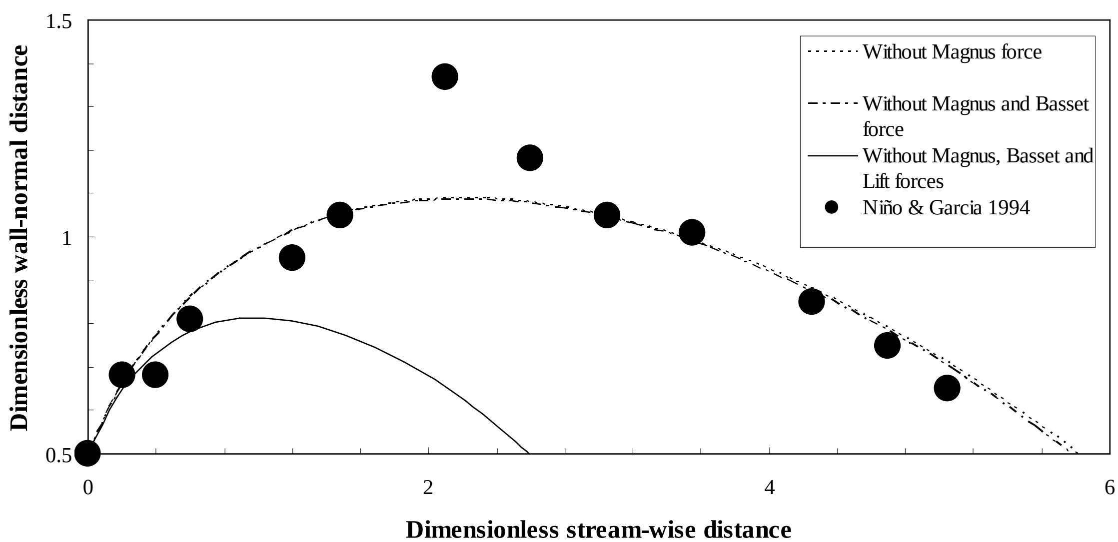


**Figure 3-5: Comparison of predictions of the particle free-flight sub-model (in 2D) with data obtained by Niño et al. (1994) for gravels. Distances are made non-dimensional by using the particle diameter. Single jump case. $d_p$ =30 mm; $u_*$=0.22 m/s.**

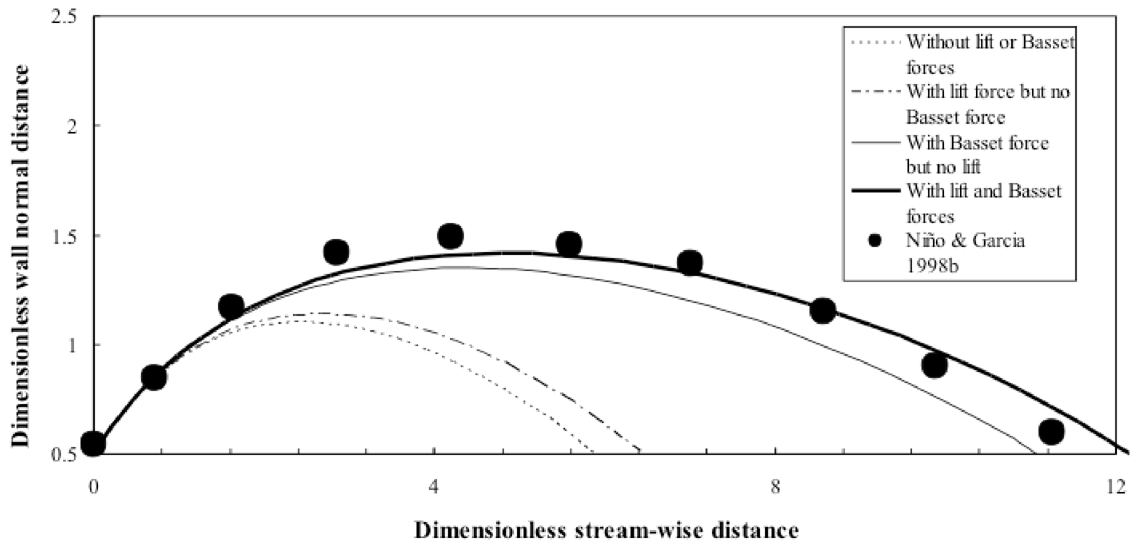


**Figure 3-6: Comparison of predictions of the particle free-flight sub-model (in 2D) with data obtained by Niño and García (1998b) for sands. Distances are made non-dimensional by using the particle diameter. Single jump case. $d_p$=0.56 mm; $u_*$ =0.025 m/s.**

### 3.4.2. Results of various flight, rebound, and roughness sub-models

**Results in terms of jump length, jump height and particle velocity**

Results of simulations explained in Table 3-4 were compared to two experimental datasets: the observations by Niño and García (1998b) ($R_p$=73), and the experiments by Lee and Hsu (1994), with $R_p$=250. As mentioned in Section 3.3.2, Runs A to H in Table 3-4 were carried out for each of the four sets of values of restitution and friction coefficients presented in Table 3-3. For $R_p$=73, five different flow intensities were simulated ($\tau_*/\tau_{*c}$= 1.79, 1.87, 2.43, 2.50 and 2.67), following the experiments by Niño and García (1998a). For $R_p$=250, instead, three flow intensities were simulated ($\tau_*/\tau_{*c}$=2.31, 3.08, and 3.85). In total, including both particle sizes, information of over 250 simulations was analyzed. Figure 3-7 presents the results for Run G, Set 2, the model that best represented both $R_p$= 73 and $R_p$= 250.

In an attempt to provide accessible means for interpretation of results, different metrics were devised and used for each empirical dataset. Since the numerical predictions are of stochastic nature, a metric involving a measure of the agreement in terms of both the mean values and the scatter (the standard deviation) is needed. For the data set of Niño and García (1998a), Table 3-5 presents the results of simulations through an overlap area index defined herein after following three steps: a) an area for each of the three parameters mentioned above ($H, L, \overline{u}_p$) is delimited by using the average value of each parameter plus/less one standard deviation. These areas are defined for both the measured data and the results obtained numerically. b) The overlap area is determined by calculating the percentage of the area of overlap of the numerical results with respect to the area of the experimental results. c) Then, the overlap areas percentages pertaining to the three parameters are averaged to obtain the overlap area index. Therefore, the larger the overlap area index is, the better the performance of the model in general (see Fig. 3-8 as an example). Although this metric may have limitations, such as the case of a small "numerical" area far from the mean values of the experiments; or the case of similar mean values between two areas with different standard deviations; etc., the authors believe it provides a reasonable metric for data comparison, as shown below. Those models with the best agreement show an area ratio (simulation results area/experimental results area) close to one, which suggest the results in those cases are reliable.

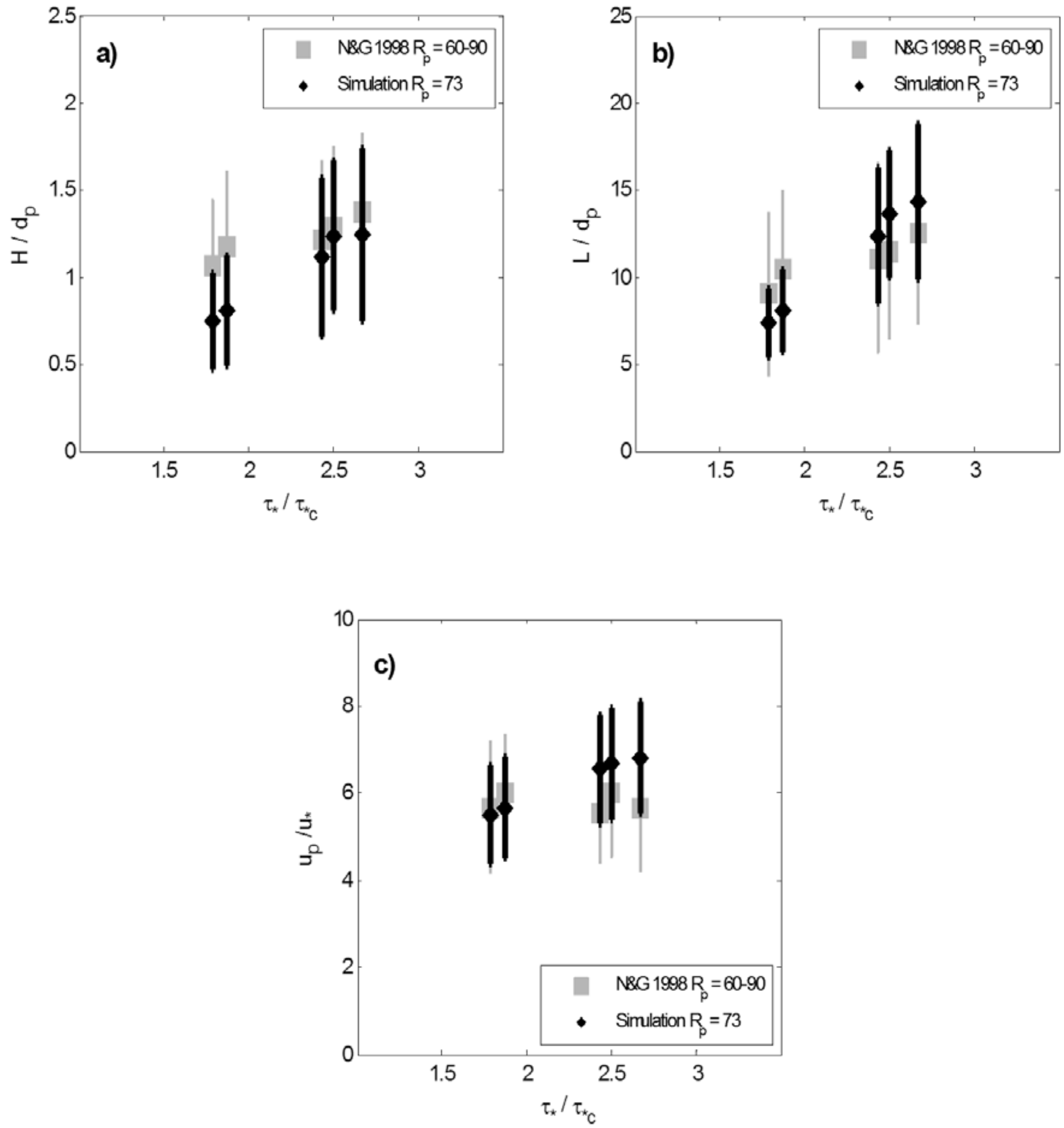


**Figure 3-7: Comparison of numerical simulations with experimental data for the case of a particle moving in a flume and rebounding with the wall (Run G, Set 2). The figure shows results associated with: the dimensionless a) particle jump height (*H*), b) particle jump length (*L*) and c) particle stream-wise mean velocity. Symbols represent mean values and vertical lines indicate two corresponding standard deviations. $R_p$ =73.**

**Table 3-5: Statistical analysis using the overlap area indices. Run for $R_p$=73**

| Run | | Set (from Table 3-3) 1 | 2 | 3 | 4 |
|---|---|---|---|---|---|
| A | Overlap Area H (%) | 39.80 | 13.37 | 29.54 | 37.18 |
| | Overlap Area L (%) | 49.74 | 7.82 | 42.76 | 44.13 |
| | Overlap Area U (%) | 72.40 | 22.37 | 73.85 | 78.63 |
| | **Overlap Index** | **53.98** | **14.52** | **48.72** | **53.31** |
| B | Overlap Area H (%) | 0.00 | 0.00 | 0.00 | 0.00 |
| | Overlap Area L (%) | 0.00 | 0.00 | 0.00 | 0.00 |
| | Overlap Area U (%) | 0.00 | 12.86 | 4.57 | 0.00 |
| | **Overlap Index** | **0.00** | **4.29** | **1.52** | **0.00** |
| C | Overlap Area H (%) | 0.00 | 0.00 | 0.00 | 0.00 |
| | Overlap Area L (%) | 0.00 | 0.00 | 0.00 | 0.00 |
| | Overlap Area U (%) | 0.00 | 0.00 | 0.00 | 0.00 |
| | **Overlap Index** | **0.00** | **0.00** | **0.00** | **0.00** |
| D | Overlap Area H (%) | 0.00 | 19.67 | 95.63 | 93.31 |
| | Overlap Area L (%) | 8.85 | 51.51 | 76.47 | 61.34 |
| | Overlap Area U (%) | 46.96 | 62.72 | 57.71 | 40.17 |
| | **Overlap Index** | **18.60** | **44.63** | **76.61** | **64.94** |
| E | Overlap Area H (%) | 5.80 | 72.38 | 3.03 | 0.00 |
| | Overlap Area L (%) | 31.55 | 46.55 | 4.15 | 0.01 |
| | Overlap Area U (%) | 67.15 | 67.60 | 40.40 | 23.02 |
| | **Overlap Index** | **34.83** | **62.18** | **15.86** | **7.68** |
| F | Overlap Area H (%) | 0.31 | 66.55 | 28.44 | 7.79 |
| | Overlap Area L (%) | 27.40 | 54.87 | 21.36 | 9.48 |
| | Overlap Area U (%) | 61.21 | 80.95 | 65.34 | 52.48 |
| | **Overlap Index** | **29.64** | **67.46** | **38.38** | **23.25** |
| G | Overlap Area H (%) | 0.00 | 72.53 | 56.65 | 18.00 |
| | Overlap Area L (%) | 22.01 | 64.13 | 33.29 | 13.41 |
| | Overlap Area U (%) | 56.52 | 75.79 | 59.10 | 41.99 |
| | **Overlap Index** | **26.18** | **70.82** | **49.68** | **24.47** |
| H | Overlap Area H (%) | 0.00 | 63.99 | 19.47 | 3.09 |
| | Overlap Area L (%) | 18.14 | 42.78 | 16.79 | 5.85 |
| | Overlap Area U (%) | 55.57 | 79.43 | 62.61 | 48.84 |
| | **Overlap Index** | **24.57** | **62.07** | **32.96** | **19.26** |

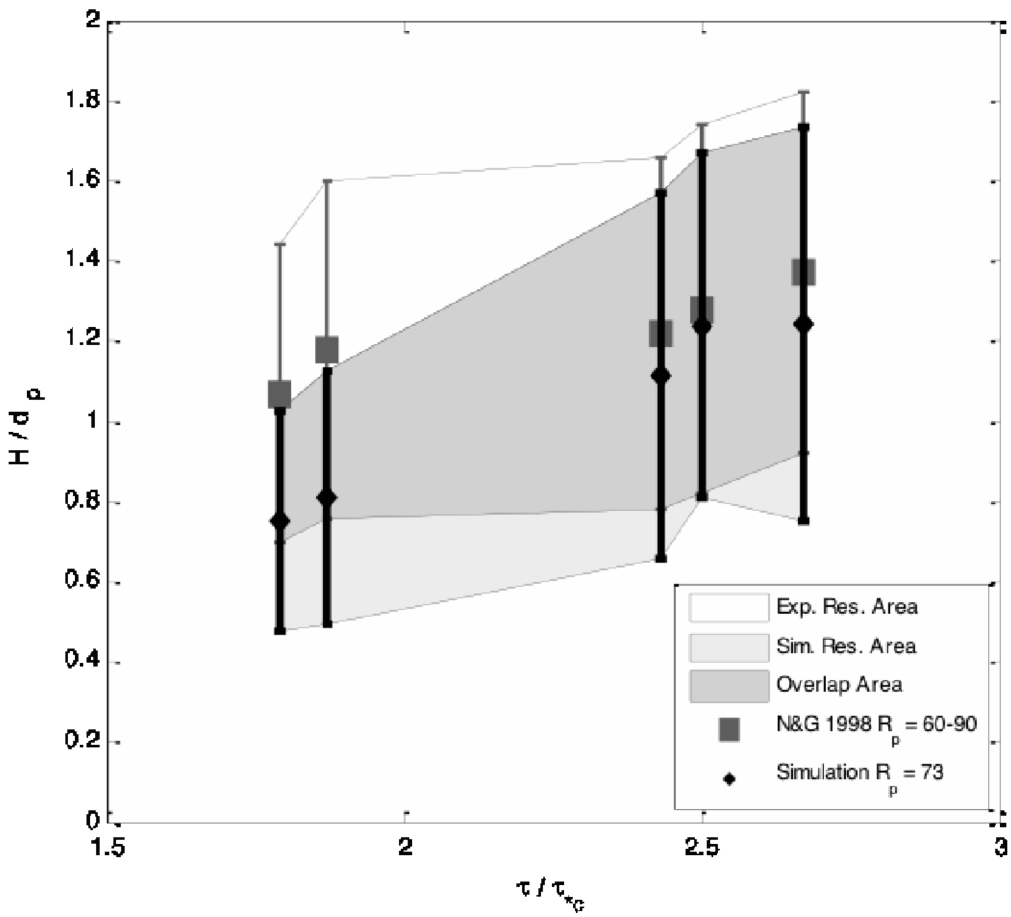


**Figure 3-8: Overlap area index determination: $R_p$=73; Run G. Set 2. The overlap area is defined as the grey area in the figure (for the non-dimensional jump height). Also shown above are the experimental results area (Exp. Res. Area), and the simulation results area (Sim. Res. Area).**

For the data of Lee and Hsu (1994), the previous method *cannot* be used because no standard deviation of the experimental data is provided. (As an example, simulation results for Run G, Set 2 (or G2) are presented in Fig. 3-9.) Table 3-6 presents the results of the root mean square error (RMSE) instead, defined as $\sqrt{\frac{\sum_{i=1}^{n}(P_i - O_i)^2}{n}}\frac{1}{\bar{O}}$ where $P_i$ and $O_i$ indicate predicted and observed data, the over-bar denotes average, and $n$ refers to the number of points. The error index for each simulation set is defined as the average between the values of RMSE observed for the particle jump height, length and mean particle velocity. Figure 3-10 shows a summary of the results presented in Tables 3-5 and 3-6. Figure 3-10a depicts a ranking of the best 15 models, those with larger overlap area index (OAI) for $R_p$=73. As it can be seen, Run D, Set 3 (D3 as shown in the figure), followed by Run G, Set 2 (G2 in the figure), are the models with closer results when compared with the experimental data, as shown in Table 3-5. Figure 3-10b depicts the ranking of the best models, those with smaller RMSE, for $R_p$=250. For this case, Run D, Set 2 (D2 in the figure) followed by Run G, Set 2 (G2 in the figure) are the models that better approximate the experimental results. Figure 3-10c shows the averaged results from both particle sizes, creating a rank of the models best suited for both cases. This ranking was created calculating the arithmetic mean of the rankings for both particle sizes, and then sorted in ascending order. For the simulations presented herein the model that performs the best for both particle sizes is Run G, Set 2 (G2), which is the case we have shown in Figs. 3-7 to 3-9.

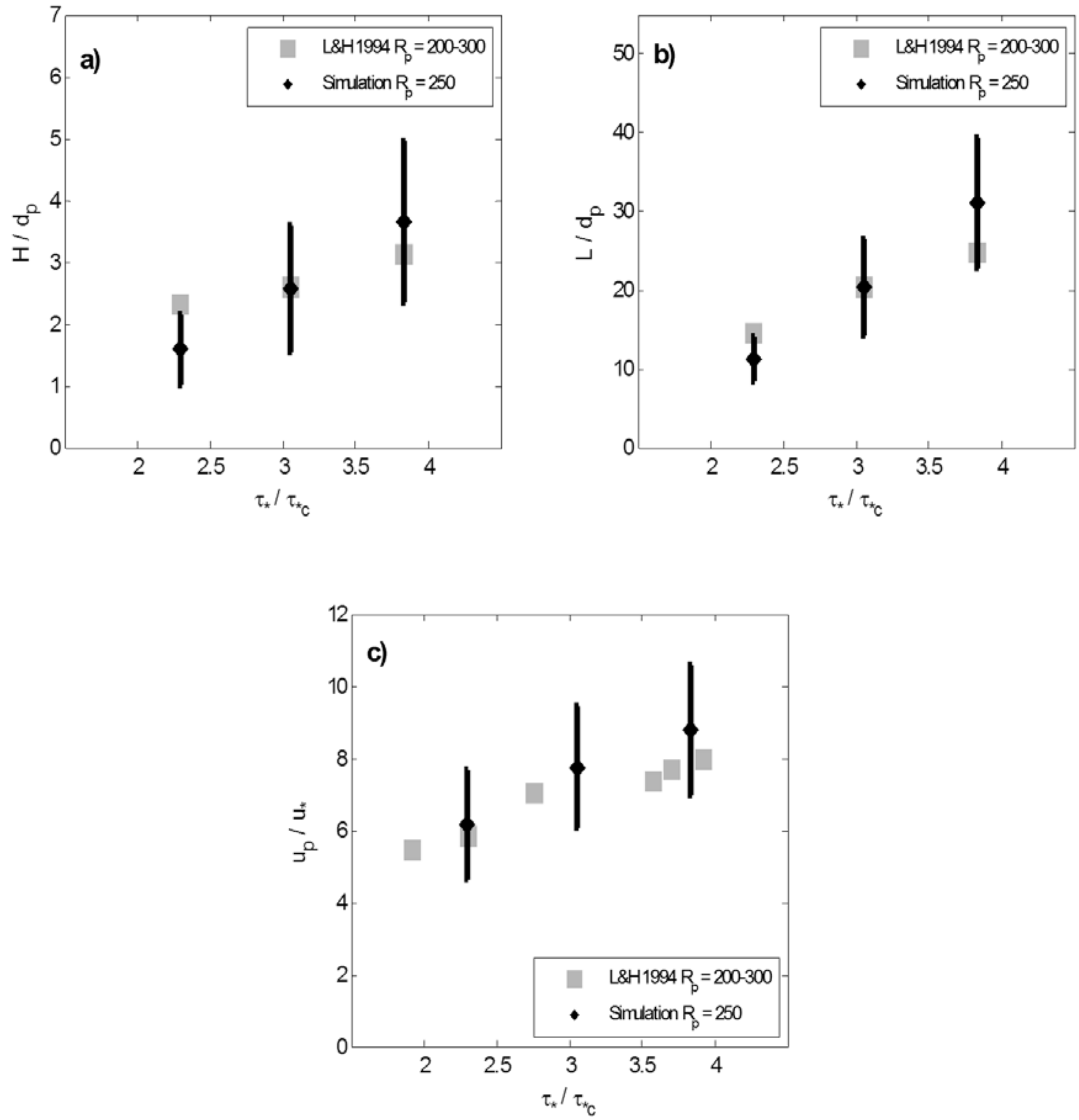


**Figure 3-9: Comparison of numerical simulations to experimental data for the case of a particle moving in a flume and rebounding with the wall (Run G, Set 2). The figure shows results associated with: the dimensionless a) particle jump height (*H*), b) particle jump length (*L*) and c) particle stream-wise mean velocity. Symbols represent mean values and vertical lines indicate two corresponding standard deviations. $R_p$=250.**

**Table 3-6: Statistical analysis using the root mean squared error (RMSE). Run for $R_p$=250**

| | | Set (from Table 3-3) | | | |
|---|---|---|---|---|---|
| Run | | 1 | 2 | 3 | 4 |
| A | RMSE H (%) | 39.80 | 13.37 | 29.54 | 37.18 |
| | RMSE L (%) | 49.74 | 7.82 | 42.76 | 44.13 |
| | RMSE U (%) | 72.40 | 22.37 | 73.85 | 78.63 |
| | **Error Index** | **53.98** | **14.52** | **48.72** | **53.31** |
| B | RMSE H (%) | 0.00 | 0.00 | 0.00 | 0.00 |
| | RMSE L (%) | 0.00 | 0.00 | 0.00 | 0.00 |
| | RMSE U (%) | 0.00 | 12.86 | 4.57 | 13.96 |
| | **Error Index** | **0.00** | **4.29** | **1.52** | 4.65 |
| C | RMSE H (%) | 0.00 | 0.00 | 0.00 | 0.00 |
| | RMSE L (%) | 0.00 | 0.00 | 0.00 | 0.00 |
| | RMSE U (%) | 0.00 | 0.00 | 0.00 | 0.00 |
| | **Error Index** | **0.00** | **0.00** | **0.00** | **0.00** |
| D | RMSE H (%) | 1.64 | 0.91 | 9.13 | 11.64 |
| | RMSE L (%) | 8.91 | 3.85 | 61.43 | 75.44 |
| | RMSE U (%) | 1.21 | 0.36 | 4.81 | 5.60 |
| | **Error Index** | **3.92** | **1.70** | **25.13** | **30.89** |
| E | RMSE H (%) | 1.25 | 0.76 | 7.61 | 9.09 |
| | RMSE L (%) | 7.05 | 6.27 | 50.08 | 57.45 |
| | RMSE U (%) | 1.08 | 1.21 | 4.08 | 4.68 |
| | **Error Index** | **3.13** | **2.75** | **20.59** | **23.74** |
| F | RMSE H (%) | 1.69 | 0.72 | 1.99 | 5.60 |
| | RMSE L (%) | 9.96 | 4.70 | 12.75 | 36.14 |
| | RMSE U (%) | 1.46 | 0.46 | 1.72 | 3.18 |
| | **Error Index** | **4.37** | **1.96** | **5.49** | **14.97** |
| G | RMSE H (%) | 1.53 | 0.52 | 5.82 | 7.98 |
| | RMSE L (%) | 8.39 | 4.09 | 39.14 | 51.47 |
| | RMSE U (%) | 1.26 | 0.73 | 3.51 | 4.28 |
| | **Error Index** | **3.73** | **1.78** | **16.16** | **21.24** |
| H | RMSE H (%) | 1.39 | 0.96 | 4.99 | 6.71 |
| | RMSE L (%) | 7.72 | 7.37 | 32.56 | 42.24 |
| | RMSE U (%) | 1.29 | 0.96 | 2.93 | 3.62 |
| | **Error Index** | **3.47** | **3.10** | **13.49** | **17.52** |

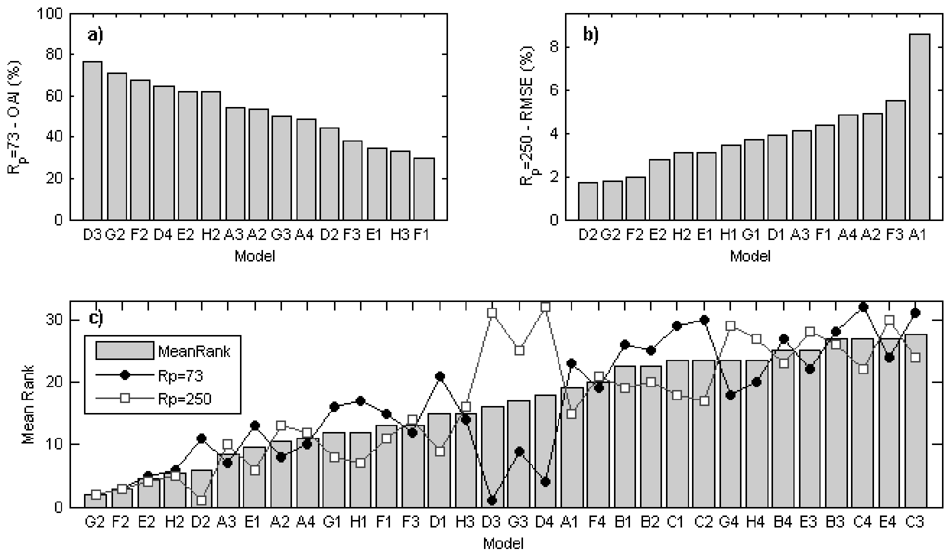


**Figure 3-10: Performance comparison of different models (Runs and Sets). Models with best results are shown in ascending order: a) Best 15 models for $R_p$=73 according to their Overlap Area Index (OAI) results, higher percentages denote better approximation to experimental results; b) best 15 models for $R_p$=250 according to their Root Mean Square Error (RMSE), lower percentages denote better approximation to experimental results; c) mean rank of models in ascending order, calculated as the arithmetic mean of the rank of both particle sizes.**

For the García and Niño (1992) particle-wall collision and roughness sub-models, the best agreement with the experimental results for Run A and $R_p$= 73 was obtained using Set 1 of friction and restitution coefficients (which incidentally are the proposed values by Niño and García (1994) for this particle size). These tests present a slightly smaller standard deviation than the experiments. For other runs, simulation results in Table 3-5 indicate that Run B does not represent at all the experimental observations. (The overlap areas for jump height and length, for all restitution and friction coefficients, are equal to zero.) The same disagreement with data is also observed for Run C (Sommerfeld (1992) roughness model). This result can be interpreted in terms of the limited range for the impact angle of the Sommerfeld's model. A closer look at the results shows that the roughness model used in Runs A to C produce either very large or extremely small jumps, generating a jump distribution, which possesses a sizeable standard deviation. Analyzing these models in more detail, the assumption that the contact plane is defined with angles varying between -30º and 30º or -4º and 4º, disregarding the incidence angle of the moving particle, seems to be unrealistic. Positive values of $\theta_b$ indicate that the particle hits the upstream face of the lying particle, and negative values of $\theta_b$ indicate a collision occurring at the downstream face of the bed particle. Considering the characteristic of the particle velocity just before the collision, there is a bigger probability of hitting the upstream face than the downstream side of the roughness (see Sommerfeld and Huber, 1999). By assuming a uniform probability for $\theta_b$ (as sub-model A does) that includes both positive and negative angles, the model considers particle collision angles equal to zero to have an important probability, generating several simulation results with jump lengths and heights almost equal to zero, which is unrealistic. The roughness sub-model proposed in this work and utilized in Run D for $R_p$=73, which basically increases the range of the impact angles with respect to the range proposed by Tsuji et al. (1987) and Sommerfeld (1992), from -4° to +4° to 0° to 30°, leads to a remarkable increase in the overlap index. The simulation results present a very good agreement with the experimental data with an overlap area index ranging from 18.6% (Set 1) to 76.6% (Set 3). Simulation results for Run D, Set 3, produce the strongest agreement with the experimental data for $R_p$=73. The results in Table 3-5 (and Figure 3-10a) suggest that Run D greatly improves the prediction made by Runs B and C, due to the reset in the range of variability of $\theta_b$ from 0° to 30°. The total overlap index is 76.61%, but when looking at the particular overlap index for H (95.63%) and L (76.47%), one can see how close this Run follows the average jump height and length from the experimental data, although the stream-wise velocity has a lower overlap index (57.71%). Following Run D3 are Runs G2 (Overlap Index 70.82%) and F2 (67.46%), in that order (Fig. 3-10a). The only difference for Runs D, G and F can be found in their different approach for the roughness sub-model (see Table 3-4). In short, the difference in the calculation of $\theta_b$ and $\alpha_b$ namely: a completely random approach for both angles (R4 in Table 3-1), some dependence on the incidence angle for $\theta_b$ (R7 in Table 3-1), and a stronger dependence of the incidence angles for $\theta_b$ and $\alpha_b$ (R6 in Table 3-1), respectively. It seems that for the particular case of $R_p$=73, a completely random treatment for the roughness sub-model will give the best results, albeit the models that use more information from the incidence angle right before collision still do a very good job. Regarding the restitution ($f$) and friction ($e$) coefficients, the best approximation (D3) is obtained when using Tsuji et al. (1987) values, while the other two Runs (G2 and F2) use the values suggested by Schmeeckle et al. (2001).

For the case of $R_p$=250 (see Table 3-6 and Fig. 3-10b) the Run with the closest results to experimental data is D2 (RMSE 1.70%), closely followed by G2 (RMSE 1.78%) and F2 (RMSE 1.96%). It is important to remember that more complete experimental information for this particle size would help to better rank the different approaches when including standard deviations. When comparing this outcome with the one obtained for $R_p$=73, the same approaches for the roughness sub-models are found to be the best suited, and in the same order: completely random (R4), some dependence on the incidence angle for $\theta_b$ (R7), and finally stronger dependence in both incidence angles (R6). For this particle size the best results are obtained when using the restitution and friction coefficients from Schmeeckle et al..

Now we analyze the overall results for each Run for both particle sizes (Fig. 3-10c). In order to do that, we have found those models that work best for both $R_p$ values, we averaged the ranks of the best Runs for both particle sizes and sorted them in ascending order. Although D3 was the best result for $R_p$=73, it gave very bad approximation to experimental values for $R_p$=250, hence overall it had a mediocre performance. For $R_p$=250 the best Run was D2, however it ranked 11th when predicting values for $R_p$=73, with four other models with better predictions in the overall ranking. From Fig. 3-10c several conclusions can be drawn. It is very clear that according to our simulations, the first five Runs that best approximate all two experimental datasets use the restitution and friction coefficients from Set 2 (Schmeeckle et al.), suggesting that for simulations within the sand range, overall, $f$=0.65 and $e$=0.1 seem to lead to closer approximations to the experimental data. The best results were obtained for Runs: G2, F2 and E2, in that order. All three Runs use the 3D approach for the particle free flight, all three use the 3D Tsuji et al. rebound sub-model, however the roughness sub-models are different. For Run G, as mentioned before, the roughness sub-model has some dependence of the incidence angle for the computation of $\theta_b$ when using Eq. (3-5), nonetheless the computation of $\alpha_b$, is achieved randomly. Run F has a strong dependence for both incidence angles, $\theta_b$ and $\alpha_b$, through the estimation of $r_{max}/d_p$. The latter model involves one extra step in complexity because of the geometrical constraint place to the calculation of $r_1/d_p$ and $r_2/d_p$ Finally Run E, has some dependence in both incidence angles through Eq. (3-5). Consequently all three models have at least some level of dependence on the incidence angles, yet, in the case of Run G this is valid only for the incidence angle $\theta_b$, which is the angle that mainly controls the particle jump height and length, while $\alpha_b$, the angle that primarily controls the particle lateral diffusion (or dispersion), can be computed simply by using a random generator. Experimental studies for particle saltation for different particle sizes, with in the sand range (gravel as well), that measure lateral particle diffusion may help to better elucidate the importance of the dependence on the incident angle $\alpha_b$.

**Particle angular velocity and takeoff angles**

A comparison of the numerically obtained values of the mean dimensionless spin rate (in each jump) with the experimental results of Niño and García (1998a) is shown in Fig. 3-11. It can be seen that the agreement is very satisfactory. Validation of the particle-rotation sub-model through comparisons with experimental data of Lee and Hsu (1994) for $R_p$=2126 (not shown herein), was also carried out, with acceptable agreement (see González, 2008). In conformity with Niño and García (1998a), simulation results show that the particle spin rate is larger at the beginning of the jump and decreases throughout the jump.

To further validate the results of the selected collision model, the characteristics of the collision were investigated in more detail (small-scale level of validation). Niño and García (1998a) provided experimental information of the takeoff angles of the particles of $R_p$=60 to 90. In Fig. 3-12, the simulated results for the collision model with the best performance (Run G, Set 2) are compared with the experimental data obtained by Niño and García's work; the agreement is acceptable, within the experimental range, although the numerical results over-predict the data.

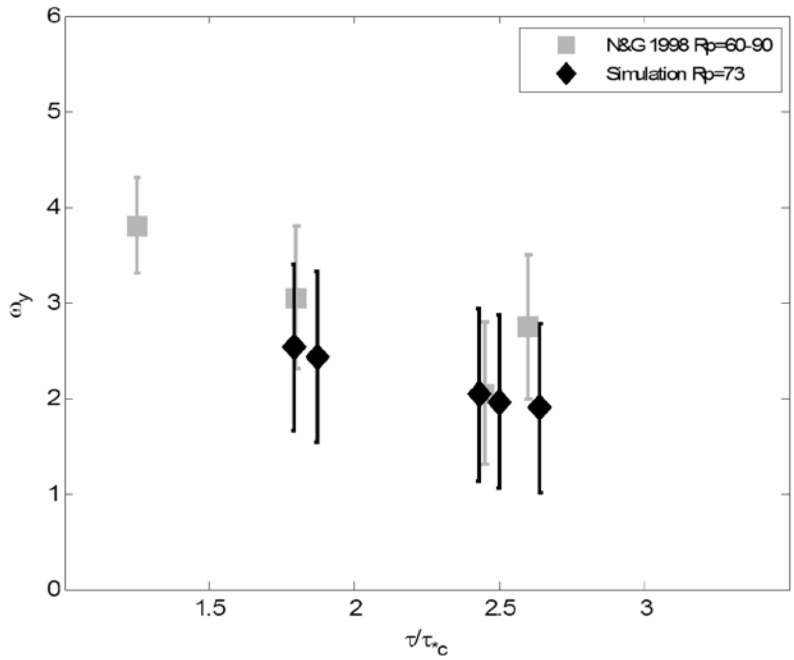


**Figure 3-11: Comparison of numerical results of particle angular velocity with Niño and García (1998a) data for $R_p$=73. Run G, Set 2.**

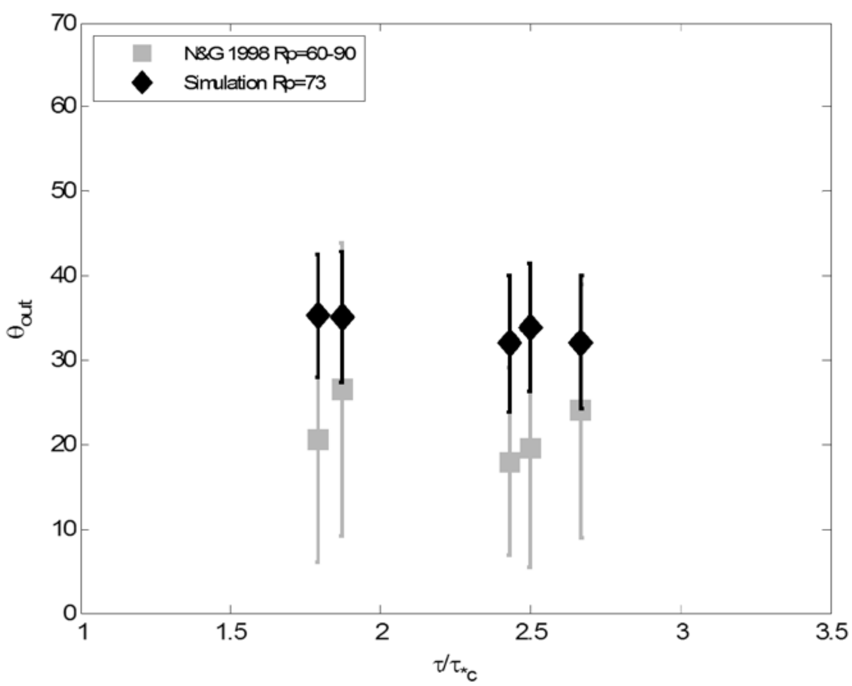


**Figure 3-12: Comparison of numerical results of takeoff angles with the experimental data of Niño and García (1998a) for $R_p$=73. Run G, Set 2.**

**Lateral particle motion**

The particle lateral deviation angle, $|\alpha_d|$, is defined as the absolute value of the angle of deviation of the particle in the x-y plane. A comparison with observations undertaken by Niño and García (1998a) is seen in Fig. 3-13 using numerical results of Run G, Set 2 (for $R_p$=73). In general terms, good agreement was found between the numerical simulation and the experimental results. The bed roughness model selected produced slightly larger lateral dispersion angles than the values found experimentally (Fig. 3-13a). The average value of the lateral deviation angle ($\alpha_d$) resulting from the simulation does not appear to depend strongly on the flow conditions, which agrees with the experimental data obtained by Niño and García (1998a). Niño and García suggested that the lateral deviation of particle trajectories might be produced by two different mechanisms: one associated with the initial conditions given by the rebound with the wall, and the other associated with cross-flow turbulent events. Both processes would occur simultaneously and the lateral deviation angle stays relatively constant in spite of the flow velocity increase. In our simulations, as the flow velocity increases, the mean particle stream-wise velocity increases (see Fig. 3-7c and 3-9c), and the span-wise component remains relatively constant (not shown). There is no other effect (like the presence of secondary currents or particle-particle collisions) that might counteract the shear flow effect on the deviation angle. A rather satisfactory agreement was also found in terms of the cumulative probability distribution function of the absolute of the deviation angle (Fig. 3-13b).

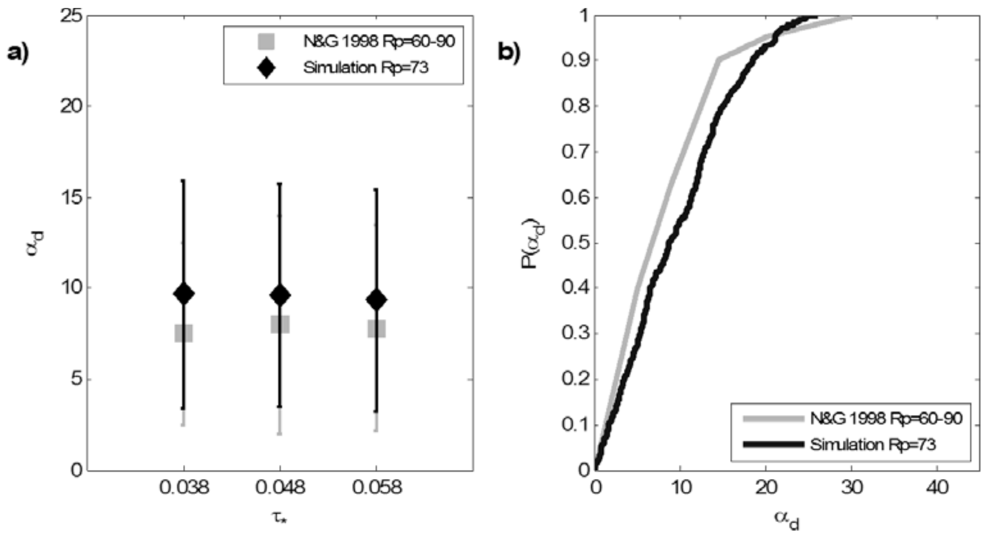


**Figure 3-13: Comparison of the absolute value of the deviation angle $\alpha_d$ obtained in the numerical simulation with experimental data by Niño and García (1998a). a) Absolute value of the deviation angle $\alpha_d$ of particle trajectories as a function of the flow condition. b) Cumulative probability distribution of the absolute value of the deviation angle.**

As a summary, the model that better approximated both sets of experimental results ($R_p = 73$ and $250$) was G2. Simulation results from G2 closely follow average jump height and length from Niño and García (1998) and Lee and Hsu (1994) data sets. Other variables such as lateral particle motion, span-wise particle angular velocity, and takeoff angle can be approximated to experimental results reasonably by the model. Also important is to mention that the simulation results suggest that the restitution and friction coefficients proposed by Schmeeckle et al. (2001), set 2 in Table 3-3, allow for better approximation to experimental values.

### 3.4.3. Assessment of the importance of forces in the particle motion

The importance of some components of each intervening force in the particle trajectory was analyzed in detail for particles with $R_p$=73 (Run G, Set 2). Fig. 3-14 shows the relative weight of each force expressed with respect to the total force exerted on the particle in the stream-wise ($x$) and wall-normal ($z$) directions, as a function of the particle jump trajectory on the horizontal plane. Fig. 3-14 presents three vertically arranged tiles showing: a) the average jump trajectory of the saltating particle in the $x-z$ plane, calculated among all jumps from the simulation after eliminating the first 20 jumps; b) the average behavior of each force component (normalized by the total force exerted on the particle) acting on the stream-wise direction (see Eq. (3-1)); and c) the wall-normal direction (see Eq. (3-2)).

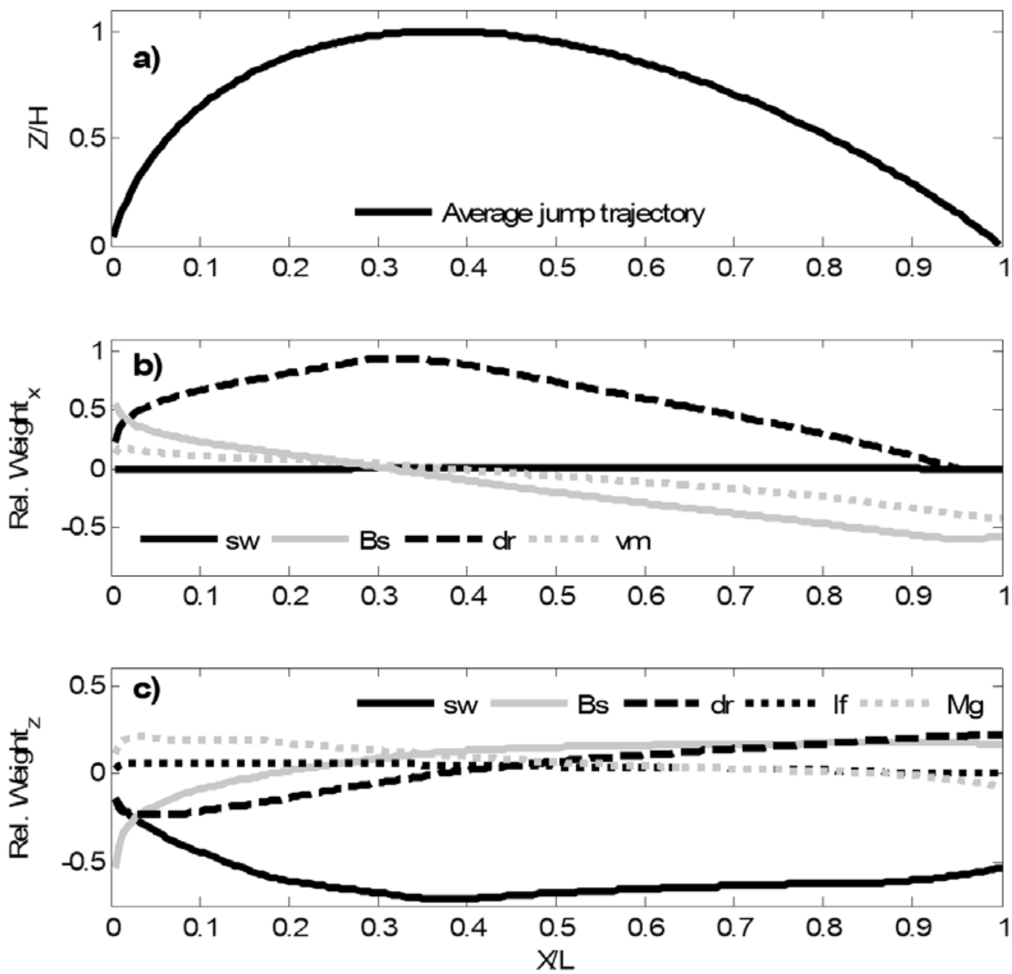


**Figure 3-14: Analysis of forces throughout an average jump. a) Average jump trajectory calculated among all jumps; b) average relative weight of each force acting on the stream-wise direction; b) average relative weight of each force acting on the wall-normal direction. Each force contribution is estimated by dividing each force by the total force acting on the direction analyzed. The forces shown include the forces of submerged weight (sw), Basset (Bs), drag (dr), virtual mass (vm), lift (lf), and Magnus (Mg). $R_p$=73. Run G, Set 2. $\tau_*/\tau_{*c}$=1.87.**

The figure shows the average values obtained when simulating the particle motion for 200 jumps (after subtraction of the first 20 jumps). The total force changes as the particle moves, so the percentages change, even if the force is constant throughout the entire time (such as the submerged weight force). A comparison of the location of the particle and the relative weight of each force at any point of the jump cycle can be made when comparing Figs. 3-14b and 14c with Fig. 3-14a.

In Fig. 3-14 b), it can be seen that the x-component of the drag force is driving the particle motion, and moving the grain in the stream-wise direction. The drag force achieves its maximum at the highest point on the jump (over 90% of the total force contribution). On the contrary, the drag force approaches zero when the particle is closer to the channel bed. This happens at the beginning and end of a single hop. The contribution of the stream-wise component of the submerged weight is very small, close to zero, when compared to the rest of the forces acting on the x-axis. The stream-wise component of the Basset force becomes important when the particle is closer to the channel bed. When the particle is at its highest point in the jump trajectory, the stream-wise component of the Basset force becomes zero. This could be explained by the larger relative acceleration of the saltating particle close to the wall. At the beginning of the jump, right after the particle had collided with the bed, the x-component of the Basset force accounts for more than 50% of the total forces, decreasing from there up to the point where it becomes almost negligible, when the particle reaches its highest point in a single jump, and then becoming negative and then going back to reaching a maximum contribution of over 50% of the total forces acting on the particle The latter happens at the last part of the jump, when the grain is coming down and getting closer to the wall. The stream-wise component of the remainder of the virtual mass force behaves similar as to the Basset force, but with a smaller magnitude. The remainder of the virtual mass attains a contribution of about 10% right after the particle has collided with the wall and a maximum contribution right before the particle collides with the wall (towards the end of the jump cycle) of about 40%. This can be explained due to the fact that the fluid velocity gradient with respect to the wall-normal direction is greater close to the wall (see Eq. (3-1)).

The contribution of the wall-normal components of the forces acting on the saltating grain (normalized by the total force acting on the particle) is shown in Fig. 3-14c) (see Eq. (3-2)). The wall-normal component of the submerged weight is by far the most important force acting on the particle. It starts smaller than other forces at the very beginning of the jump, but it quickly gains weight relative to the total force as the particle moves up in the jump trajectory. The submerge weight reaches its maximum when the particle is at its highest point, keeping its importance, although slightly decreasing, until the end of the jump. The submerged weight is the force trying to pull the particle towards the bed (that is why it is negative all throughout the jump), while the wall-normal components of the lift and Magnus (except at the very end of the jump) forces are trying to keep the particle suspended away from the wall (all of them with positive contributions). An important percentage of the vertical component of the submerged weight force (depending on the coefficient of restitution, *e*, used in the simulation) is converted into a positive vertical reaction that pushes the particle up, right at the moment of its collision with the wall (not shown in this Figure), causing the particle to begin a new jump. The wall-normal component of the drag force reaches its minimum when the particle is at its highest point (when it becomes zero), going from 20% to 0% and to 20%, at the beginning, highest point and end of the hop, respectively. This is obviously caused by the changes in the wall normal velocity, where it is positive as the particle goes up, it becomes zero at the highest point of the jump, and then it becomes negative when going down. The drag force in the wall-normal direction, then, acts in the opposite direction of the vertical velocity as a result of the resistance of the flow to the particle movement. The lift force reaches its maximum contribution at some distance from the beginning of the jump cycle, gradually losing its importance until it becomes negligible when the jump cycle is reaching its end. The vertical component of the Basset force becomes very important right after the particle has collided with the wall, where it reaches its maximum vertical acceleration (with a negative contribution), immediately after the particle has rebounded from the bed. The Magnus force plays a moderate role (contribution of about 20%) between the beginning of the jump and when the particle reaches its maximum height. Its behavior is dictated by the relative angular velocity of the particle.

In general, the drag force, in the stream-wise direction, and the submerged weight force, in the wall-normal direction, are the most important forces driving the particle motion (see Bombardelli and Jha, 2009), as shown in Figs. 3-15a and 3-15b. The Basset and virtual-mass forces become more important close to the bed, where the particle acceleration and the fluid velocity gradient are relatively large. The Basset force plays an important role when the particle starts a new jump, close to the wall; its importance decreases as the particle moves through the fluid. Since the events after collisions are crucial in particle saltation, the Basset force needs to be included among forces for sands; (see Bombardelli et al., 2008). On the other hand, the lift force plays a relatively smaller role.

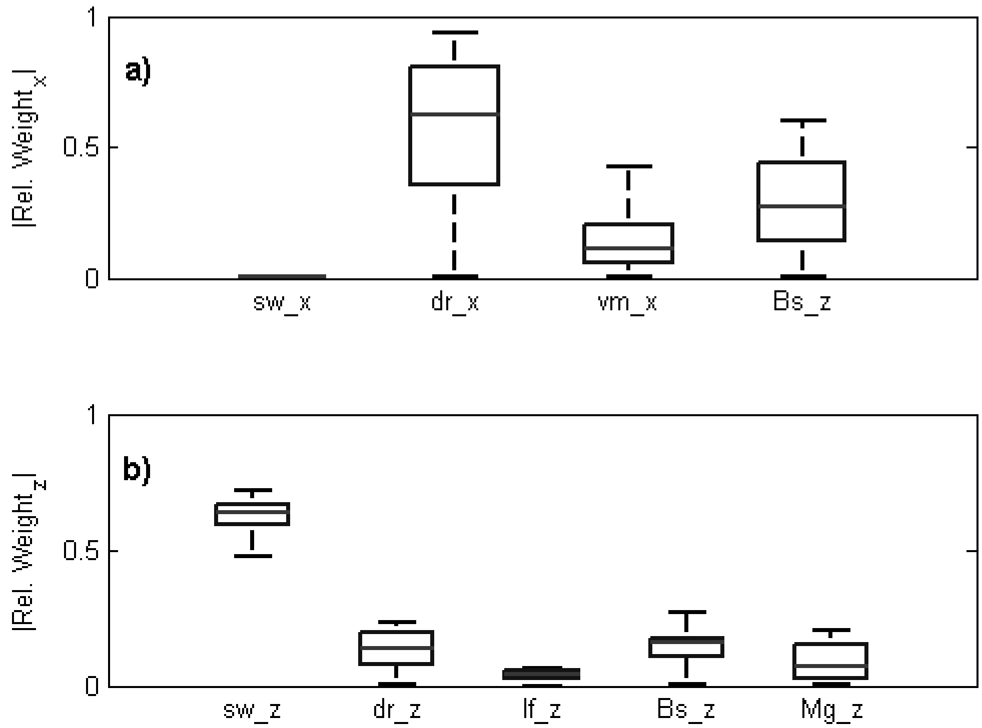


**Figure 3-15: Importance of each force relative to the total force acting on the saltating particle in absolute value. a) Boxplot of the average relative weight contribution of forces on the stream-wise direction; and on the b) wall-normal direction. Each box depicts a central mark (the median), a bottom edge (25th percentile), and top edge (75th percentile) of the simulation data. The whiskers show the most extreme data points that are not considered outliers. For clarity the outliers are not shown in the figure. $R_p$=73. Run G, Set 2. $\tau_*/\tau_{*c}$=1.87.**

### 3.4.4. Analysis of the model for the particle angular velocity

The 2D particle-tracking model proposed by Niño and García (1994) (Run A) uses an empirical expression to compute the particle angular velocity (Eq. (3-6)) and this effect is embedded in the calculation of the Magnus force.

$$\boldsymbol{\varpi_y = 5.11 - 1.13\frac{\tau_*}{\tau_{*c}}} \tag{3-6}$$

Extending the use of this model beyond its range of validity (even for particles sizes slightly smaller/larger than the ones used to obtain the empirical expression) may not necessarily provide accurate results. To evaluate this, numerical results were compared with the experimental data available, in terms of the mean particle jump length ($L$) and height ($H$) and the mean particle stream-wise velocity ($\overline{u}_p$).

The simulation results for Run A (not shown herein) and the experimental data available present two different trends. The experimental data show the expected trend between the dimensionless parameters ($H$, $L$ and $\overline{u}_p$) and the Shields parameter $\tau_*$: as the value of $\tau_*$ increases, the flow velocity increases and the particle is capable of describing jumps that are higher and longer and, therefore, the value of the dimensionless parameters increase. However, the numerical results for Run A show that there is a value of $\tau_*$ after which the dimensionless parameters no longer increase. By explicitly estimating the particle rotation at every time step using the Eq. (3-4), as done in Run D to Run H, the numerical results trend is concomitant with the experimental trend, as shown in Fig. 3-11. When switching on and off the lift, Basset, and virtual mass forces, a change in the magnitude of the dimensionless parameters ($H$, $L$ and $\overline{u}_p$) is observed, but there is still a value of $\tau_*$ after which the dimensionless parameters no longer increase. However, when turning off the Magnus force, as the friction velocity increases, the value of each dimensionless parameter ($H$, $L$ and $\overline{u}_p$) increases. Therefore, the Magnus force is responsible for the model behavior.

Fig. 3-16 shows the average relative weight of the Magnus force with respect to the total force for different wall-friction (shear) velocity values, when the particle changes position in an average jump. Three tiles are shown in the figure: the upper tile shows the particle trajectory for an average jump in the $x - z$ plane, the middle tile depicts the relative weight of the Magnus force in the wall-normal direction when using Eq. (3-6) (empirical equation), and the bottom tile shows the relative weight of the Magnus force in the wall-normal direction when using Eq. (3-4). The average jump trajectory was obtained averaging all jumps in the simulation (after eliminating the first 20 jumps). The same concept was used to obtain the average weight of the Magnus force relative to the total force applied to the particle in the wall-normal direction. The sign of the Magnus force depends on the difference between the particle rotation and the value of the derivative of the stream-wise fluid velocity with respect to the wall-normal direction, evaluated at the elevation where the particle is located (see Eq. (3-2)). When using the Niño and García empirical Eq. (3-6), for smaller values of the friction velocity ($\tau_*/\tau_{*c}$ less than 3), the value of particle angular velocity is larger than the value of the fluid velocity derivative at every point in the vertical. In this case, the sign of the Magnus force is positive and it is maintained across the wall-normal direction. As the value of the shear stress increases, the rotation of the particle decreases, as calculated by using the empirical expression and, eventually, the fluid velocity derivative close to the bed (where this value is larger) becomes larger than the particle angular velocity. Thus, the sign of the Magnus force switches from positive to negative when the particle is close to the bed as seen at the very end of the jump in Fig. 3-16b for a shear stress ratio of 3. When the particle moves away from the wall, the value of the fluid velocity derivative becomes smaller and the Magnus force becomes positive again. This change of sign significantly affects the particle acceleration, and therefore the particle trajectory. If the Magnus force has a positive sign, it increases the particle acceleration, making the particle travel further away. On the other hand, when the Magnus force becomes negative, the particle acceleration becomes reduced and so does the jump length and height. If instead Eq. (3-4) is used to compute the particle angular velocity, all shear stresses simulated are going to cause the Magnus force to become negative near the wall, as observed in Fig. 3-16c, causing a deceleration of the particle right before it collides with the wall. Another important aspect of the analysis can be noticed when using Eq. (3-6) to calculate the particle rotation, the average relative weight of the Magnus force throughout the jump reduces its importance as the shear stress increases (Fig. 16b), while when using Eq. (3-4) the average relative weight becomes independent from the flow intensity. Although the shape of the curve described by the relative weight of the Magnus force throughout the jump seems to be similar in both cases, the maximum contribution is slightly smaller in flows with lower shear stresses. Since Eq. (3-4) is time dependent and does not come from experimental regressions, and therefore not limited to a specific range of particle diameters used in a specific experiment, it seems reasonable to think it is better suited to calculate the particle angular velocity for saltating particles in bed-load motion. From the previous results, the computation of the rotation of the particle is a key factor to correctly estimate the value of the Magnus force, which has been addressed successfully by Runs E to H.

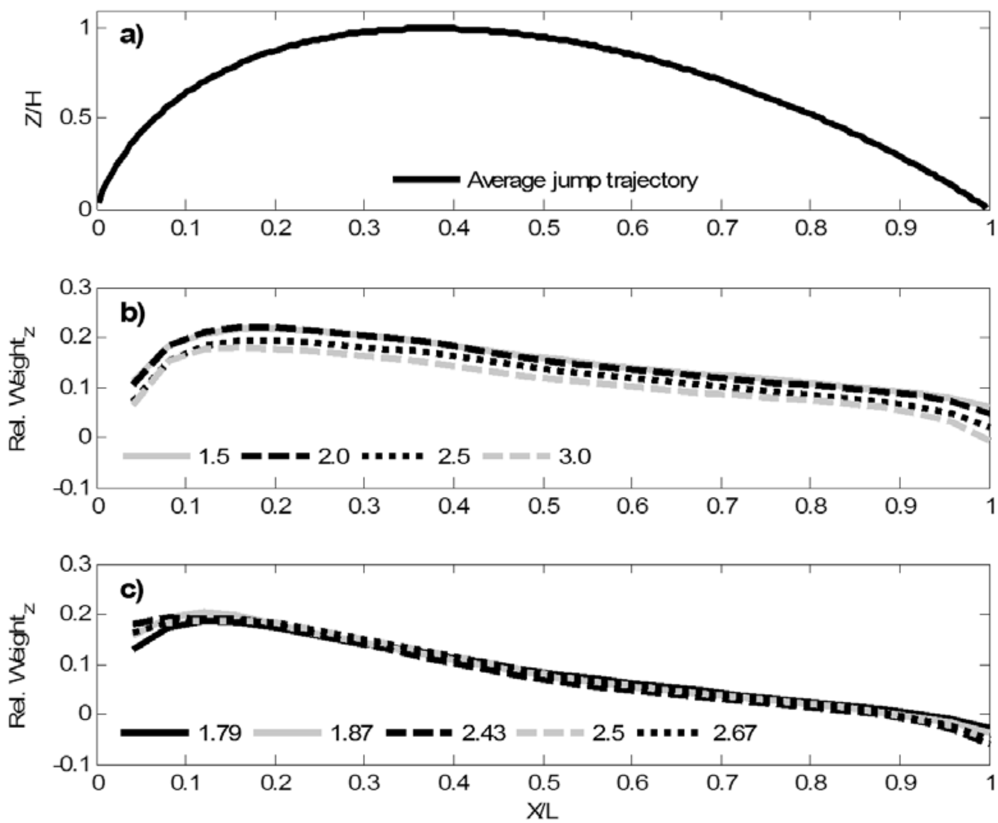


**Figure 3-16: Average variation of the Magnus force (relative to the total force on the wall-normal direction) along the average jump trajectory for different shear stress ratios. a) Average relative weight of the Magnus force using Eq. (3-6) (empirical expression) to compute the particle angular velocity; b) average relative weight of the Magnus force using Eq. (3-4) (time dependent formulation) to compute the particle angular velocity. $R_p$=73. Run G, Set 2.**

### 3.4.5. Verification of particle diffusion

The nature of bed-load transport of sediment particles in rivers and channels is diffusive (Nikora et al., 2001), and therefore all models focusing on particle saltation should reproduce this diffusion. Particle diffusion is associated with the level of scattering of the saltating particles in the stream and span-wise directions, and a mathematical representation of the particle diffusion or scattering may help to evaluate if a particular model is capable of reproducing this phenomenon. One way to corroborate the level of scattering generated by the models proposed in this study, is to follow the approach presented by Nikora et al. (2001, 2002):

$$\langle \boldsymbol{X'^2} \rangle = \boldsymbol{\alpha_x t^{2\gamma_x}} \tag{3-7}$$

$$\langle \boldsymbol{Y'^2} \rangle = \boldsymbol{\alpha_y t^{2\gamma_y}} \tag{3-8}$$

where $\langle X'^2 \rangle$ and $\langle Y'^2 \rangle$ are the second order moments of the location of the particle in the stream-wise and span-wise directions, respectively, which represent the diffusion of particles over time in either direction; $\alpha_x$ and $\alpha_y$ are constants; $X' = X - \langle X \rangle$, $Y' = Y - \langle Y \rangle$; angular brackets denote ensemble averaging. The exponents $\gamma_x$ and $\gamma_y$ dictate the state of diffusion (Nikora et al., 2001, 2002) by describing the degree of inclination of the slope of the diffusion plot, namely sub-diffusion ($\gamma$ < 0.5), normal diffusion ($\gamma$ =0.5), super-diffusion ($\gamma$ > 0.5), and ballistic diffusion ($\gamma$ =1). When $\gamma \approx 0$ there is no diffusion or scattering on that particular direction. The larger the value of $\gamma$ the greater the scatter of the particles.

Three different ranges have been identified in the conceptual model suggested by Nikora et al. (2001, 2002): Local range, intermediate range, and global range. For saltation, the local range represents the particle trajectory between two successive collisions with the bed, equivalent to what we call the “free flight” stage; the intermediate range is composed by several local trajectories up to the point where the saltating particle stops and lies in the bed motionless, where the period of rest begins; while the global range is composed by several intermediate trajectories, including several periods of rest, entrainment and deposition from and to the channel/river bed. Figure 3-17 shows the results of particle diffusion (scattering) in both the stream-wise and span-wise directions following Nikora et al.’s methodology, for $R_p$ =73, Run G, Set 2.

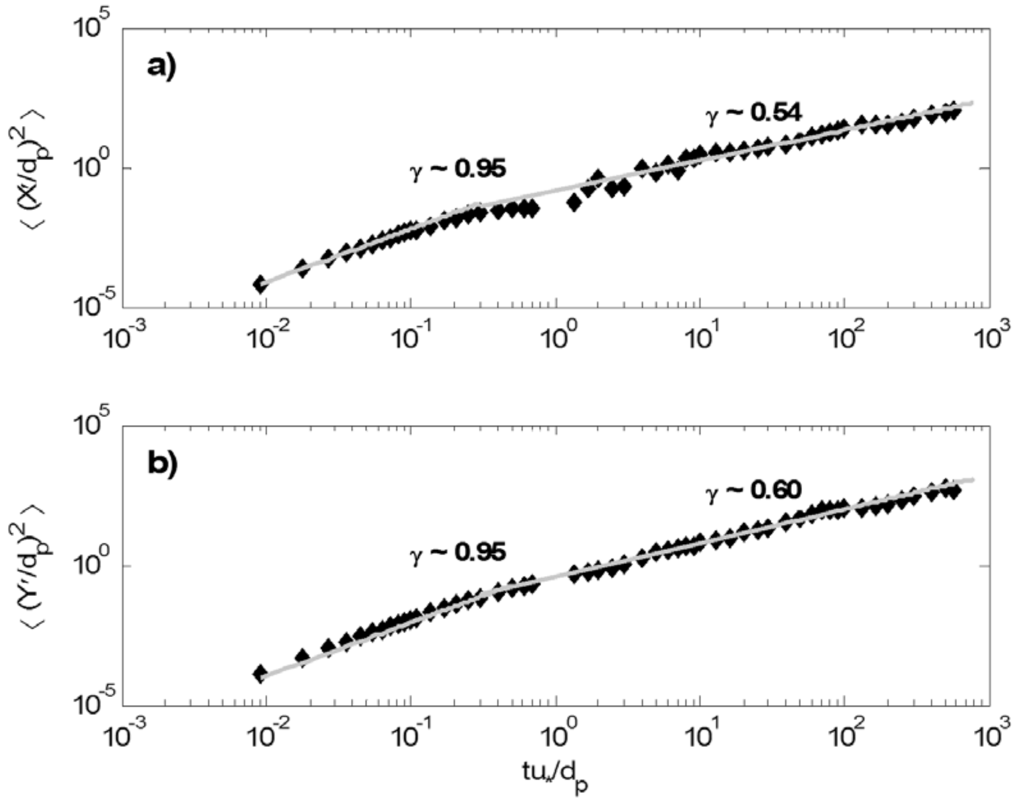


**Figure 3-17: Non-dimensional time evolution of the second order moment of particle position (particle diffusion): a) In the stream-wise (x-direction), and b) the span-wise direction (y-direction). $R_p$ =73. Run G, Set 2. $\tau_*/\tau_{*c}$ =1.87.**

As it can be seen both figures show clearly the local and intermediate ranges (the simulations presented in this work have not been intend to reproduced the global range). The local range corresponds to the slopes on the left of Fig. 3-17 a) and b), both of which show nearly ballistic diffusion ($\gamma \approx 1$). A difference between slopes becomes clear when analyzing the intermediate range (second slope from left to right). According to Fig. 3-17a, in the stream-wise direction the particle scattering is virtually normal ($\gamma \approx 0.5$), while in the span-wise direction the particle scattering can be categorized as super-diffusive ($\gamma > 0.5$). In both cases, the stream and span-wise directions, it is evident that the model reproduces diffusion ($\gamma \neq 0$), with similar outcomes to those presented by Nikora et al. (2001, 2002), Bialik et al. (2012), and Moreno and Bombardelli (2012), validating the model with respect to particle scattering.

# APPENDIX 3-A: García and Niño (1992) model for particle rebound with the wall

The striking particle velocity is resolved using normal and tangential components with respect to the collision surface, $u_n|_{in}$ and $u_t|_{in}$, respectively. It is assumed that these components after the rebound, $u_n|_{out}$ and $u_t|_{out}$, are reduced in a way that (Tsujimoto and Nakagawa, 1983),

$$u_n|_{out} = -e\ u_n|_{in} \qquad\qquad u_t|_{out} = f\ u_t|_{in} \tag{3A-1}$$

In the equations above, $e$ and $f$ denote the restitution and friction coefficients, respectively. In such a case, the particle rebounds with an angle $\theta_r$ given by:

$$\tan(\theta_r) = \frac{e}{f}\tan(\theta_{in} + \theta_b) \tag{3A-2}$$

The particle's dimensionless velocity components in the stream-wise and wall-normal directions immediately after the rebound, denoted as $\hat{u}_p$ and $\widehat{w}_p$, respectively, can be expressed in terms of the particle's dimensionless velocity components immediately before the collision (denoted by $\tilde{u}_p$ and $\widehat{w}_p$) as follows:

$$\boldsymbol{\hat{u}_p = f\ (\tilde{u}_p{}^2 + \widetilde{w}_p{}^2)^{0.5} \cos(\theta_{in} + \theta_b) \frac{\cos(\theta_r + \theta_b)}{\cos(\theta_r)}} \tag{3A-3}$$

$$\widehat{w}_p = f\ (\tilde{u}_p{}^2 + \widetilde{w}_p{}^2)^{0.5} \cos(\theta_{in} + \theta_b) \frac{\sin(\theta_r + \theta_b)}{\cos(\theta_r)} \tag{3A-4}$$

# APPENDIX 3-B: Tsuji et al. (1985) model for particle rebound with the wall

A particle slides if expression (3B-1) below is satisfied (Crowe et al., 2011):

$$\frac{\widetilde{w}_p}{|\widetilde{U}|_{in}|} < \frac{-2}{7f\ (e+1)} \tag{3B-1}$$

where $\left|\widetilde{U}|_{in}\right|$ is the modulus of the particle velocity vector before the collision with the wall. If the criterion is met, i.e., if the particle slides, the post-collision velocities for the stream-wise, the span-wise and wall-normal directions are calculated as follows (Crowe et al., 2011; hard-sphere model):

$$\hat{u}_p = \frac{5}{7}\ (\tilde{u}_p - \frac{2a}{5}\widetilde{\varpi}_y)\ ; \qquad \hat{v}_p = \frac{5}{7}\ (\tilde{v}_p - \frac{2a}{5}\widetilde{\varpi}_x); \qquad \widehat{w}_p = -e\ \widetilde{w}_p \tag{3B-2}$$

$$\widehat{\varpi}_x = \frac{\tilde{v}_p}{a}; \qquad \widehat{\varpi}_y = -\frac{\tilde{u}_p}{a}; \qquad \widehat{\varpi}_z = \widetilde{\varpi}_z \tag{3B-3}$$

where $\varpi_x$, $\varpi_y$ and $\varpi_z$ indicate the components of the particle rotation vector along the stream-wise, span-wise and wall-normal directions, respectively, before the collision; and $a$ denotes the particle radius. If the particle does not slide, i.e., if the criterion in (3B-1) is not met, the post-collision velocities are calculated as:

$$\hat{u}_p = \tilde{u}_p + \varepsilon_x f(e+1)\widetilde{w}_p; \quad \hat{v}_p = \tilde{v}_p + \varepsilon_y f(e+1)\widetilde{w}_p \quad \widehat{w}_p = -e\ \widetilde{w}_p \tag{3B-4}$$

$$\widehat{\varpi}_x = \widetilde{\varpi}_x - \frac{5}{2a}\varepsilon_y f(e+1)\widetilde{w}_p; \quad \widehat{\varpi}_y = \widetilde{\varpi}_y + \frac{5}{2a}\varepsilon_x f(e+1)\widetilde{w}_p; \quad \widehat{\varpi}_z = \widetilde{\varpi}_z \tag{3B-5}$$

where the coefficients $\varepsilon_x$ and $\varepsilon_y$ are defined as $\varepsilon_x = \left(\tilde{u}_p + a\widetilde{\varpi}_y\right)/\left|\widetilde{U}|_{in}\right|$ and $\varepsilon_y = \left(\tilde{v}_p + a\widetilde{\varpi}_x\right)/\left|\widetilde{U}|_{in}\right|$. They satisfy the relation ${\varepsilon_x}^2 + {\varepsilon_y}^2 = 1$. Eqs. (3B-1) to (3B-5) are developed for a horizontal contact plane between the flying particle and the bed, and their derivation is fully described in Crowe et al. (2011).

# CHAPTER 4

# 3D NUMERICAL SIMULATION OF PARTICLE-PARTICLE COLLISIONS IN SALTATION MODE NEAR STREAM BEDS

## 4.1. INTRODUCTION

The motion of particles as bed load describing consecutive "hops" in a fluid flow near a granular bed is called saltation (Graf, 1971; Yalin, 1977; Parker, 2004; García, 2008; Julien, 2010). Generally speaking, both sand and gravel can be subjected to bed-load transport (García, 2008; Julien, 2010).

In spite of their extended presence in most streams of the planet, our understanding of the interactions among sediment (of finite size, in flows of large Reynolds numbers), flow and turbulence is still limited, to the point that this constitutes one of the unresolved topics belonging to the field of two-phase flow mechanics. Considering that this flow involves the motion of a carrier fluid with solid particles interspersed, the most comprehensive simulation strategy we could follow consists in: a) solving the mass and momentum (Navier-Stokes) equations in the space in between particles in three dimensions (3D); b) updating the position of the particles; c) remeshing; and d) solving again the equations of fluid motion with the new position of the particles (see Chung, 2002). This paradigm is clearly impractical for industrial purposes for particles of finite size, given the need of very fine meshes to resolve all scales of turbulence in a Direct Numerical Simulation (DNS), and due to the remeshing process, which is very time consuming. Very recently, Lin et al. (2011, 2012) developed a model in finite volumes where a similar strategy to this was used, albeit with a different treatment of particles. Lin et al.'s model is based on a direct-forcing method to capture the particle motions and their interaction with the flow.

Given the difficulties in addressing particles of finite size in a flow, several authors in the last decade have produced alternative solutions (Wiberg and Smith, 1985; García and Niño, 1992; Lee and Hsu, 1994; Niño and García, 1994; Niño and García, 1998b; Lee et al., 2002; Schmeeckle and Nelson, 2003; Harada and Gotoh, 2006; Lee et al., 2006; Lukerchenko et al., 2006 and 2009a; González, 2008; Bombardelli et al., 2008; Bialik, 2011; Bialik et al., 2012; Bombardelli et al., 2014). Overall, those models have been shown to provide adequate responses for the analysis of saltation, namely, for the computation of useful statistics of particle jump height and length, particle horizontal velocity and, very importantly, for the estimation of bed-load transport rates. To the best of the authors' knowledge, only Lee et al. (2002), González (2008) and Bialik (2011) have considered particle-particle collisions (inter-particle collisions) in their models.

Particle-particle collisions are usually addressed using two models, the hard-sphere and the soft-sphere model (Crowe et al., 2011). The hard-sphere model is easier to use, but only applicable to binary collisions. The soft-sphere model allows for collisions among more than two particles, yet it is computationally more demanding. Herein, the hard-sphere model is used. This same model can be applied to both particle-particle collisions and particle collisions with the bed. Basically, particle collisions with the bed can be thought as a particle-particle collision, where one particle is infinitely large (i.e., the bed). In essence, the pre-collision linear and angular velocities can be used to calculate the post-collisions counterparts, in addition to known values for the restitution and friction coefficients.

Nikora et al. (2002) suggested that sediment transport near the bed is diffusive in nature. Particle diffusion, scattering or dispersion in bed-load transport refers to the spreading of sediment grains while moving close to the bed. Particle diffusion is expected to occur in the plane parallel to the bed ($X$ and $Y$ directions), and it can be described mathematically by the evolution in time of the central moments of particle location (Nikora et al., 2001 and 2002). Particularly useful is the analysis of the second order moment. Further discussions regarding these concepts can be found in Nikora et al. (2001) and Bialik et al. (2012); in those works, collisions among particles were left outside of the analysis.

Particle-particle collisions are acknowledged to gain importance as particle concentration increases (Brennen, 2009; Crowe et al., 2011); however, there are still numerous knowledge gaps regarding to what extent inter-particle collisions influence the particle scattering and trajectory. In particular, the following questions arise:

a) What is the effect of particle collision on the average jump length and height, and on the ranges of those variables?
b) What is the precise effect of bed-load concentration on inter-particle collisions?
c) What is the role of flow intensity and particle size on the process of collisions?
d) What is the effect of inter-particle collisions on particle diffusion?

One way to assess these queries is through the analysis of results of three-dimensional (3D) numerical simulations of saltation near the bed, which explicitly incorporate the particle collision phenomenon. This approach is followed herein using an averaged turbulent velocity field (logarithmic velocity profile) pertaining to an open-channel flow. Sediment particles are assumed to be spheres located far away from lateral walls at all times within the range of sands.

Two different initial relatively small particle concentrations are analyzed to examine differences in particle movement characteristics, collision frequencies and their changes under three different flow intensities, and two particle sizes (within the sand range). To assess the importance of particle-particle collisions, each run is carried out for two cases: i) including and ii) neglecting collisions. The model is initially validated by considering the motion of one particle with experimental data from Niño and García (1998a) and Lee and Hsu (1994).

## 4.2. MODEL DESCRIPTION

A 3D computational model developed at UC Davis (González, 2008; Bombardelli et al., 2008; Bombardelli et al., 2010; Moreno et al., 2011, Bombardelli et al., 2014) was modified and exploited to simulate the saltating motion of multiple particles close to the bed of an open channel. The 3D model has three major sub-models (Bombardelli et al., 2014): i) a sub-model for particle free flight, ii) a sub-model for particle collision with the bed, and iii) a sub-model for particle-particle collision, which are described as follows.

### 4.2.1. Sub-model for particle free flight

The particle free flight is calculated using the equation of linear momentum in the three Cartesian coordinate axes, namely the stream-wise (*X*), span-wise (*Y*) and wall-normal (*Z*) axes. The equations are made dimensionless by considering the particle diameter, $d_p$, and the shear velocity, $u_*$, as the length scale and velocity scale, respectively (see González, 2008):

$$\frac{du_p}{dt} = \alpha \frac{\sin\theta}{\tau_*} - \frac{3}{4}\alpha C_D \left(u_p - u_f\right)\left|\vec{u}_r\right| + \alpha C_m w_p \frac{du_f}{dz} + \frac{9\alpha}{\sqrt{\pi R_p}\,\tau_*^{1/4}} \int_0^t \frac{d}{d\tau}\left(u_f - u_p\right)\frac{d\tau}{\sqrt{t-\tau}} \tag{4-1}$$

$$\frac{dw_p}{dt} = -\alpha \frac{\cos\theta}{\tau_*} - \frac{3}{4}\alpha C_D\, w_p \left|\vec{u}_r\right| + \frac{3}{4}\alpha C_L \left( \left|\vec{u}_r\right|_T^2 - \left|\vec{u}_r\right|_B^2 \right) - \frac{9\alpha}{\sqrt{\pi R_p}\, \tau_*^{1/4}} \int_0^t \frac{d}{d\tau} w_p \frac{d\tau}{\sqrt{t-\tau}}$$
$$+ \frac{3}{4}\alpha \left|\vec{u}_r\right| \left( \varpi_y - \frac{1}{2}\frac{du_f}{dz} \right) \tag{4-2}$$

$$\frac{dv_p}{dt} = -\frac{3}{4}\alpha\, C_D\, v_p \left|\vec{u}_r\right| - \frac{9\alpha}{\sqrt{\pi R_p}\, \tau_*^{1/4}} \int_0^t \frac{d}{d\tau} v_p \frac{d\tau}{\sqrt{t-\tau}} \tag{4-3}$$

where $u_p$, $v_p$, and $w_p$ represent the dimensionless particle velocity in the stream-wise, span-wise, and wall-normal directions; $u_f$ is the fluid velocity in the stream-wise component; $\vec{u}_r$, $\vec{u}_{rT}$ and $\vec{u}_{rB}$ denote the relative velocity vectors at the center, top and bottom of the particle, respectively; $\alpha = (1 + R + C_m)^{-1}$, $C_m$ is the virtual mass coefficient,$R = \rho_s/\rho_w$-1 is the submerged particle specific gravity, where $\rho$ and $\rho_s$ are the fluid and particle density, respectively. We use $\tau_* = u_*^2/(gRd_p)$ to represent the Shields parameter; $g$ is the acceleration of gravity; $R_p = (Rgd_p^3)/\nu$ is the explicit particle Reynolds number, where $\nu$ is the kinematic water viscosity; $\theta$ is the angle of the channel bed with respect to a horizontal plane; $\varpi_y = \omega_y d_p / u_*$ indicates the dimensionless component of the particle rotation vector in the span-wise direction, and $\omega_y$ denotes the dimensional particle angular velocity in the span-wise direction ; $t$ represents time; $\tau$ is a dummy variable for integration; and $Z$ denotes the wall-normal direction; $C_L$ and $C_D$ are the lift and drag coefficients, respectively. The operator $d(\cdot)/dt$ expresses the material derivative using the particle velocity.

In order to obtain Eqs (4-1) to (4-3), we made the following hypotheses: i) the flow field is uniform in the span-wise direction; ii) the only gradient in velocity occurs in the wall-normal direction; iii) the components in the span-wise and wall-normal directions of the virtual-mass force are neglected; iv) only the wall-normal component of the lift force is considered; v) since the most important component of the particle relative rotation vector is $\varpi_y$ (this was corroborated by González, 2008, through several computational tests), only the wall-normal component of the Magnus force is considered.

The drag coefficient, $C_D$, was calculated using the expression proposed by Yen (1992):

$$C_D = \frac{24}{\mathrm{Re}_p}(1 + 0.15\sqrt{\mathrm{Re}_p} + 0.017\,\mathrm{Re}_p) - \frac{0.208}{1 + 10^4\,\mathrm{Re}_p^{-0.5}} \tag{4-4}$$

where $Re_p = w_s d_p / \nu$ is the particle Reynolds number, and $w_s$ is the particle fall velocity. For simplicity, the value of the virtual mass coefficient was assumed to be $C_m =$ 0.5, following other particle tracking models (Niño and García, 1994 and 1998b; Schmeeckle and Nelson, 2003; Lukerchenko et al., 2006; González, 2008). The lift coefficient was assumed to be $C_L =$ 0.2, as suggested by Wiberg and Smith (1985). The non-dimensional particle rotation vector, $\vec{\varpi}$, is numerically computed at each time step using the expression proposed by Yamamoto et al. (2001):

$$\frac{d\vec{\varpi}}{dt} = -C_t \frac{15}{16\pi} |\vec{\varpi}_r| \vec{\varpi}_r \tag{4-5}$$

where $C_t = C_1 / \sqrt{Re_r} + C_2 / Re_r + C_3\, Re_r$ is a non-dimensional coefficient, $Re_r = d_p{}^2 |\varpi_r| / 4\nu$ is the Reynolds number of the rotational motion; the coefficients $C_1, C_2$ and $C_3$ are obtained from the table presented in Yamamoto et al. (2001; see also, Bombardelli and Moreno, 2012), and $\vec{\varpi}_r$ is the non-dimensional relative particle rotation vector with respect to the fluid vorticity.

The numerical integration of the Basset force expression is particularly complex, because the integral becomes singular at the upper limit. In order to avoid this limitation, the calculation of the Basset term was implemented following the methodology proposed by Bombardelli et al. (2008). It is worth mentioning here that the Basset methodology is first order accurate in time (Hinsberg et al., 2011). To obtain the particle velocity and rotation, Eqs. (4-1) to (4-4) were numerically integrated using the standard fourth-order Runge-Kutta method (Isaacson and Keller, 1966).

### 4.2.2. Sub-model for particle collision with the bed

This sub-model algorithm can be considered as an extension to 3D of the model by García and Niño (1992). The incident angles ($\theta_{in}$) in the stream-wise direction and in the span-wise direction (defining the 3D behavior of the sediment motion) are calculated using the particle velocity right before the collision with the wall. Then, a trigonometric relation is established through the angle between the tangent to the particle on the bed (considered to be a sphere for simulation purposes) at the impact point and the channel surface. This trigonometric relation, for the vertical plane, can be written as follows:

$$\frac{r_1}{d_p} = \frac{1}{2}\left[\cos(\theta_b) - \tan(\theta_{in})\sin(\theta_b)\right] \tag{4-6}$$

where $r_1/d_p$ (see Fig. 4-1) is defined through a random number generator uniformly distributed between 0.1 and 0.5 (for angle description see Fig. 4-1). Therefore, the value of $\theta_b$ can be calculated from $\theta_{in}$ and $r_1/d_p$ instead of obtaining them through the use of a random distribution.  The lateral angle is obtained in the same manner. The bed is assumed to be composed by uniformly packed spheres placed one next to the other, while the particle diameter

$d_p$ is equal for moving and resting spheres. The trigonometric relation for the span-wise direction can be obtained using a similar expression to equation (6).

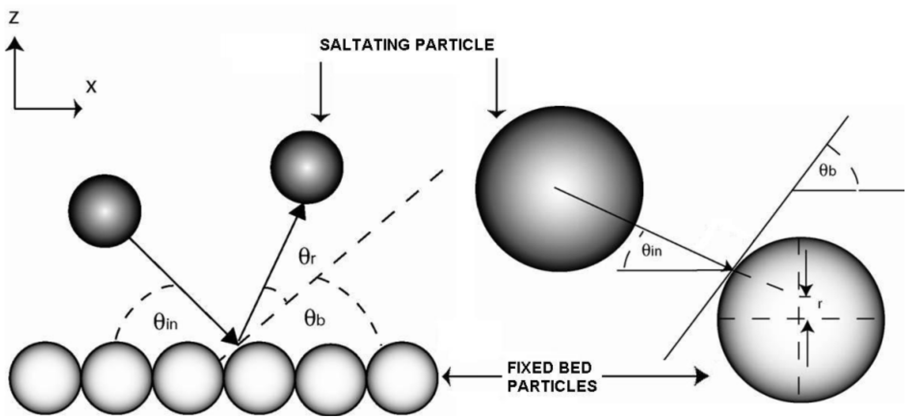


**Figure 4-1: Schematic of the collision of a particle with the bed in a vertical plane. a) View from a side. b) $\theta_{in}$ is defined from the incident velocity of the particle, right before collision with the wall; and $\theta_b$ denotes the angle between the plane tangent to the point of impact and the bed (adapted from Bombardelli et al., 2008).**

Once $\theta_b$ has been obtained, the normal and tangential components of the particle velocity are calculated as a function of coefficients of restitution ($e$) and friction ($f$), and a rebound sub-model is applied. This sub-model considers the conservation of linear and angular momentum before and after the particle collision with the bed. The rebound sub-routine used in this work is based on the equations developed by Crowe et al. (2011). These equations are applied using the hard-sphere model in a similar way to those applied for the particle-particle collisions, which are explained in the following section.

### 4.2.3. Sub-model for particle-particle collision

The inter-particle collision sub-model is based on the conservation of linear and angular momentum. The algorithm builds upon the equations discussed in Crowe et al. (2011), which allow for the calculation of the post-collision linear and angular velocities in terms of the information available before the impact between the particles. A hard-sphere model is assumed, where only collisions between two particles are considered. The latter is valid for relatively low particle concentrations (Crowe et al., 2011), which is the range we analyze in this chapter.

Post-collision velocities for random particles $i$ and $j$ are indicated herein with the superscript ^; they can be calculated using the following expressions based on the particle velocities just before the collision (which are denoted by the superscript ~):

$$\vec{\hat{u}}_{pi} = \vec{\tilde{u}}_{pi} + \frac{\vec{J}}{m_i} \qquad \vec{\hat{u}}_{pj} = \vec{\tilde{u}}_{pj} - \frac{\vec{J}}{m_j} \tag{4-7}$$

$$\vec{\hat{\varpi}}_i = \vec{\tilde{\varpi}}_i + \frac{d_p}{2}\vec{n} \times \frac{\vec{J}}{I_i} \qquad \vec{\hat{\varpi}}_j = \vec{\tilde{\varpi}}_j + \frac{d_p}{2}\vec{n} \times \frac{\vec{J}}{I_j} \tag{4-8}$$

where $\vec{J}$ is the impulse of the force exerted on particle $i$ during the collision, and $\vec{n}$ is the normal unit vector directed away from the centre of the particle $i$ to the contact point with particle $j$, as shown in Fig. 4-2. Assuming spherical particles, and considering known values for the coefficients of restitution ($e$) and friction ($f$), $\vec{J}$ can be calculated as (Tanaka and Tsuji, 1991):

$$\vec{J} = J_n \vec{n} + J_t \vec{t} \tag{4-9}$$

$$J_n = (1+e)\vec{n} \cdot \vec{c}\left( {m_i}/{2} \right) \tag{4-10}$$

$$J_t = -f\, J_n \tag{4-11}$$

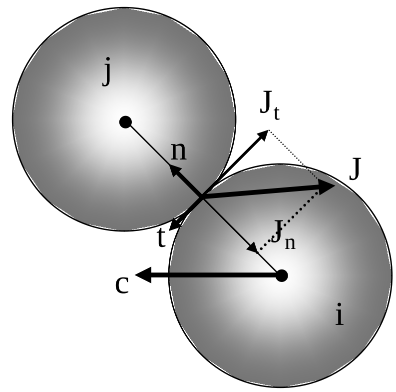


**Figure 4-2: Representation of the binary inter-particle collision. Definition of parameters shown in Eqs. (4-7) through (4-11).** $c$ **represents the relative velocity between particles after the collision.**

In Eqs. (4-7) to (4-11), $J_n$ and $J_t$ denote the normal and tangential component of the impulse, respectively; $\vec{t}$ and $\vec{n}$ represent the tangential and normal unit vectors in the direction of the slip velocity, respectively, given by $t = \vec{c}_{fc} \big/ \left|\vec{c}_{fc}\right|$. The variable $\vec{c}$ corresponds to the relative velocity of the mass centre $\vec{c} = \vec{\tilde{u}}_j - \vec{\tilde{u}}_i$, while the variable $\vec{c}_{fc}$ is the slip velocity between particle surfaces, that can be defined as:

$$\vec{c}_{fc} = \vec{c} - \left(\vec{c} \cdot \vec{n}\right)\vec{n} - \frac{d_p}{2}\vec{\tilde{\varpi}}_i \times \vec{n} - \frac{d_p}{2}\vec{\tilde{\varpi}}_j \times \vec{n} \tag{4-12}$$

### 4.2.4. Bed-load entrainment and deposition

According to Drake et al. (1998) entrainment occurs when a formerly motionless particle has an uninterrupted net motion of one particle diameter in the horizontal direction, as also noted by Bialik et al. (2012). In spite of the motion of one-particle diameter, entrainment of a motionless bed particle into bed-load layer has not been the focus of this model this far. Future steps in this project will consider the entrainment and deposition phenomena, once a highly resolved velocity profile is coupled to the simulations instead of the logarithmic law of the wall.

So far the saltation model has been used to address the physics of particle saltation, particularly during the particle "free flight" stage, particle collisions with the bed (González, 2008; Bombardelli at al., 2010; Bombardelli et al., 2014), and collisions among particles (current chapter). Therefore, all simulations consider the bed to be fixed, i.e., no particles are allowed to move from the bed, while moving particles are released from an initial point, with an initial velocity and rotation different from zero. Hence, all particles in saltation start the simulation as moving particles, and no motionless particles are suddenly put into motion during the simulation.

## 4.3. THREE-DIMENSIONAL SIMULATION OF SALTATING PARTICLES

### 4.3.1. Model Validation

The model presented in the previous sections has been validated via comparisons with laboratory data for a single saltating particle. González (2008) developed comparisons with two datasets in terms of jump length and height, and Bombardelli et al. (2008 and 2014) reported comparisons in terms of results of trajectories.

Herein, the validation of the 3D saltation model for a single saltating particle was developed through comparisons with the experimental data of Niño and García (1998a) and Lee and Hsu (1994), for values of $R_p$=73 and 250, respectively. Conditions pertaining to three different flow intensities (represented via the flow shear stress or, alternatively, the shear velocity) were simulated for each particle diameter; values of $\tau / \tau_{cr}$ = 2, 2.5, and 3 were employed, where $\tau_{cr}$, the critical shear stress for incipient motion, is calculated using the explicit expression presented in the equation below (see García, 2008).

$$\tau_{cr} = 0.22\,\mathrm{Re}_p^{\ -0.6} + 0.06\exp(-17.77\,\mathrm{Re}_p^{\ -0.6}) \qquad (4\text{-}13)$$

**Minimum number of jumps**

Fig. 4-3 shows simulation results for $R_p$= 73, $\tau / \tau_{cr}$ = 2 with a total number of 517 jumps; therein, four mean values (symbols) with their respective two standard deviation error bars of non-dimensional particle jump height (left) and length (right) are shown. Each mean value represents the standard mean calculated for the first 100 jumps (out of 517); 150 jumps, 200 jumps; and finally for the complete set of jumps (517 hops). Before each mean value was calculated, the first 10 jumps were disregarded in order to eliminate the influence of initial conditions. The standard deviation was calculated with a similar methodology.

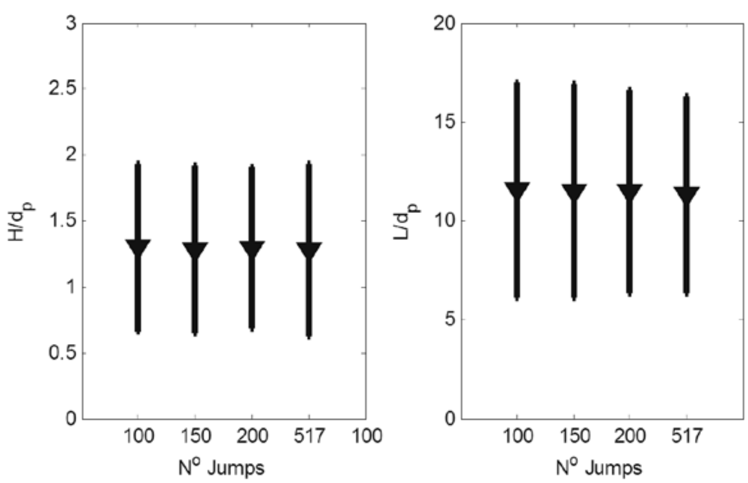


**Figure 4-3: Comparison of results of numerical simulations of a single saltating particle obtained with the model, when considering an increasing number of jumps. Left: dimensionless particle jump height (*H*). Right: dimensionless particle jump length (*L*). Symbols represent mean values, and vertical lines denote two standard deviations.** $\tau / \tau_{cr} = 2$**,** $R_p = 73$**.**

As it can be seen on the above figure, the mean jump height and length do not vary significantly when considering the first 100 jumps instead of 517 jumps, with the much smaller computational time of the former. The standard deviation for the jump length are slightly different (as expected), but that does not affect the comparison with data. Overall, the differences in mean values are within the errors in the collection of data.

**Comparison with data**

Fig. 4-4 and 4-5 show the average particle jump height and length predicted by the model compared to the Niño and García (1998a) and Lee and Hsu (1994) experimental datasets. The figures show good agreement.

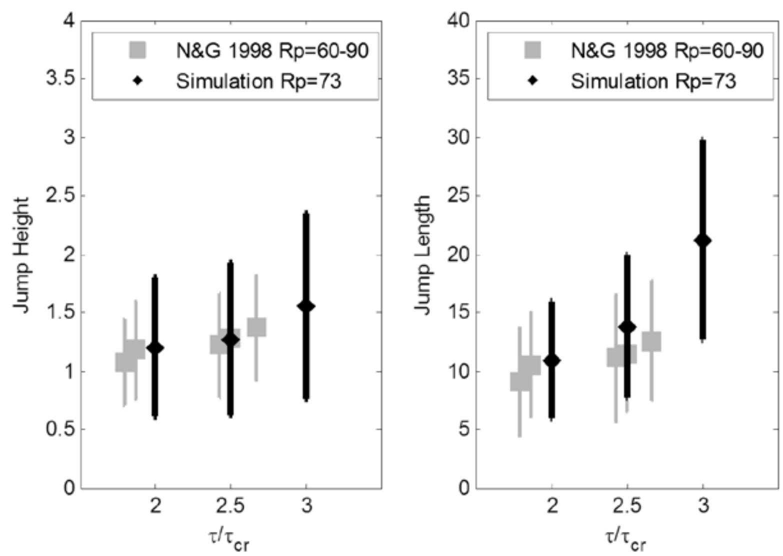


**Figure 4-4: Comparison of results of numerical simulations of a single saltating particle obtained with our Lagrangian model, with experimental data from Niño and García (1998a). Left: dimensionless particle jump height (*H*). Right: dimensionless particle jump length (*L*). Symbols represent mean values, and vertical lines denote two corresponding standard deviations.**

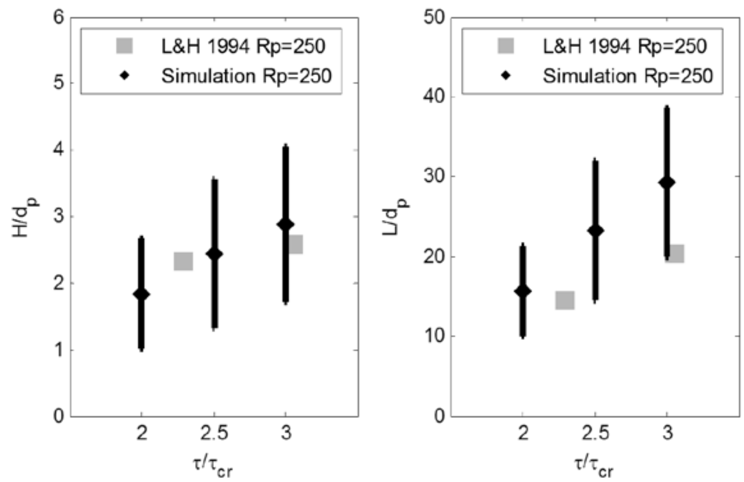


**Figure 4-5: Comparison of results of numerical simulations of a single saltating particle obtained with our Lagrangian model, with experimental data from Lee and Hsu (1994). Left: dimensionless particle jump height (*H*). Right: dimensionless particle jump length (*L*). Symbols represent mean values, and vertical lines denote two corresponding standard deviations. No information for standard deviation was found for the experimental data.**

### 4.3.2. Model Exploitation

Since one of the main objectives of this work is to contribute to the understanding of particle diffusion due to particle-particle collisions, the numerical model was manipulated to disregard particle scattering in the span-wise direction of the channel due to collisions with the wall.

A summary of the simulations performed is shown in Table 4-1. We carried out a total of 24 runs, grouped in 4 sets of runs. Each set was developed for the same initial sediment particle concentration, $C_p$, explicit particle Reynolds number, $R_p$, and either considering or disregarding inter-particle collisions.

For each set of runs, three flow conditions were employed, i.e., three values $\tau/\tau_{cr}$ were used, as before. Two explicit particle Reynolds numbers were simulated: $R_p = 73$ and $R_p = 250$, denoting particle diameters, $d_p$, of 0.69 mm and 1.57 mm, respectively, both within the range of sands. For the submerged particle specific gravity, a typical value of $R = 1.65$ (quartz) is used (García, 2008).

**Table 4-1: Characteristics of numerical simulations.**

| Run Set N° | $C_p$ | $R_p$ | $\tau / \tau_{cr}$ | Inter-particle Collisions |
|---|---|---|---|---|
| **1** | 0.13% | 73 | 2 / 2.5/ 3 | Yes/No |
| **2** | 0.13% | 250 | 2 / 2.5/ 3 | Yes/No |
| **3** | 2.33% | 73 | 2 / 2.5/ 3 | Yes/No |
| **4** | 2.33% | 250 | 2 / 2.5/ 3 | Yes/No |

The particle concentration refers to the volume occupied by particles in a well-defined initial volume of mixture (water and particles). It seems convenient to indicate a certain measure of spatial distribution of particles in order to assess the influence of this parameter on the trajectories of particles, including collisions. The boundaries of the initial volume were defined by the initial positions of the saltating particles and, then, we calculated the particle concentration by dividing the initial volume by the total volume occupied by the particles. Two different initial particle concentrations were simulated, $C_p = 0.13\%$ and $C_p = 2.33\%$ (see Table 4-1). It is worth pointing out that these concentrations correspond to somewhat non-dilute concentrations, if we follow the criteria for suspended sediment proposed by Jha and Bombardelli (2010).

The computational algorithm for the inter-particle collisions is activated when the distance between two particles is smaller than the sum of their radii. An example of the collision between two particles named as Particle 1 and Particle 2 of the same diameter is shown in Fig. 4-6. The figure depicts the change in trajectory of both particles after hitting the channel bed and after inter-particle collision. Particle 2 moves up after hitting the bottom wall and then it collides with Particle 1. The process is repeated three times before these particular sediment grains travel away from each other. A collection of snapshots summarizing the first inter-particle collision shown in Fig. 4-6, i.e., at $t = 0.888$ (dimensionless time), is presented in Fig. 4-7. The latter depicts step by step how Particle 1 (light colored sphere) approaches Particle 2 (dark colored sphere) after its collision with the wall.

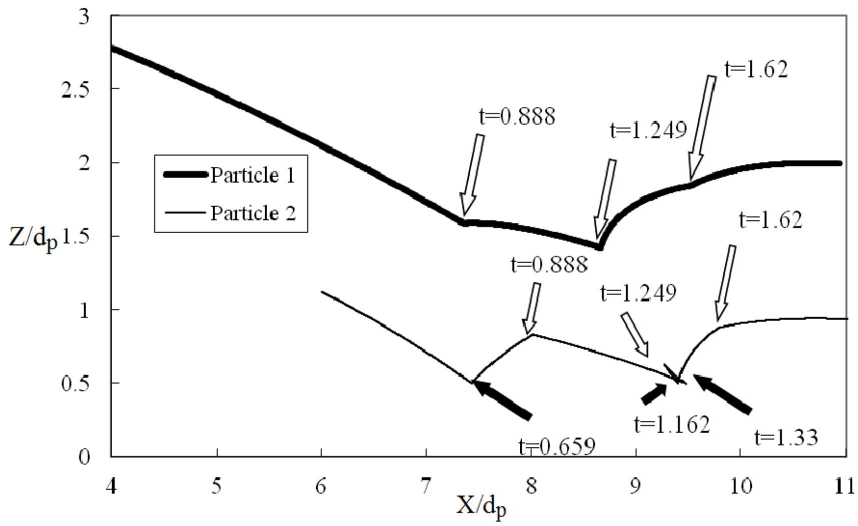


**Figure 4-6: Trajectories of two particles during particle-particle collisions. Both lines represent the position of the center of each sphere. Blank arrows depict the dimensionless time where the particles collide. Filled arrows represent the dimensionless time where Particle 2 hits the wall. $R_p$ = 73 (adapted from González, 2008).**

It is expected that inter-particle collisions may cause an increase of particle scattering, since the particle original direction of movement is suddenly modified when colliding with another particle. This path modification may occur in one, two, or all three directions, since collisions may cause the particle to move away or towards the bed, towards the positive or negative span-wise direction, and it may also accelerate or decelerate the particle movement in the stream-wise direction. This effect is generated due to the transfer of momentum during the collision. When two particles collide, the transfer of momentum will depend on the velocity magnitude and direction that each particle has before the collision, their rotation, and the contact point between colliding particles. In our simulations, particles were assumed to lose kinetic energy, during the collision, due to friction and inelastic effects. These effects are represented through the friction and restitution coefficients, as mentioned in previous paragraphs. Displays of particle scattering in 3D and in plan view are shown in Fig. 4-8 and 4-9, respectively.

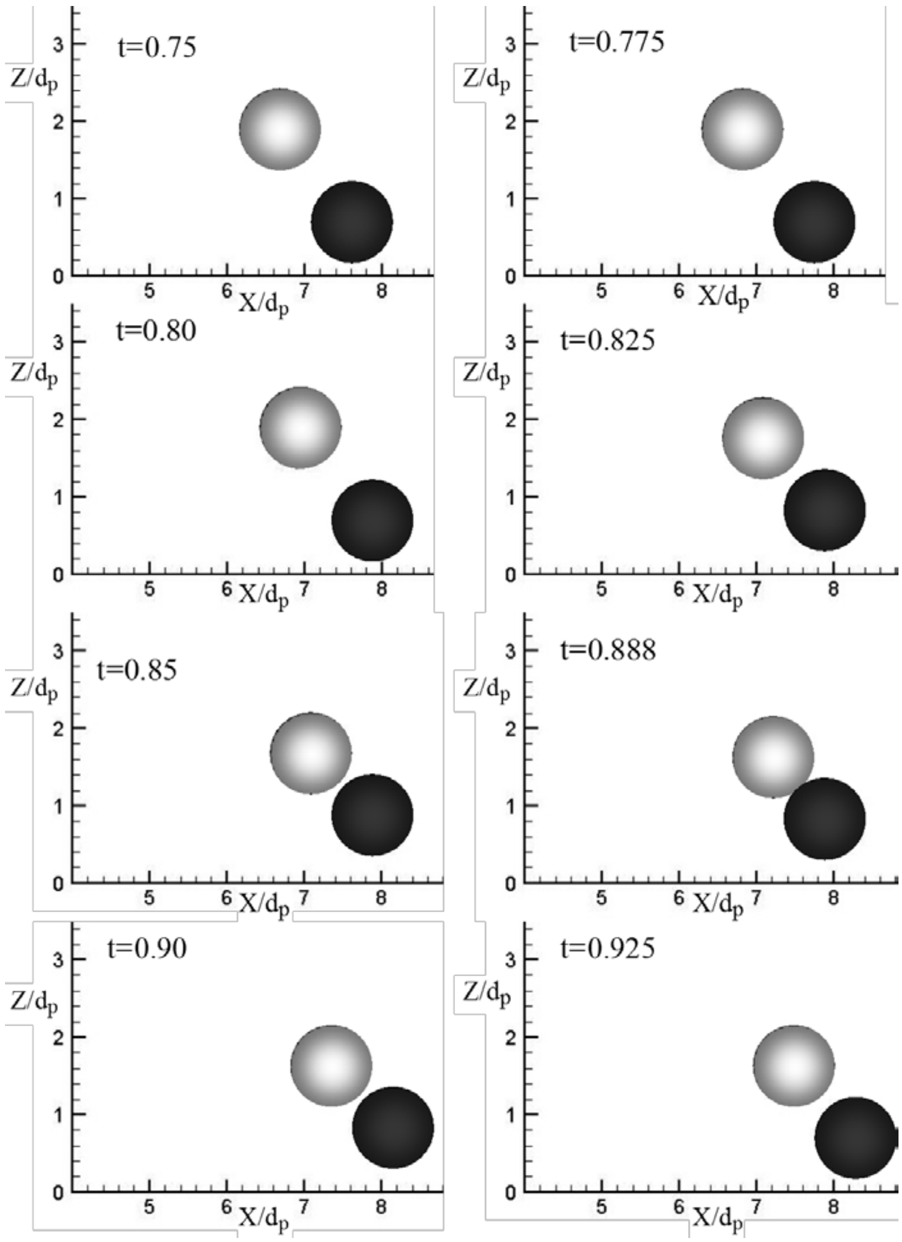


**Figure 4-7: Snapshots of particles trajectories, showing an inter-particle collision at dimensionless time t=0.888. Adapted from González (2008).**

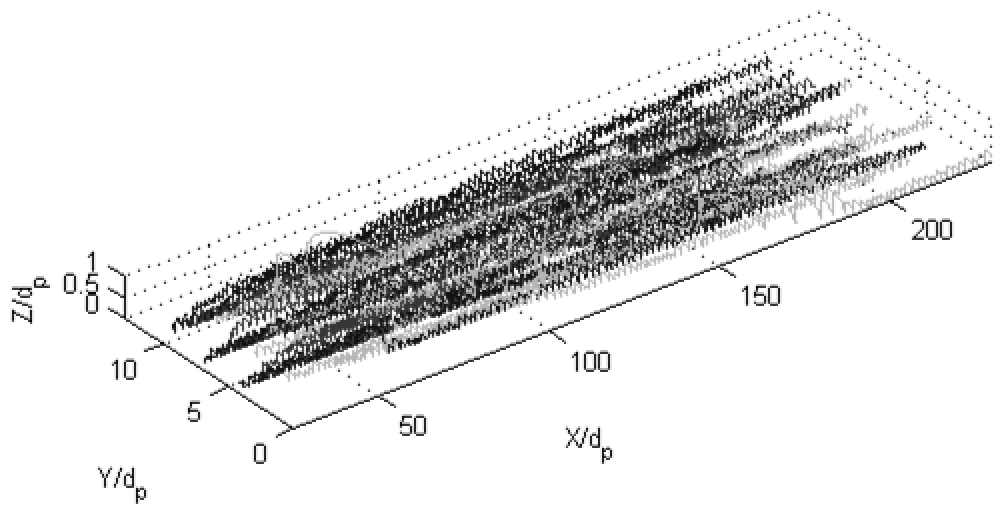


**Figure 4-8: Three-dimensional plot of particle trajectories (not to scale) for saltating and colliding particles. Figure shows the particle scattering in the span-wise and stream-wise directions caused by the collisions with the bed and between particles.** $C_p = 2.33\%$, $\tau / \tau_{cr} = 2$, $R_p = 73$.

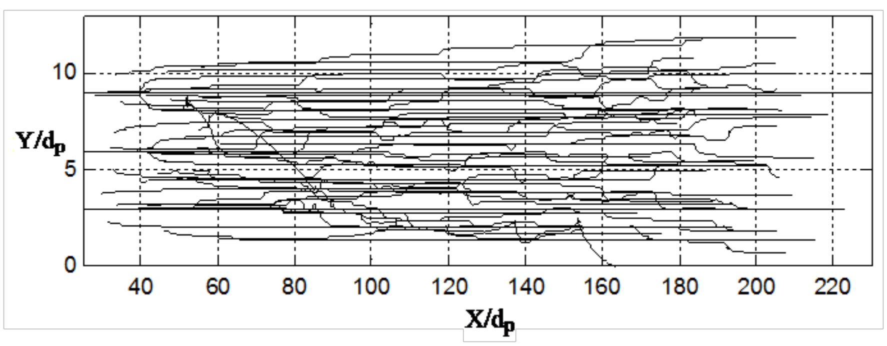


**Figure 4-9: Plan view of trajectories of saltating and colliding particles. Figure shows the particle scattering en the span-wise directions caused by the collisions between particles.** $C_p = 2.33\%$, $\tau / \tau_{cr} = 2$, $R_p = 73$.

The frequency of particle-particle collisions is expected to increase when the initial particle concentrations increases from 0.13% to 2.33%. This is shown in Table 4-2, where $R_{pb/pp}$ is the ratio of particle-bed to particle-particle collisions; $F_{pp}$ and $F_{pb}$ represent the particle-particle and particle-bed frequency of collision, respectively. All frequencies are calculated as the total number of collision events (either with the bed or among particles), in one run, divided by the complete dimensionless simulation time. Naturally, the frequency of particle collisions with the bed also increases at higher concentrations. It can also be observed from the table that $R_{pb/pp}$ decreases with increasing shear intensity.

**Table 4-2: Statistics of particle-particle and particle-bed collisions. $R_{pb/pp}$ indicates the ratio of particle-bed to particle-particle collisions; $F_{pp}$ and $F_{pb}$ represent the particle-particle and particle-bed frequency of collision, respectively. $R_p$=73.**

| $C_p$ | | 0.13 % | | | 2.33 % | |
|---|---|---|---|---|---|---|
| $\tau / \tau_{cr}$ | 2 | 2.5 | 3 | 2 | 2.5 | 3 |
| $R_{pb/pp}$ | 72.40 | 47.14 | 40.80 | 6.74 | 6.69 | 4.46 |
| $F_{pp}$ | 0.14 | 0.18 | 0.19 | 4.51 | 4.12 | 5.31 |
| $F_{pb}$ | 9.91 | 8.68 | 7.89 | 30.42 | 27.57 | 23.71 |

Fig. 4-10 shows the comparison between simulations with and without inter-particle collisions for $C_p = 0.13\%$ and $R_p = 73$. In the figure, it is apparent that no significant difference is observed in the simulation results at low particle concentration, when comparing average particle jump heights and lengths. The same conclusion can be obtained from Fig. 4-11 for the same concentration and $R_p = 250$. However, for higher particle concentrations, relatively sizable differences between simulation results with and without collisions appear for higher shear stresses, as shown in Fig. 4-12 (as expected). To test this hypothesis a Wilcoxon rank sum test was carried out. The distribution of the jump height and jump lengths for the data with and without particle-particle collisions is non normal, and therefore for non normal distributions the Wilcoxon rank sum test is used to perform a two-sided rank sum test of the null hypothesis that data of any two vectors (comparing jump heights and lengths with and without collisions) have equal medians, against the alternative that there is statistical evidence of significant difference. According to the test the medians of jump heights with and without collisions for a shear stress ratio of 3, at the 5% significance level, indicates that the medians are significantly different. The same test was undertaken for jump lengths with and without collisions for a shear stress ratio of 3, and it was also found that the medians are significantly different.

According to Fig. 4-12, disregarding inter-particle collisions for a particle concentration of $C_p = 2.33\%$ does not cause significant errors for shear stress ratios of $\tau/\tau_{cr} = 2$. Some differences can be noticed at $\tau/\tau_{cr} = 2.5$ in both, average particle jump height and length. However, when $\tau/\tau_{cr}$ is increased to 3, relatively sizable differences can be seen between simulation results, where the average particle jump height and length are smaller than the simulation results without considering collisions among particles. Moreover, when looking at the standard deviation (vertical line) for the highest shear stress ratio, the simulation with particle collisions shows a larger scatter of jump heights and lengths. This is expected, since an increase of particle-particle collisions will generate abrupt changes in trajectory of saltating particles, with the consequence of a larger range of lengths and heights in particle jumps.

When two particles collide there is an exchange of linear and angular momentum that may change the incoming particle rotation, particle velocity, and angle of trajectory right after the collision. During the simulations, these parameters were saved into an output file immediately before and after the collision, allowing for the calculation of the change in those variables. Fig. 4-13 depicts changes in the trajectory angle before and after collision between particles, for multi-particle simulations. Each tile refers to angles formed in the different planes. In general, the change in angle of trajectory due to particle-particle collision (Fig. 4-13) tends to decrease with increasing shear stress for both concentrations, in all axes. The change in angle of trajectory measured in the *Y-Z* plane shows noticeable differences between high and low particle concentrations in all three flow intensities. In this case, the change in angle appears to be larger for higher concentrations and lower shear stresses. When the shear stress increases up to a ratio of $\tau/\tau_{cr} = 3$, the difference becomes relatively small. This result suggests that the importance of collisions reduces with flow intensity. Also, a difference in the change in angle of trajectory can be seen for $\tau/\tau_{cr} = 2.5$ in the *X*-*Z* plane. However, this change does not follow a pattern with the increase in flow intensity.

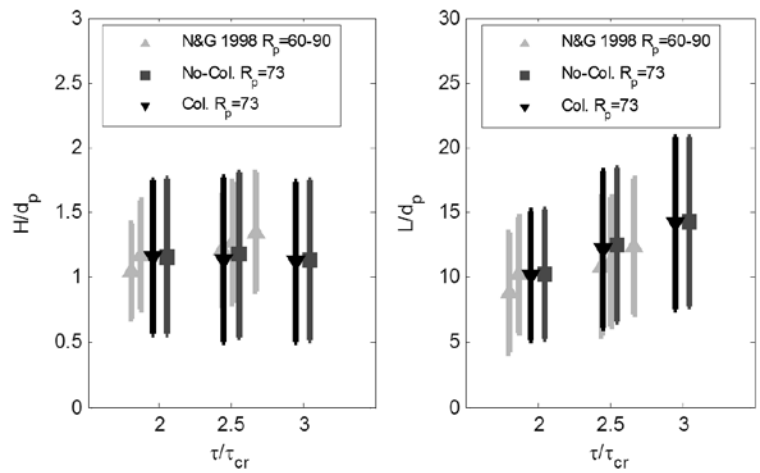


**Figure 4-10: Comparison of numerical results of simulations with (Col) and without (No-Col) particle-particle collisions, for $C_p = 0.13\%$ and $R_p = 73$. (Symbols representing simulation results have been slightly displaced from the simulated $\tau/\tau_{cr}$ ratio to avoid overlapping.) Vertical lines represent two standard deviations and solid (dark) symbols depict average values.**

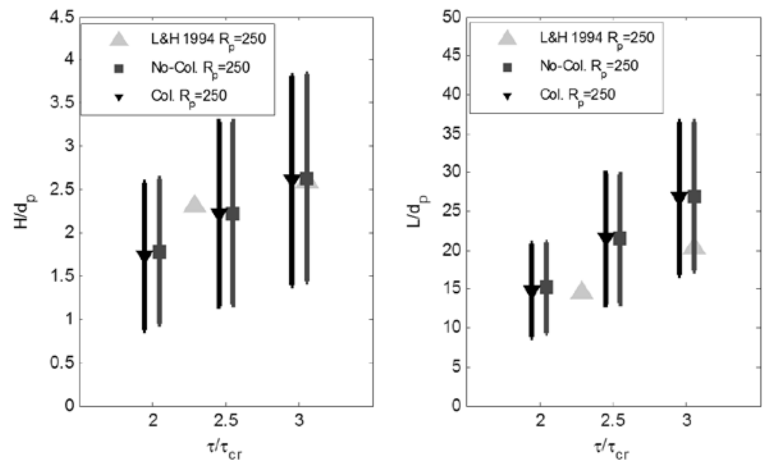


**Figure 4-11: Comparison of numerical results of simulations with (Col) and without (No-Col) particle-particle collisions, for $C_p = 0.13\%$ and $R_p = 250$. (Symbols representing simulation results have been slightly displaced from the simulated $\tau/\tau_{cr}$ ratio to avoid overlapping.) Vertical lines represent two standard deviations and solid (dark) symbols depict average values.**

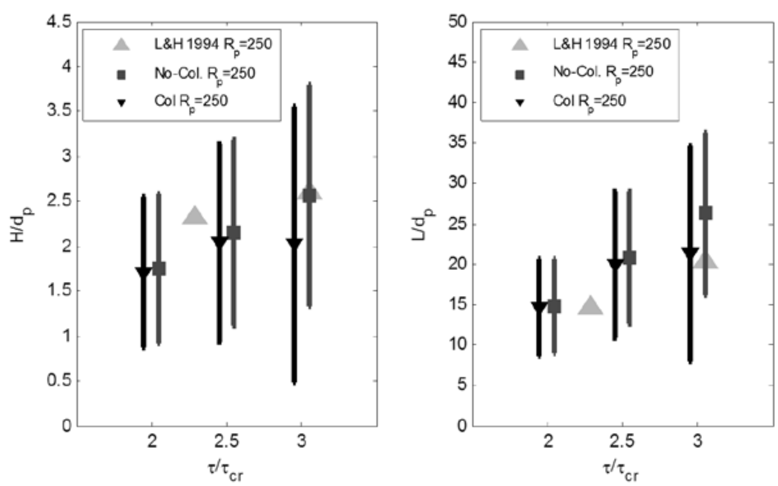


**Figure 4-12: Comparison of numerical results of simulations with and without particle-particle collisions, for $C_p = 2.33\%$ and $R_p = 250$. (Symbols representing simulation results have been slightly displaced from the simulated $\tau/\tau_{cr}$ ratio to avoid overlapping.) Vertical lines represent two standard deviations and solid (dark) symbols depict average values.**

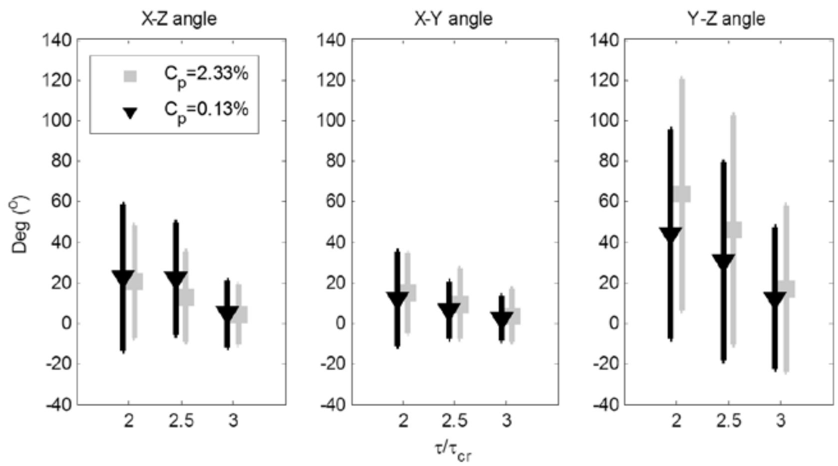


**Figure 4-13: Change in angle of particle trajectory due to particle-particle collisions, for multi-particle simulations. Comparison between $C_p = 0.13\%$ and 2.33% for $R_p = 73$. The angle differences presented correspond to the angles formed in the *X-Z* (left), *X-Y* (center) and *Y-Z* (right) planes. Symbols denote average values, and vertical lines denote two standard deviations.**

When examining the changes in particle velocity due to inter-particle collisions, the same pattern observed in Fig. 4-13 is apparent. According to the simulation results (Fig. 4-14), it is possible to notice higher changes in particle velocity at lower shear stresses. When shear stress increases, the change in particle velocity decreases, in all three directions. In the same manner, changes in particle rotation (Fig. 4-15) during collision behave similarly. We can also notice that these results on angle and velocity change are not especially sensitive to particle concentration (at least for the range of concentrations studied herein).

After analysis of the change in particle angle of trajectory, velocity and rotation in all three directions, it seems fair to hypothesize that at lower shear stresses, the transfer of momentum from particle to particle due to collision among sediment grains becomes important when compared to the transfer of momentum from the flow to the particle, hence notably changing the particle angle of trajectory, particle velocity and particle rotation in the colliding grains. However, the transfer of momentum due to inter-particle collisions is overcome by the momentum transfer from the flow to the particle when shear stress is sufficiently large. It is important to remark that changes seem to tend asymptotically to zero for increasing shear stress ratios (Figs. 4-13 to 4-15), reinforcing the explanation provided above.

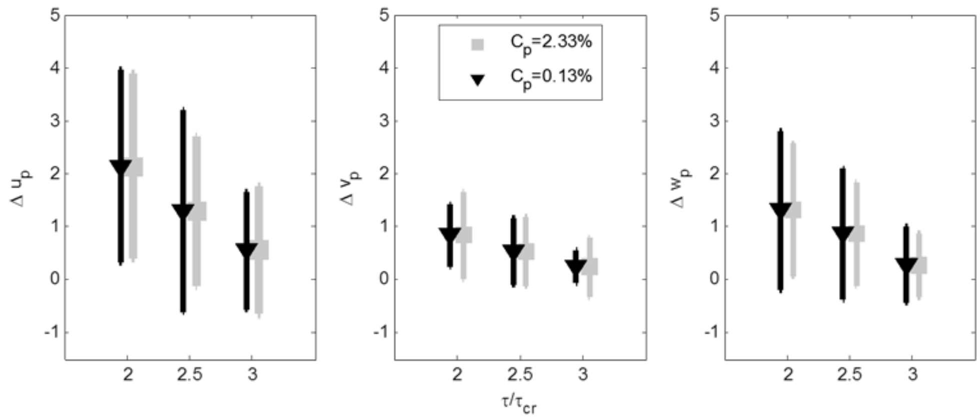


**Figure 4-14: Change in dimensionless particle velocity due to particle-particle collisions, for multi-particle simulations. Comparison between $C_p$ =0.13% and 2.33% for $R_p = 73$. $\Delta u_p$, $\Delta v_p$ and $\Delta w_p$ denote the change in dimensionless particle velocity in the stream-wise, span-wise and the wall-normal directions, respectively. Symbols represent average values, and vertical lines denote two standard deviations.**

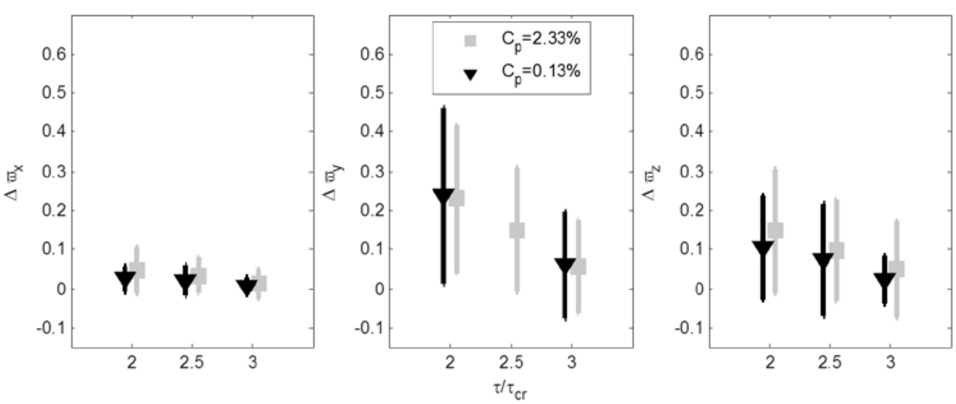


**Figure 4-15: Change in dimensionless particle angular velocity (particle rotation) due to particle-particle collisions, for multi-particle simulations. Comparison between $C_p$ =0.13% and 2.33% for $R_p = 73$. $\Delta\varpi_x$, $\Delta\varpi_y$ and $\Delta\varpi_z$ denote the change in angular velocity in the stream-wise, span-wise and the wall-normal directions, respectively. Symbols denote average values, and vertical lines denote two standard deviations.**

As previously mentioned, the numerical model was set up to avoid particle scattering in the transverse direction of the channel (span-wise direction) due to collisions with the wall. The main purpose of this was to isolate the effects of particle-particle collisions and to assess their influence in diffusion of saltating grains in the span-wise direction. Fig. 4-16 shows a dark colored sediment particle, which travels in saltation mode near the bed in collision course with another particle (light colored), with which it collides a second time later. Then, the dark colored particle heads towards a second particle, which is also light colored, colliding again two different times. Finally, the dark colored particle collides with the last particle (again light colored) further on in the *X*-axis.

The main purpose of Fig. 4-16 is to show changes in trajectory in the dark colored particle due to inter-particle collisions and, therefore, other particles are equally colored (light colored). In the first graph, from top to bottom, the dark colored particle denotes the typical hopping behavior every time it hits the wall. The second tile describes the behavior of the particle in the horizontal plane. The third and fourth tiles show the span-wise particle velocity, $v_p$, and an approximation to the acceleration component in the span-wise acceleration, $a_y$, of the dark particle before collision with the first light particle. The approximation to $a_y$ was calculated using the non-dimensional velocity change between time steps. When inter-particle collisions occur, changes in the dimensionless span-wise velocity and acceleration are important, while when collisions among particles are not present, particles tend to follow a constant trajectory in a direction parallel to the *X*-axis (if we disregard collisions with the bed, as done in this work), and possess a zero value for the particle velocity and acceleration, because of the effect of the unidirectional flow field. This suggests that particle-particle collisions cause a significant change in particle trajectory, introducing scattering in the span-wise direction. No clear correlation was found between features of the collisions and the other parameters (e.g., location, velocity and acceleration in the other axes). It is important to mention that the analysis above is valid when the effect of particle collisions with the bed, in the span-wise direction, is eliminated on purpose.

One way to corroborate the findings presented above is to mathematically express the scatter process of bed particles through the non-dimensional time evolution of the second order moment of particle position in the *X* and *Y* directions (see Fig. 4-17 and Fig. 4-18), as proposed by Nikora et al. (2001 and 2002) and Bialik et al. (2012). The latter can be expressed as:

$$\left\langle X'^2 \right\rangle = \alpha_x t^{2\gamma_x} \tag{4-14}$$

$$\left\langle Y'^2 \right\rangle = \alpha_y t^{2\gamma_y} \tag{4-15}$$

where $X$ and $Y$ are the stream-wise and span-wise coordinates of the saltating particle, respectively; $\left\langle X'^2 \right\rangle$ and $\left\langle Y'^2 \right\rangle$ are the time evolution of the second order moment of *X* and *Y*, respectively; $\alpha_x$ and $\alpha_y$ are constants; $X' = X - \left\langle X \right\rangle$, $Y' = Y - \left\langle Y \right\rangle$; and angular brackets denote ensemble averaging; the exponents $\gamma_x$ and $\gamma_y$ dictate the state of diffusion (Nikora et al., 2001 and 2002), namely sub-diffusion ($\gamma$ < 0.5), normal diffusion ($\gamma$ =0.5), super-diffusion ($\gamma$ > 0.5), and ballistic diffusion ($\gamma$ =1); while when $\gamma \approx 0$ it can be concluded that there is no diffusion or scattering on that particular direction.

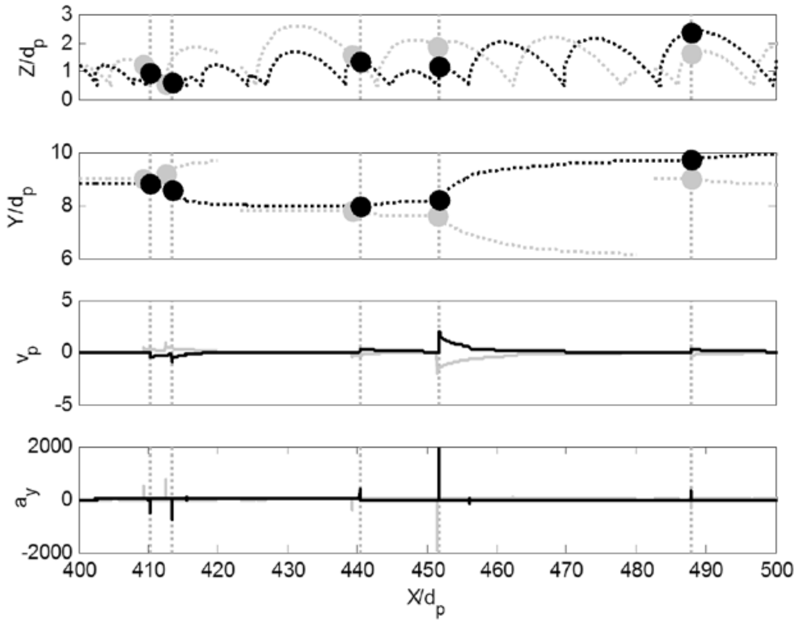


**Figure 4-16: Particle trajectories. Upper tile: elevation view. Second tile: plan view. Third tile: Particle span-wise dimensionless velocity. Fourth tile: Particle span-wise dimensionless acceleration. All parameters are dimensionless. Vertical dotted lines indicate the location of inter-particle collisions in the *X*-axis. $R_p$ = 73, $\tau / \tau_{cr}$ = 2.**

Particles start from different initial positions in all simulations presented herein. In order to analyze particle scattering, the differences in initial location of particles in the *X*-*Y* plane have been shifted to a unique release point. In this way, the calculations involving ensemble averaging of particle location and variance collapses to one single curve of data points, as shown in Figure 4-17 and Figure 4-178..

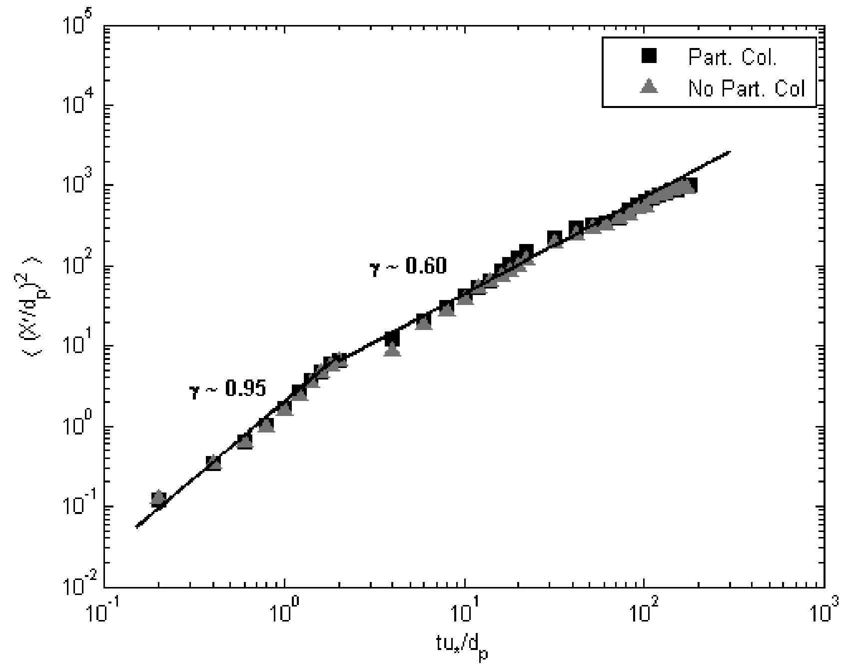


**Figure 4-17: Non-dimensional time evolution of the second order moment of particle position in the stream-wise (*X*) direction, for a simulation of concentration equal to $C_p = 2.33\%$, with and without particle-particle collisions. While the variance has been made dimensionless dividing it by $d_p^{\ 2}$, time has been multiplied by $u_* / d_p$. Solid lines indicate the slope of the curves. $R_p$ =73, $\tau / \tau_{cr}$ =2.**

In Fig. 4-17 and Fig. 4-18 the solid lines represent the time evolution of the second order moment of particle location in the stream-wise and span-wise directions of multi-particle simulations. Fig. 4-17 shows that there is no significant difference in scattering between simulations with and without particle-particle collisions in the stream-wise direction. Inter-particle collisions do not seem to affect the particle diffusion in the stream-wise direction significantly, when considering a logarithmic velocity profile and a unidirectional flow. However, this is not true when comparing diffusion in the span-wise direction with and without inter-particle collisions, as shown in Fig. 4-18. The last segment (to the right) of the diffusion plot shows a decline of the exponent, $\gamma \approx 0$, to a point where it is nearly zero, for the simulations without particle-particle collisions, indicating that there is no transverse particle diffusion in this simulation. Since the collisions of particles with the bed have been arranged not to cause any scattering in the span-wise direction, the only source of particle diffusion transverse to the flow is the inter-particle collision process, and Fig. 4-18 clearly shows this. The top curve of the figure denotes the particle diffusion when inter-particle collisions are considered in the simulation, and the respective slopes show values of $\gamma$ clearly different from zero. That is to say, particle-particle collisions alone are a significant source of particle dispersion in the span-wise direction, and it cannot be neglected when simulating particle saltation in the range of sands.

The light colored slope line in Fig. 4-18 shows the particle diffusion in the span-wise direction for a single particle as presented in Fig. 3.17b on Section 3.4.5 of this thesis (only the slope line for the intermediate range is shown for the sake of clarity). The contribution of particle-particle collisions to transverse particle diffusion is about a half of that caused by particle collisions with the wall, when comparing the $\gamma$ exponents for both slopes.

Results of Figures 4-17 and 4-18 are similar to those obtained by Nikora et al. (2001 and 2002) and Bialik et al. (2012), when disregarding entrainment effects for the latter work. In both figures, three segments differentiated by their slopes are observed. The first segment suggests a ballistic behavior ($\gamma_x = \gamma_y \approx 1$) in all cases (with and without collisions). The second segment denotes super diffusion in the stream-wise direction ($\gamma_x \approx 0.7$) for both cases of particle collision; it also suggests super diffusion in the span-wise direction ($\gamma_y \approx 0.6$), when including inter-particle collisions. Normal diffusion ($\gamma_y \approx 0.5$) is found in the span-wise direction where collisions among particles are not considered. The third segment shows sub-diffusion (although very close to normal diffusion) in the stream-wise direction ($\gamma_x \approx 0.47$) with and without inter-particle collisions, whereas in the span-wise direction the results show sub-diffusion and no diffusion at all for the cases with and without inter-particle collision, respectively

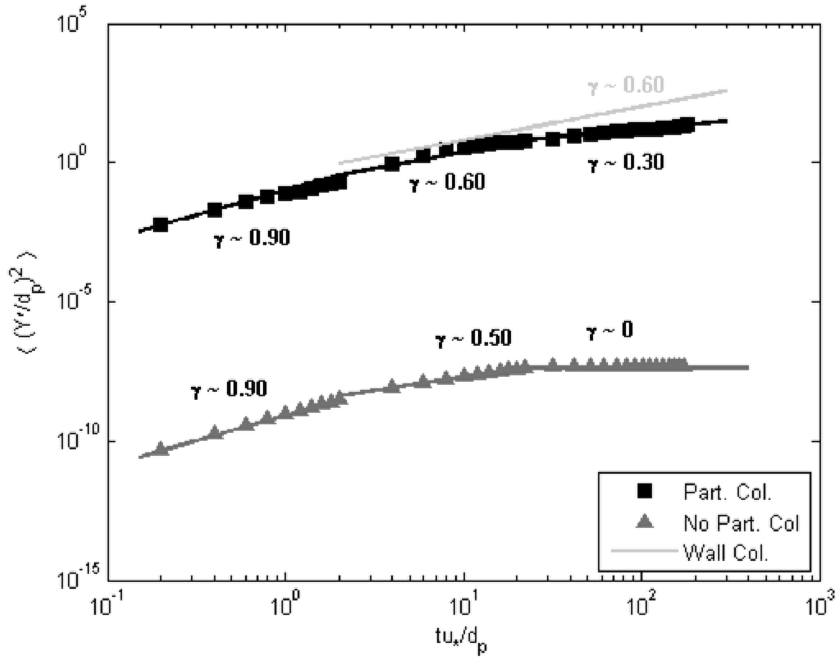


**Figure 4-18: Non-dimensional time evolution of the second order moment of particle position in the span-wise (*Y*) direction, for a simulation of concentration equal to $C_p$ =2.33%, with and without particle-particle collisions. While the variance has been made dimensionless dividing it by $d_p{}^2$, time has been multiplied by $u_* / d_p$. Solid lines indicate the slope of the curves. $R_p$ =73, $\tau / \tau_{cr}$ =2.**

. The results obtained herein regarding diffusion rates (i.e., the slopes) are similar to those obtained by Nikora et al. (2001 and 2002) and Bialik et al. (2012) in the stream-wise direction, whereas they are smaller in the last two segments for the span-wise direction. Since the model does not allow particle scattering due to collisions with the wall in the span-wise component, results in this direction are expected to differ with those by Nikora et al. and Bialik et al.

# CHAPTER 5

# A REVIEW OF RECENT ADVANCES IN THE COMPUTATION OF THE BASSET (HISTORY) FORCE

## 5.1. INTRODUCTION

Multi-phase flows are abundant in natural environments as well as man-made devices. They appear, for instance, in air-water flows past spillways in dams (Amador et al., 2006; Bombardelli et al., 2011), pneumatic transport of solids in the mining industry, sediment transport in streams and rivers (García, 2008; Bombardelli and Jha, 2009), and solid particle-air flows in the atmosphere (Crowe et al., 2011). Consequently, they have become important subject matters in diverse branches of science and engineering (Drew and Passman, 1999; Bombardelli and Chanson, 2009; Crowe et al., 2011). Multi-phase flows are constituted by a carrier phase (water or air), in which there are either bubbles (in case of water) and/or solid particles, which form the "disperse phase." In general, either bubbles or solid material are called "particles."

In order to numerically predict the behavior of multi-phase flows, it is often required to formulate mass and momentum equations for each of the phases separately (Drew and Passman, 1999; Prosperetti and Tryggvason, 2007; Bombardelli and Jha, 2009; Crowe et al., 2011). A common multi-phase, mathematical approach is to follow each particle in a so-called Lagrangian description. In this description, whereas the conservation of mass of the disperse phase becomes enforced automatically (because the motion of each particle is addressed explicitly (Drew and Passman, 1999; Crowe et al., 2011)), a momentum equation needs to be provided for the particles. To that end, a version of second Newton's law is employed, adapted to represent particles of finite size. Historically, one of the early approaches for such equation is the so-called Basset-Boussinesq-Oseen (BBO) expression, valid for Reynolds numbers much smaller than unity for a particle slowly accelerating in a still fluid. This equation included three forces: Stokes drag, added (virtual) mass and Basset. However, when considering a small rigid spherical particle moving also in low Reynolds numbers in non-uniform unsteady flow, the equation presented by Maxey and Riley (1983) has been widely used. The equation of Maxey and Riley (1983) is as follows:

$$m_p \frac{d\vec{u}_p}{dt} = m_f \frac{D\vec{u}_f}{Dt} - \frac{m_f}{2}\left(\frac{d\vec{u}_p}{dt} - \frac{D\vec{u}_f}{Dt}\right) - 6\pi a\rho\nu\left(\vec{u}_p - \vec{u}_f\right) + \left(m_p - m_f\right)\vec{g}$$

$$- 6a^2\rho\sqrt{\pi\nu}\int_{t_0}^{t} \frac{1}{\sqrt{t-\tau}}\left(\frac{d\vec{u}_p}{d\tau} - \frac{d\vec{u}_f}{d\tau}\right) d\tau \qquad (5\text{-}1)$$

In the above equation $\vec{u}_p$ and $m_p$ are the velocity vector and mass of the particle, respectively; $\vec{u}_f$ and $m_f$ represent the velocity vector and mass of fluid "excluded" by the particle; $t$ is the time coordinate; $a$ is the particle radius; $\rho$ depicts the density of fluid; $\vec{g}$ represents the acceleration of gravity vector; and $\tau$ is a dummy integration variable. The expression $d/dt$ denotes the time derivative following the moving particle, whereas $D/Dt$ indicates the time derivative following a fluid parcel. The terms on the right-hand side of Eq. (5-1) represent the following forces: pressure gradient of the undisturbed flow, virtual (added) mass, Stokes drag, submerged weight, and the Basset (history) force. The original Maxey and Riley equation includes second-order terms known as the Faxén terms, which work as correction for the curvature of the velocity profile (Crowe et al., 2011). The Faxén terms are neglected in Eq. (5-1) since they are usually smaller than other terms (Niño and García, 1994). Whereas those forces related to the pressure gradient and gravity are easy to understand from a physical standpoint, the forces of virtual mass and Basset are less evident. The virtual mass force is associated with the work needed from the moving particle to accelerate the fluid displaced by its body when translating to a new position; the name "added mass" refers to the fact that this force is equivalent to the effect of adding an extra mass in the accelerating particle (Crowe et al., 2011). The Basset term accounts for the temporal delay in the development of the boundary layer surrounding the particle's surface as a consequence of changes in the relative velocity (Crowe et al., 2011; Michaelides, 2006; Bombardelli et al., 2008). Armenio and Fiorotto (2001) found that the Basset force is important when the particle Reynolds number ($Re_p = w_s a/\nu$, where $w_s$ represents the particle fall (limit) velocity, and $\nu$ depicts the kinematic viscosity of the fluid) is of the order or smaller than 1, for a large range of density ratios.

Different variants of the Maxey and Riley equation have been developed in recent decades in order to account for particle motions in rivers as bedload, which involve the extension of the expression to finite Reynolds numbers (Wiberg and Smith, 1985; Mei, 1994; Niño and García, 1994; Lukerchenko et al., 2006; Dorgan and Loth, 2007; Bombardelli et al., 2008; Moreno and Bombardelli, 2012). Their efforts consisted in both changing some forces to make them compatible with large Reynolds numbers, and in some cases adding new terms known to work relatively well outside of the creeping flow regime ($R_e \ll 1$). From the terms of Eq. (5-1), the quasi-steady drag force needs to be modified for finite Reynolds numbers (Dorgan and Loth, 2007). The Basset force that accounts for the unsteady drag can also be modified for Reynolds numbers larger than one, although there is no agreement among researchers on how to approach the problem (see section 5.2.1 for further discussion). As the Reynolds number increases, the drag becomes non-linear. In the latter case the drag force can be rewritten in terms of the drag coefficient, $C_D$, for which there are several empirical or semi-empirical expressions available in the literature (i.e., Yen, 1992; González, 2008; Bombardelli and Moreno, 2012). The gradient of the velocity close to the bed of the stream may be significant enough to lift the particle; thus, a new term representing the lift force needs to be added. Another type of lift caused by the rotation of the moving particle needs to be considered through the addition of a term representing the Magnus force.

The Basset term can be presented in a generalized way, as follows:

$$F_B = 6a^2\rho\sqrt{\pi\nu}\int_{t_0}^{t} K(t-\tau)\frac{d}{d\tau}(f(\tau))d\tau \tag{5-2}$$

where $K(t-\tau)$ is called the Basset kernel and it is usually represented by the standard expression $1/\sqrt{t-\tau}$. The second factor, $f(\tau)$, is the relative velocity between phases.

In most cases, an analytical solution of Eq. (5-1) for low and finite Reynolds numbers is not possible, requiring the assistance of numerical techniques. Whereas most terms included in Eq. (5-1) can be computed using well-known numerical integration methods such as the standard Runge-Kutta, the integro-differential Basset term poses some challenges to its computation. First, the term includes the derivative of the relative velocity between the two phases, which is integrated since the beginning of times. This translates to high memory requirements to store the changes in relative acceleration of each simulated particle, and long integration times, reducing its applicability on disperse flow simulations when the motion of several hundred thousand particles need to be considered. Another important difficulty regarding the numerical integration of the Basset term is the singularity encountered when the upper limit is enforced in the integrand. The difficulties introduced by the Basset term have induced many authors to completely disregard it from the particle equation of motion, which may lead to large computational errors for small particles (Niño and García, 1998; Bombardelli et al., 2014).

This chapter critically compares major recent advances brought by four works: Dorgan and Loth (2007), Bombardelli et al. (2008), Hinsberg et al. (2011), and Daitche (2013), which involve a fractional derivative approach, window kernels and higher-order numerical integration schemes. The purpose of this chapter is to provide a general framework for the analysis of the Basset force for further developments. To this end, a test integral with a known analytical solution was used to compare the approaches by the last three contributions. Differences in CPU time of computation, rate of convergence and accuracy are analyzed.

## 5.2. RECENT DISCUSSIONS REGARDING THE BASSET FORCE

The latest advances in the computation of the Basset force focus on two different aspects: a) the validity of different kernels for the force to reflect the physics of the problem; b) numerical integration methods able to overcome the issues associated with the term. In what follows, we discuss these issues in detail.

### 5.2.1. Basset kernels

Regarding the first aspect, a kernel applicable to the finite Reynolds number range was proposed by Mei and Adrian (1992):

$$K(t-\tau) = \left\{(t-\tau)^{1/(2c_1)} + \left[\sqrt{\frac{\pi}{\nu}}\frac{\left|\vec{u}_f-\vec{u}_p\right|^3 (t-\tau)^2}{2\nu\, f_h}\right]^{1/c_1}\right\}^{-c_1} \tag{5-3}$$

$$f_h = \left[0.75 + c_2\left(\frac{2a\left|\vec{u}_f-\vec{u}_p\right|}{\nu}\right)\right]^3 \tag{5-4}$$

In Eqs. (5-3) and (5-4), $c_1 = 2$ and $c_2 = 0.105$. Other authors made modifications to the values of the two constants originally proposed by Mei and Adrian (Lawrence and Mei, 1995; Kim et al., 1998; Dorgan and Loth, 2007).

There is no agreement on the scientific community regarding whether the standard Basset term should change to account for turbulent effects in the non-linear drag range (Niño and García, 1994; Dorgan and Loth, 2007). The work of Mei and Adrian (1992) suggests that for short-time periods the decay rate of the Basset kernel is proportional to $t^{-1/2}$, as in the standard expression; however, for long-time periods the decay rate is proportional to $t^{-2}$ (a much faster decay rate). In their work, Mei and Adrian proposed a new kernel that takes into account the above by adding both decay expressions.

Lawrence and Mei (1995) found that the long-time decay rate was valid for a particle falling from rest to terminal velocity, but that it was different for particles stopping or experiencing flow reversal. Years later, Mordant and Pintot (2000) observed that the standard Basset expression was a good approximation to the history force for short periods at finite particle Reynolds numbers in line with previous findings but, more interesting, that the Basset force becomes negligible after a finite time interval. The work by Dorgan and Loth (2007) uses the kernel proposed by Mei and Adrian (1992) (Eqs. (5-3) and (5-4)) with a modification of the value of the constants ($c_1 = 2.5$ and $c_2 = 0.2$) for better approximation to experimental results. A comparison of the standard kernel with that proposed by Mei and Adrian (1992), and its modified version using the values proposed by Dorgan and Loth (2007) is shown in Fig. 5-1.

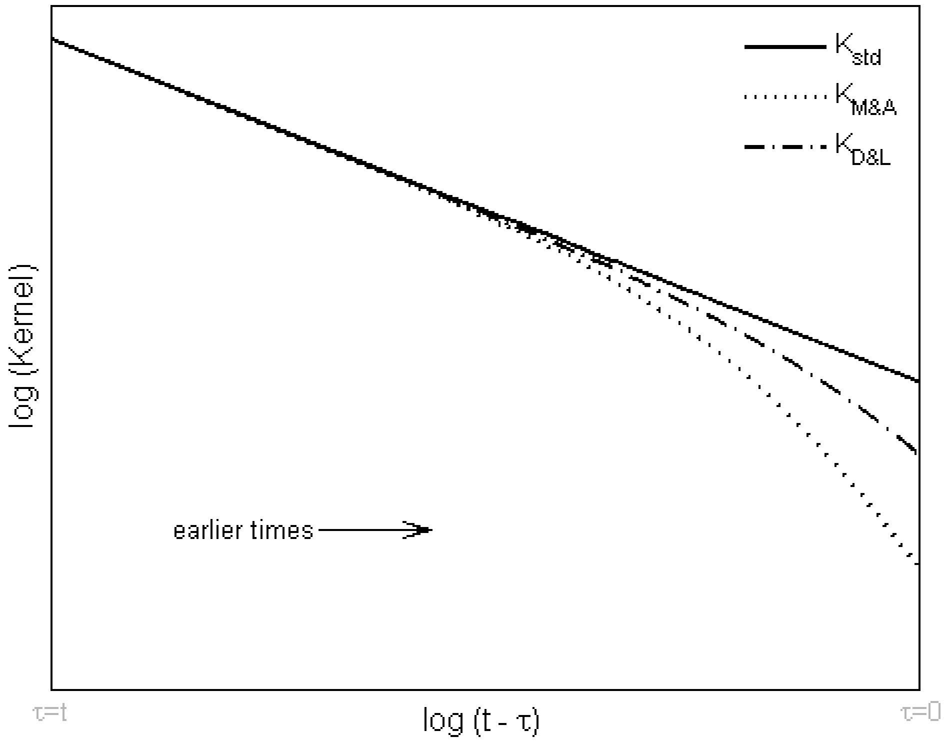


**Figure 5-1: Schematic comparison of the Basset standard kernel, $K_{std}$, versus the kernel proposed by Mei and Adrian (1992), $K_{M\&A}$, and a modified version of the Mei and Adrian kernel using the values proposed by Dorgan and Loth (2007), $K_{D\&L}$, as a function of time for $2a|\vec{u}_f - \vec{u}_p|/\upsilon = 10$. A value of $\upsilon$ equal to $10^{-6}$ $m^2/s$ was used. In the plot the more recent times (later times) are towards the left of the x-axis, while the earlier times are towards the right of the x-axis.**

### 5.2.2. Numerical approximation of the Basset term

In the past few years, attempts to overcome the difficulties in the integration of the Basset force have been made (Dorgan and Loth, 2007; Bombardelli et al., 2008; Hinsberg et al., 2011; Daitche, 2013). In this regard, several proposals have been put forward with the following goals: 1) to avoid the singularity of the integration process; 2) to reduce the computational time and memory requirements of the term; and 3) to increase the accuracy of the integration. The following sections discuss these three aspects in detail by comparing the different approaches taken by Dorgan and Loth (2007), Bombardelli et al. (2008), Hinsberg et al. (2011), and Daitche (2013).

#### 5.2.2.1. Singularity

Several methods have been developed to numerically solve cases of integration in which the integrand is singular. Press et al. (1992) discuss several open-formula quadratures (the integrand is not evaluated at the endpoints) to accomplish this, such as the second order Euler-MacLaurin method, and the second order Newton-Cotes scheme. The problem with these later quadratures is that they generate solutions with low temporal accuracy (O($h^{1/2}$)) and slow convergence (Bombardelli et al, 2008; Hinsberg et al., 2011; Daitche, 2013).

In order to circumvent the singularity problem, clever schemes need to be constructed to avoid the $t-\tau$ term from the denominator, or simply to change the upper limit of integration and separate the Basset term in two parts (Brush et al., 1964), while at the same time yielding solutions to the Basset integral with temporal accuracy larger than that obtained by the quadrature methods mentioned above. In the last few years, three works have devoted time to this issue (Bombardelli et al., 2008; Hinsberg et al., 2011; Daitche, 2013) with interesting results.

The work by Bombardelli et al. (2008) consists on a semi-derivative approach based on the work by Tatom (1988). Tatom noted that the Basset integro-differential equation may be transformed trough the Riemann-Liouville integral definition to a semi-derivative expression.

$$\int_{t_0}^{t} \frac{1}{\sqrt{t-\tau}} \frac{d}{d\tau}\big(f(\tau)\big) d\tau = \Gamma\left(\frac{1}{2}\right) \frac{d^{-0.5}\left(\frac{df(\tau)}{d\tau}\right)}{[d(t-t_0)]^{-0.5}} \tag{5-5}$$

where $\Gamma(\cdot)$ is the gamma function. The second factor on the right-hand side of the above equation corresponds to a fractional derivative of order ½, also known as the semi-derivative. This factor can be computed using the following series expansion for an arbitrary function $f$ (Oldham and Spanier, 1974):

$$\frac{d^q g}{[d(t-t_0)]^q} = \lim_{N\to\infty}\left\{\left(\frac{t-t_0}{N}\right)^{-q}\frac{1}{\Gamma(-q)}\sum_{k=0}^{N-1}\frac{\Gamma(k-q)}{\Gamma(k+1)}\,g\left(t-\frac{k(t-t_0)}{N}\right)\right\} \tag{5-6}$$

where $q = -0.5$ in this case, and $N$ is the number of terms considered in the semi-derivative sum. The paper by Tatom only notes the transformation given in Eq. (5-5), but it does not address either pure numerical results for the integral or its applications. Bombardelli et al. replaced expression (5-6) into Eq. (5-5) giving the final numerical approximation to the Basset force. The beauty of this approach lies on the use of the evaluation of the semi-derivative using a series expansion, which eliminates the $t-\tau$ term from the denominator, and hence solves the singularity problem.

Hinsberg et al. circumvented the singularity problem with the use of a trapezoidal-based method (the ordinary trapezoidal rule is not suited for singular integrals), by approximating the derivative of the relative velocity of the moving particle with a linear interpolant $P_1(t)$, to later integrate the product $K(t-\tau)P_1(\tau)$. The integral can be evaluated using the following expression:

$$\int_{t_0}^{t} K(t-\tau)\frac{d}{d\tau}\big(f(\tau)\big)d\tau = \frac{4}{3}\frac{d}{d\tau}\big(f(\tau_0)\big)\sqrt{h} + \frac{d}{d\tau}\big(f(\tau_N)\big)\frac{\sqrt{h}\left(N-\frac{4}{3}\right)}{(N-1)\sqrt{N-1}+\left(N-\frac{3}{2}\right)\sqrt{N}} +$$

$$\sqrt{h}\sum_{k=1}^{N-1}\frac{d}{d\tau}\left(f(\tau_k)\right)\left(\frac{k+\frac{4}{3}}{(k+1)\sqrt{k+1}+\left(k+\frac{3}{2}\right)\sqrt{k}}+\frac{k-\frac{4}{3}}{(k-1)\sqrt{k-1}+\left(k-\frac{3}{2}\right)\sqrt{k}}\right) \tag{5-7}$$

where $h$ is the time step for the discretization $\tau_k = t - kh$, with $k = 0, 1, 2, \dots, N$.

In turn, Daitche's methodology approximates only $f(\tau)$ with a polynomial (not the whole integral) and computes the resulting integral analytically through a trivial integration by parts which brings an initial condition. In this way the term causing the singularity $t - \tau$ does not appear in the denominator anymore. In that, Daitche was able to drop the derivative from the original kernel and take advantage of simplified numerical schemes with which a generalized procedure for quadrature schemes of higher order was established:

$$\int_{t_0}^{t} K(t-\tau)\frac{d}{d\tau}(f(\tau))d\tau + K(t-t_0)f(t_0) = \frac{d}{dt}\int_{t_0}^{t} K(t-\tau)(f(\tau))d\tau \tag{5-8}$$

The second term in the left-hand side of Eq. (5-8) assumes that the particle has an initial velocity different from that of the carrier fluid. When considering the same initial velocity for both, fluid and particle, the latter term vanishes. Finally, the quadrature scheme is as follows:

$$\int_{t_0}^{t} K(t-\tau)G(\tau)d\tau = \sqrt{h}\sum_{j=0}^{n}\beta_j^n\, G\left(\tau_{n-j}\right) + O(h^m)\sqrt{t-t_0} \tag{5-9}$$

where the order of approximation of the scheme will vary with the definition of the coefficient $\beta_j^n$. The definition of the coefficient is rather lengthy and for convenience it will not be shown in the present work. However, the format is similar to the following:

$$\int_{t_0}^{t} K(t-\tau)\frac{d}{d\tau}(f(\tau))d\tau = \sqrt{h}\sum_{k=0}^{n}\beta_j^n\, f(\tau_{n-k}) \tag{5-10}$$

$$\beta_j^n = \frac{4}{3}\begin{cases} 1 & ,k=0 \\ (k-1)^{3/2} + (k+1)^{3/2} - 2k^{\frac{3}{2}} & ,0<k<n \\ (n-1)^{3/2} - n^{\frac{3}{2}} + \frac{6}{4}\sqrt{n} & ,k=n \end{cases} \quad (5\text{-}11)$$

which is a second order solution. For further details of the coefficients with error orders $O(h^3)$ and $O(h^4)$ the reader is referred to Daitche (2013). In Eqs. (5-10) and (5-11), $\tau_k = t_0 + hk$; in turn, $n = (t - t_0)/h$ is the number of intervals used to approximate the integral.

Bombardelli et al.'s methodology can only be used with the standard kernel, while the approaches presented by Hinsberg et al. (2011) and Daitche (2013) can numerically approximate the Basset expression either using the standard or the modified kernel presented by Mei and Adrian (1992).

#### 5.2.2.2. Computational time and memory requirements of the Integration

Regarding the computational time associated with the integration of the Basset force, recent progress includes the so-called window-based approach. This is based on the idea according to which the acceleration of the particle at a given time loses correlation with previous values of acceleration as time passes by. The issue is how to express mathematically such loss of correlation. To the best of the author's knowledge, the completely independent works by Dorgan and Loth (2007) and Bombardelli et al. (2008) were the first works aiming at reducing the computation time by identifying a time window in which the Basset force needs to be considered. The window method presented by Dorgan and Loth (2007) was influenced by the findings of Mordant and Pintot (2000), who realized that the Basset force at finite Reynolds numbers was well represented by the creeping flow kernel (Eq. (5-1)) up to a finite time interval or time window, while after that period it decayed exponentially and eventually became negligible. This suggests that the Basset integral may be separated into two integrals partitioned by a finite time usually called $t_{win}$. The integral evaluating the earlier or older times will be defined by an approximation kernel, which will be called the tail kernel ($K_{tail}(t-\tau)$), different from the standard Basset kernel, while the integral evaluating later or more recent times will be defined by a window kernel ($K_{win}(t-\tau)$), where usually $K_{win}(t-\tau) = K(t-\tau)$:

$$\int_{t_0}^{t} K(t-\tau)\frac{d}{d\tau}(f(\tau))d\tau = \int_{t_0}^{t-t_{win}} K_{tail}(t-\tau)\frac{d}{d\tau}(f(\tau))d\tau + \int_{t-t_{win}}^{t} K_{win}(t-\tau)\frac{d}{d\tau}(f(\tau))d\tau \tag{5-12}$$

The main purpose implicit in Eq. (5-12) is to approximate the tail using a computationally cheap expression for $K_{tail}(t-\tau)$, which will translate in to a reduction in the use of computer memory and in computational time. Bombardelli et al. (2008), in turn, adopted a zero value for $K_{tail}$, assuming a complete lack of correlation of particle velocities with old ones in the transport of solids as bed-load. Since saltating particles move in a hopping motion, constantly colliding with the channel wall (Bombardelli et al., 2008; Moreno and Bombardelli, 2012; Bombardelli and Moreno, 2012) it seems reasonable to link $t_{win}$, the memory time period (called $T_{back}$ in Bombardelli et al. (2008)) to a specific number of jumps for which the window kernel is computed.

Fig. 5-2 sketches the numerical evaluation of the window and tail kernels. It is important to remember that the time evolution goes from right to left on Fig. 5-2, since the x-axis is evaluated as $t-\tau$. The approximation error of the window-based approach depends on the chosen $t_{win}$, the numerical integration method used to approximate the window kernel, and the numerical expression chosen to compute the tail kernel (Dorgan and Loth, 2007; Hinsberg et al., 2011).

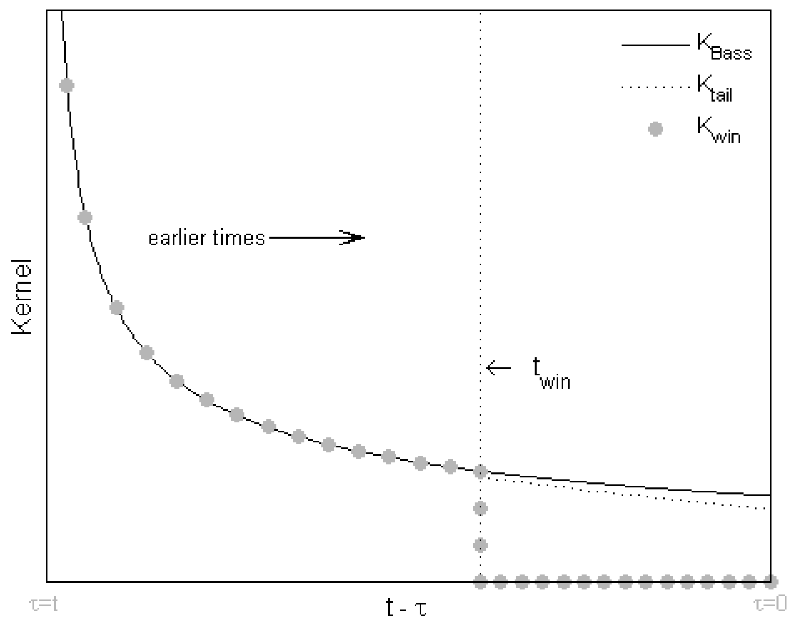


**Figure 5-2: Schematic of the numerical evaluation of the standard Basset kernel ($K_{Bass}$), window kernel ($K_{win}$) and tail kernel ($K_{tail}$) for an arbitrary $t_{win}$ as a function of time ($t - \tau$). The standard Basset kernel (solid black line) is approximated by the window kernel (grey circles), from $t$ up to $t - t_{win}$, and the tail kernel (broken black line) at times earlier than $t - t_{win}$. Modified from Dorgan and Loth (2007). As in Fig. 5-1, A value of υ equal to 10-6 m2/s was used. In the plot the more recent times (later times) are towards the left of the x-axis, while the earlier times are towards the right of the x-axis.**

Bombardelli et al. compared their results to the second Euler-Maclaurin summation formula and to the decomposition by Brush et al. (1964) method, using the Simpson quadrature, and found that the semi-derivative approach converged much faster than the other two, consequently reducing the computational time in about 20%. Applying the window-based method reported an improvement of the simulation time of 70-90% from the original run.

Hinsberg et al. (2011) applied a window-based approach through the use of less expensive functions to approximate $K_{tail}(t-\tau)$.

$$\int_{t_0}^{t} k(t-\tau)\frac{d}{d\tau}\big(f(\tau)\big)d\tau \approx \underbrace{\int_{t_0}^{t-t_{win}} K_{tail}(t-\tau)\frac{d}{d\tau}\big(f(\tau)\big)d\tau}_{EXPONENTIAL\ FUNCTIONS} + \int_{t-t_{win}}^{t} K_{win}(t-\tau)\frac{d}{d\tau}\big(f(\tau)\big)d\tau \qquad (5\text{-}13)$$

The numerical approximation of the integration of the tail kernel is carried out using a direct and a recursive term, based on exponential functions, as follows:

$$\int_{t_0}^{t-t_{win}} K_{tail}(t-\tau)\frac{d}{d\tau}\big(f(\tau)\big)d\tau = \sum_{i=1}^{m} a_i F_i(t) \qquad (5\text{-}14)$$

where $F_i(t)$ represents the contribution of the $i$-th exponential function, which is split into a direct ($F_{i=di}(t)$) and a recursive ($F_{i-re}(t)$) component.

$$F_i(t) = F_{i-di}(t) + F_{i-re}(t) \qquad (5\text{-}15)$$

in which:

$$F_{i-di}(t) = 2\sqrt{et_i}\, exp\left(-\frac{t_{win}}{2t_i}\right)\left\{\frac{d}{d\tau}\big(f(\tau_N)\big)\left[1-\varphi\left(-\frac{h}{2t_i}\right)\right] + \frac{d}{d\tau}\big(f(\tau_{N+1})\big) exp\left(-\frac{h}{2t_i}\right)\left[\varphi\left(\frac{h}{2t_i}\right)-1\right]\right\} \qquad (5\text{-}16)$$

$$F_{i-re}(t) = exp\left(-\frac{h}{2t_i}\right) F_i(t-\Delta t) \qquad (5\text{-}17)$$

where $a_i$ and $t_i$ are positive constants, and $\varphi(z) = \frac{e^z-1}{z} = 1 + \frac{1}{2}z + \frac{1}{6}z^2 + O(z^3)$. According to Hinsberg et al., the use of the recursive exponential functions for the tail kernel makes the calculation of the Basset integral very efficient, reducing the computational costs by more than an order of magnitude, while the memory requirements are reduced even further. Daitche (2013) presented a different approach without the use of a window-based method, although its implementation should be straightforward. No comparisons or explicit statements on computational time and memory savings are mentioned on Daitche (2013), since all the efforts are focused in obtaining highly accurate solutions (see next sub-section).

A comparison of the methods proposed by Bombardelli et al. (2008), Hinsberg et al. (2011), and Daitche (2013) with second and third order error are shown in Fig. 5-3. The different algorithms were coded in the FORTRAN 95 language and compared over CPU time in seconds. In order to perform the comparison, an arbitrary integral with an analytical known solution was selected, namely $\frac{d}{d\tau}\big(f(\tau)\big) = \cos(\tau)$, with the known analytical solution $\int_o^t \frac{\cos(\tau)}{(\sqrt{t-\tau})} d\tau = -\sqrt{2\pi}\left\{\cos(t)\, C\left[\sqrt{2/\pi}\sqrt{t-\tau}\right] + \sin(t)\, S\left[\sqrt{2/\pi}\sqrt{t-\tau}\right]\right\}_0^t$, where the Fresnel Integrals $C$ and $S$ are given by $C(\tau) = \int_o^\tau cos[(\pi z^2)/2]dz$ and $S(\tau) = \int_o^\tau sin[(\pi z^2)/2]dz$. The integral was evaluated at $t = 50\pi$. All methods were used to calculate the integral over the complete time domain (no window-based method was applied). Each computation was run 1000 times, and then the average results for CPU time, rate of convergence and accuracy of each method were obtained. Fig. 5-3 shows that the method proposed by Hinsberg et al. is the fastest, about one half of the time that takes the Bombardelli et al. approach, and one and two orders of magnitude faster than Daitche 2$^{nd}$ and 3$^{rd}$ order, respectively. This difference may be of importance when simulating thousands or even larger number of particles; however, the inclusion of tail kernels may render some of the comparisons moot.

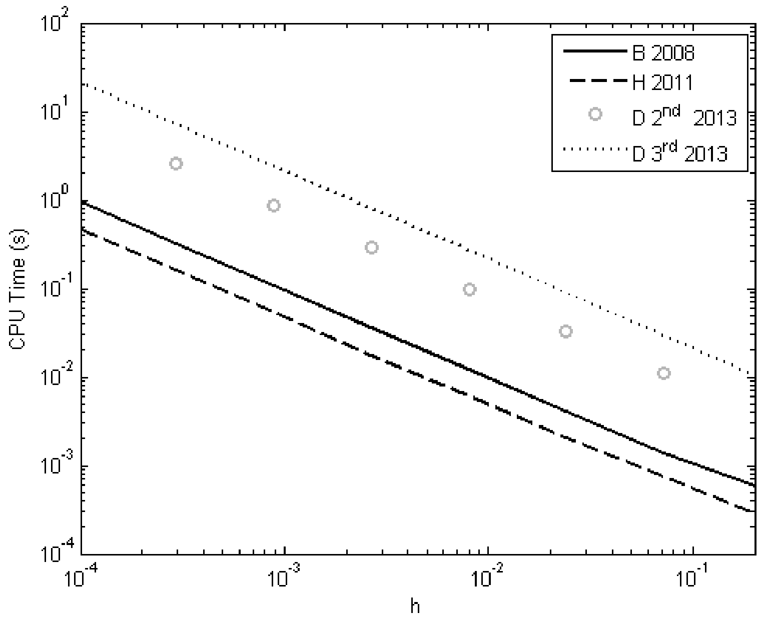


**Figure 5-3: Comparison of computational time elapsed as a function of time step (h). The time elapsed was measured in seconds as CPU time (built in function in Fortran 95) for four different methods: Bombardelli et al. (B 2008), Hinsberg et al. (H 2011), Daitche 2$^{nd}$ order error (D 2$^{nd}$ 2013) and 3$^{rd}$ order error (D 3$^{rd}$ 2013).**

### 5.2.2.3. Rate of Convergence and Accuracy

In the computation of the different terms present in the Maxey and Riley Equation (5-1), or those terms modified or added for higher Reynolds numbers, numerical methods such as the Runge-Kutta methods yield higher-order solutions, and therefore it would be desirable that the accuracy of the computation of the Basset integral gives solutions with at least second order error (Hinsberg et al., 2011). The semi-derivative method proposed by Bombardelli et al. (2008) yields solutions with temporal accuracy $O(h)$, where $h$ is the time step. Hinsberg et al. (2011) compared the convergence and relative error of their approach to the semi-derivative approach used by Bombardelli et al. In that, a test function providing a known analytical solution for the Basset integral was used, showing that Hinsberg et al. approach produces a smaller error than the semi-derivative approach. Furthermore, when increasing the number of points ($N$) the error becomes $O(h^2)$, which is an improvement from the semi-derivative method. Daitche (2013) presented a procedure to generate numerical schemes of arbitrary order (errors of $O(h^2)$ and higher) to compute the Basset integro-differential equation using quadratures.

Fig. 5-4 depicts a comparison of order of accuracy, using the same test integral from section 5.2.2.2, of the four analyzed methodologies. It seems important to mention that the coefficients proposed by Daitche for both 2nd and 3rd order approaches should be computed using quad precision (otherwise the 2nd and 3rd order are not achieved) and stored in double precision (to save computational time and memory).

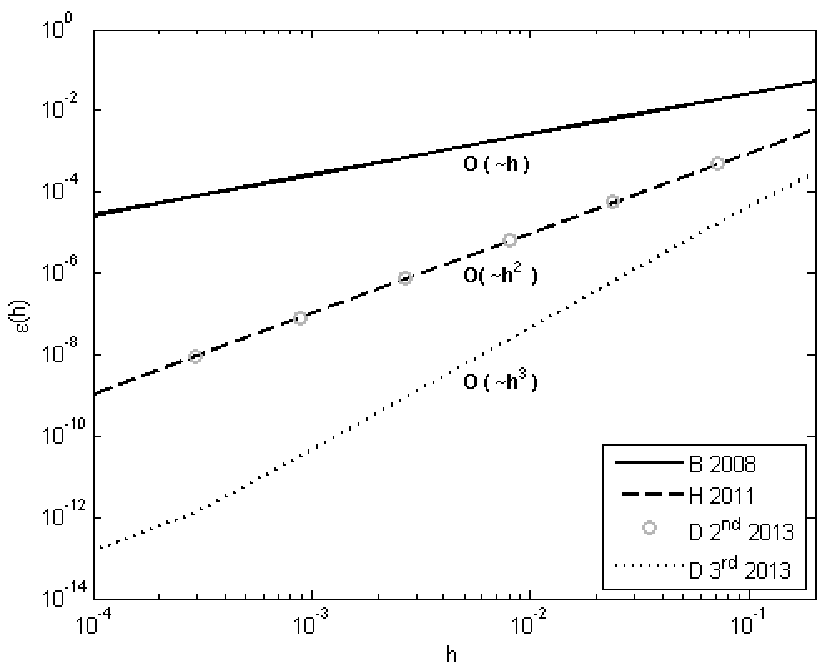


**Figure 5-4: Comparison of the order of accuracy for four different methods: Bombardelli et al. (B 2008), Hinsberg et al. (H 2011), Daitche 2nd order error (D 2nd 2013) and 3rd order error (D 3rd 2013). h depicts time step.**

With the information gathered from Figs. 5-3 and 5-4, it is possible to establish a graph that depicts the CPU time needed to compute the Basset term for a desired accuracy, depending on the methodology selected. This is depicted in Fig. 5-5. It can be clearly seen from the figure that the method proposed by Hisberg et al. (2011) is convenient no matter what the desired accuracy is.

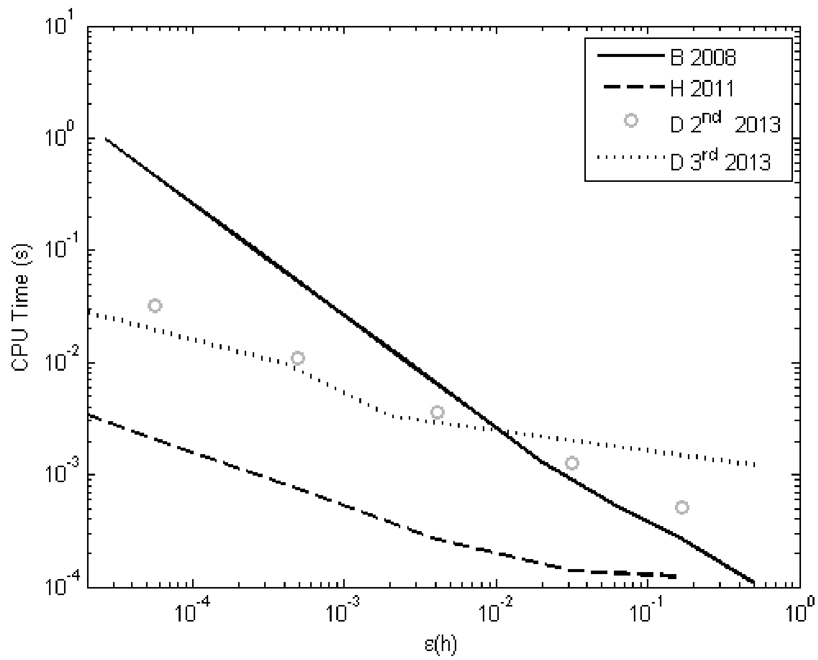


**Figure 5-5: Accuracy versus CPU time of computation for four different methods: Bombardelli et al. (B 2008), Hinsberg et al. (H 2011), Daitche 2nd order error (D 2nd 2013) and 3rd order error (D 3rd 2013).**

# CHAPTER 6

# SUMMARY AND CONCLUSIONS

This thesis showed the convenience of interpreting theoretical/numerical models for bed-load transport in streams as composed by three sub-models: a) a Lagrangian sub-model describing the particle motion with the fluid (i.e., a flight model); b) a rebound sub-model linking the particle velocity before and after the collision with the stream bed; and c) a realistic bed roughness (surface) representation. The model could also be extended to a multi-particle simulation (carried out in Chapter 4), including the effect of inter-particle collisions as done in González (2008) and Moreno and Bombardelli (2012).

This work presented a three dimensional sub-model for particle flight which extends the equations put forward by Niño and García (1994). This sub-model includes an equation for the particle angular velocity, an aspect disregarded in most models, but necessary to estimate the value of the Magnus force. This sub-model was paired with two rebound sub-models to compute the particle velocity after the collision with the wall, one proposed by Tsuji et al. (1985) and the other proposed by García and Niño (1992). Finally, to complete the simulation model, eight different bed-roughness representations were included. The first three bed-roughness sub-models (R1 to R3) have been used previously by different authors; the five remaining sub-models (R4 - R8) have been proposed for the first time in this thesis. These proposed surface roughness sub-models provided five different approaches to estimate the inclination plane of the point of contact between the moving particle and the bed. Although not exact, the criterion for comparison of runs based on an overlap index area showed to be an adequate tool for comparison of numerical and observed data.

Eight simulation scenarios (one for each bed-roughness sub-model) were tested and compared among themselves and against experimental data by Niño and García (1998a) and Lee and Hsu (1994). The results obtained were analyzed in detail from a physical/geometrical point of view for each $R_p$, separately, and a ranking was developed to find the models that would perform equally well for both particle sizes. According to the simulation results the best model was G2, which includes some level of dependence of $\theta_b$ on the vertical incidence angle $\theta_{in}$ through the estimation of $r_1/d_p$, which is the angle that controls the jump height and length, but no dependence of $\alpha_b$ on the lateral incidence angle $\alpha_{in}$, that mainly controls the transverse particle diffusion. This suggests that considering the lateral scattering as a purely random phenomenon gives the best approximation to experimental values. A better analysis may be carried out with new experimental values for $R_p$= 250, that would include information about the standard deviation of the main dimensionless variables ($H$, $L$, and $\overline{u}_p$). The results suggest that the sub-models for surface roughness proposed by Tsuji et al. (1985) and Sommerfeld (1992) are less representative for bed-load transport in streams. In this work it is also shown that by far the restitution ($e$) and friction ($f$) coefficients that allowed a closer approximation to experimental values in the overall, were the ones proposed by Schmeeckle et al. (2001) where $e$ = 0.65 and $f$ = 0.1. Also, this study has demonstrated the risks of using regressions from specific experimental tests for estimating the particle angular velocity for high values of the wall-friction (shear) velocity. In addition it was proven that the particle diffusion present in natural streams, rivers and channels for bed-load transport could be reproduced with our models, in agreement with the recent literature.

I would like to highlight the extensive assessment carried out in chapter 3 that evaluated many of the different aspects present in model approaches presented in literature on the subject of particle saltation. The use of forces commonly disregarded in simulations (Basset and Magnus), the use of a time dependent equation for particle angular velocity, the analysis of commonly used restitution and friction coefficients, a thorough analysis of the contribution and importance of each force in an average particle jump trajectory, and the evaluation of particle diffusion in the stream and wall-normal directions, make this dissertation the most extensive work analysis on the simulation of particle saltation yet published, with the hope to help future research on the matter.

Chapter 4 focuses on particle-particle collisions in saltation in the bed-load layer. The 3D Lagrangian theoretical/numerical model presented in Chapter 3 was set up to disregard particle scattering caused by particle collisions with the bed, in a way to isolate the effects of particle-particle collisions and to address their influence in diffusion of saltating grains. Model results were validated with available experimental data for two different sediment diameters, subjected to different flow intensities.

Results show no significant difference between simulations with and without inter-particle collisions for initial sediment concentrations of 0.13%, regardless of the particle diameter in terms of particle average jump height and length. However, when the initial sediment concentration increases to 2.33%, differences between simulations with and without inter-particle collisions at higher shear stresses become relatively important, as shown when comparing average particle jump heights and lengths.

Changes in particle angle of trajectory, particle velocity and particle rotation due to particle-particle collisions appear to be significant for the smaller shear stress ratios, while they become less important (close to zero) when the shear stress ratio is equal to 3 or larger. This suggests that at lower shear stress ratios the transfer of momentum due to collisions becomes important in relative terms, whereas when the shear stress ratio is increased, the transfer of momentum exerted by the flow to the particle overcomes that generated from particle collision.

Later, the simulations presented in Chapter 4 show that inter-particle collisions significantly introduce transverse diffusion, due to strong correlation of sudden changes in particle velocity and acceleration in the span-wise direction.

Finally in Chapter 5, we provided an overview and compared recent advancements in the computation of the Basset force. The focus was given to four recent papers on the subject, namely, Dorgan and Loth (2007), Bombardelli et al. (2008), Hinsberg et al. (2011), and Daitche (2013). *For the first time we presented a unified analysis of all relevant aspects of the problem*. All methods discussed efficiently overcome the singularity of the term.

Regarding the computational time and memory requirements to integrate the standard Basset term, our simulations show that the Hinsberg et al. approach yielded a good approximation to the analytical solution, using a test integral, requiring less CPU time. The issue is that in spite of the computational time of the approach and the accuracy of the numerical scheme employed, the reduction in computational time coming from the tail term can be of a large amount as opposed to the window term. Therefore gains in this aspect will highly depend on the application and the use of a tail kernel.

For the accuracy in the computation of the standard term, one important difference between all three methods is the order of accuracy of each approximation. While Bombardelli et al.'s approach leads to a first order error in the computation, the method by Hinsberg et al. leads to a second-order solution, and the Daitche approach sets grounds to obtain higher order solutions (second-order and higher). It has also been shown that no matter the desired accuracy required to compute the Basset term, the method proposed by Hinsberg et al. would require less time for computation.

Overall, all methods give better time accuracy than known quadratures ($O(h^{1/2})$), and in that regard they are all fine contributions.

The next step on this line of research would be to add a turbulent flow field, instead of using the law of the wall, and analyze the statistics of the jump and particle diffusion caused by the fluctuation of velocities in all three directions. Later on, a two-way coupled approach should be studied, where the flow affects the particle and the particles affect the flow, and study the changes in turbulence modulation for different flow intensities and sediment concentrations, and the effect of turbulence in particle-particle collisions.

# REFERENCES


Abbott JE, Francis JRD. 1977. Saltation and suspension trajectories of solid grains in water stream. *Philosophical Transactions of the Royal Society of London*. Series A, Mathematical and Physical Sciences **284:** 225-254.

Amador A, Sanchez-Juny M, Dolz J. 2006. Characterization of the nonaerated flow region in a stepped spillway by PIV. Journal of Fluids Engineering **128(6):** 1266-1273.

Armenio V, Fiorotto V. 2001. The importance of the forces acting on particles in turbulent flows. *Physics of Fluids* **13(8):** 2437-2440.

Auton TR, Hunt JCR, Prud'Homme M. 1988. The force exerted on a body in inviscid unsteady non-uniform rotational flow. *J. Fluid Mech.* **197:** 241-257.

Bialik RJ. 2011. Particle-particle collision in Lagrangian modelling of saltating grains. *Journal of Hydraulic Research* **49(1)**: 23-31.

Bialik RJ, Nikora VI, Rowiński PM. 2012. 3D Lagrangian modeling of saltating particles diffusion in turbulent water flow. *Acta Geophysica* **60(6):** 1639-1660.

Bombardelli FA, González AE, Niño YI. 2008. Computation of the particle Basset force with a fractional-derivative approach. *Journal of Hydraulic Engineering ASCE* **134(10):** 1513-1520. DOI: 10.1061/(ASCE)0733-9429(2008)134:10(1513).

Bombardelli FA, Jha S. 2009. Hierarchical modeling of the dilute transport of suspended sediment in open channels. *Environmental Fluid Mechanics* **9(2):** 207-235. DOI: 10.1007/s10652-008-9091-6.

Bombardelli FA, Chanson H. 2009, Progress in the observation and modeling of turbulent multi-phase flows. *Environmental Fluid Mechanics* **9(2):** 121–123.

Bombardelli FA, González AE, Moreno PA. 2010. Numerical simulation of spheres moving and colliding close to bed streams, with a complete characterization of turbulence. In: *Proceedings of River Flow 2010*: Braunschwig, Germany; 777-784.

Bombardelli FA, Meireles I, Matos J. 2011. Laboratory measurements and multi-block numerical simulations of the mean flow and turbulence in the non-aerated skimming flow region of steep stepped spillways. *Environmental Fluid Mechanics* **11:** 263-288.

Bombardelli FA, Moreno PA. 2012. Exchange at the bed sediments-water column interface. In *Fluid Mechanics of Environmental Interfaces*, Second Edition, Gualtieri C, and Mihailovic DT (eds). Taylor & Francis Group: London, Chapter 8, pp. 221-253.

Bombardelli FA, Moreno PA, González AE, Moniz R. 2014. Generalized algorithms for particle motion and collision with stream beds, *In Review*.

Brennen C. 2009. Fundamentals of multiphase flow. *Cambridge University Press*: New York, USA.

Brush JS, Ho HW, Yen BC. 1964, Acceleration motion of sphere in a viscous fluid. *Journal of Hydraulic Division* **90:** 149-160.

Chung TJ. 2002. Computational fluid dynamics, *Cambridge University Press*: Cambridge, UK.

Crowe C, Sommerfeld M, Tsuji M. 2011. Multiphase flows with droplets and particles, *CRC Press*: Boca Raton, Florida, USA.

Daitche A. 2013. Advection of inertial particles in the presence of the history force: Higher order numerical schemes. *Journal of Computational Physics* **254:**,93-106.

Davidson PA. 2005. Turbulence: An introduction for scientists and engineers. Oxford University Press, Oxford, UK.

Dorgan A, Loth E. 2007. Efficient calculation of the history force at finite Reynolds numbers. *International Journal of Multiphase Flows* **33:** 833-848.

Drake TG, Shreve RL, Dietrich WE, Whiting PJ, Leopold LB. 1998. Bedload transport of fine gravel observed by motion-picture photography. *Journal of Fluid Mechanics* **192**: 193-217.

Drew DA, Passman SL. 1999. Theory of Multicomponent Fluids, *Springer*: Berlin, Germany.

Duan J, Barkdoll B, Fan S, Kumpp C, McAnnally B, Papanicolaou T, Scott S, Wang S, Wu W, Ying X. 2004. Computational modeling of sediment transport processes. *Journal of Hydraulic Engineering,* ASCE **130(7):** 3-5.

Einstein HA. 1950. The bed-load function for sediment transportation in open channel flow. *US Department of Agriculture*. Technical Bulletin Nº 1026: Washington D.C.

Engelund F, Hansen E. 1967. A monograph on sediment transport in alluvial streams. *Monograph Denmark Technical University*. Hydraulic Lab. Denmark.

Francis JRD. 1973. Experiments on the motion of solitary grains along the bed of a water-stream. *Proceedings of the Royal Society of London*. Series A, Mathematical and Physical Sciences **332:** 443-471.

García M, Niño Y. 1992. Lagrangian description of beadload transport by saltating particles. In: *Proceedings of the 6$^{th}$ IAHR International Symposium on Stochastic Hydraulics*: Taipei, Taiwan; 259-266.

García MH. 2008. Sedimentation engineering: processes, measurements, modeling, and practice, *ASCE Manuals and Reports on Engineering Practice N° 110*: Reston, Virginia, USA.

González, AE, Bombardelli FA, Niño YI. 2006. Towards a direct numerical simulation (DNS) of particle motion near the bed. In: *Proceedings of River Flow 2006*: Lisbon, Portugal; 799-806.

González AE, Bombardelli FA, Calo VM, Niño YI. 2007. Simulation of particle motion close to a rigid wall. In: *ASME Applied Mechanics and Materials Conference, McMat 2007*: University of Texas, June 3-7.

González AE. 2008. Coupled numerical modeling of sediment transport near the bed using a two-phase flow approach. *Ph.D. Thesis, University of California, Davis*; 188.

Gordon R, Carmichael JB, Isackson FJ. 1972. Saltation of plastic balls in a "one-dimensional" flume. *Water Resources Research* **8(2):** 444-459.

Graf WH. 1971. The hydraulics of sediment transport, *McGraw-Hill Book Company*: New York, USA.

Greimann BP, Muste M, Holly F. 1999. Two phase formulation of suspended sediment transport. *Journal of Hydraulic Research*. **37(4):** 479-500.

Hanratty TJ, Theofanous T, Delhaye J, Eaton J, McLaughlin J, Prosperetti A, Sundaresan S, Tryggvason G. 2003. Workshop Findings. *International Journal of Multiphase Flow* **29:** 1047–1059

Harada E, Gotoh H. 2006. Influence of sand shape to vertical sorting under uniform flow condition. In: *Proceedings of River Flow 2006:* Lisbon, Portugal; 853-858.

Hu C, Hui Y. 1996. Bed-Load transport. II. Stochastic characteristics. *Journal of Hydraulic Engineering ASCE* **122:** 255-261.

Isaacson E, Keller HB. 1966. Analysis of numerical methods. *Dover Publications, Inc.*: New York.

Iversen JD, White BR. 1982. Saltation threshold on Earth, Mars and Venus. *Sedimentology* **29:** 111-119.

Jha SK, Bombardelli FA. 2010. Toward two-phase flow modeling of nondilute sediment transport in open channel. *Journal of Geophysical Research-Earth Surface* **115**: F03015.

Julien PY. 2010. Erosion and sedimentation, Second Edition, *Cambridge University Press*: Cambridge, UK.

Kartushinsky A, Michaelides E. 2004. An analytical approach for the closure equations of gas-solid flows with inter-particle collision. *International Journal of Multiphase Flow* **30:** 159-180. DOI: 10.1016/j.ijmujltiphaseflow.2003.10.007.

Kim I, Elghobashi S, Sirignana WB. 1998. On the equation for spherical-particle motion: effect of Reynolds and acceleration numbers. *Journal of Fluid Mechanics* **367:** 221-253.

Kundu PK, Cohen IM. 2008. Fluid mechanics, 4th Edition, *Academic Pres*, San Diego; California, USA.

Lawrence CJ, Mei R. 1995. Long-time behavior of the drag on a body in impulsive motion. *Journal of Fluid Mechanics* **283:** 307-327.

Lee HY. 1993. Investigations of the particle saltating process near the channel bed. *Unpublished MS Thesis, National Taiwan University*: Taiwan.

Lee HY, Hsu IS. 1994. Investigation of saltating particle motions. *Journal of Hydraulic Engineering ASCE* **120:** 831-845.

Lee HY, Chen YH, You JY, Lin T. 2000. Investigations of continuous bed load saltating process. *Journal of Hydraulic Engineering ASCE* **126(9):** 691-700.

Lee HY, You JY, Lin YT. 2002. Continuous saltating process of multiple sediment particles. *Journal of Hydraulic*, ASCE **128(4):** 443-450.

Lee HY, Lin YT, You JY, Wang HW. 2006. On three-dimensional continuous saltating process of sediment particles near the channel bed. *Journal of Hydraulic Research* **44(3):** 374-389.

Lin SY, Chin YH, Hu JJ, Chen YC. 2011. A pressure correction method for fluid-particle interaction flow: Direct-forcing and sedimentation flow. *International Journal for Numerical Methods in Fluids* **67(12):** 1771-1798.

Lin SY, Chin YH, Wu CM, Lin JF, Chen YC. 2012. A pressure correction-volume of fluid method for simulation of two-phase flows. *International Journal for Numerical Methods in Fluids* **68(2):** 181-195.

Loth E, Dorgan AJ. 2009. An equation of motion for particles of finite Reynolds number and size. *Environ. Fluid Mech.* **9(2):** 187-206. DOI: 10.1007/s10652-009-9123-x.

Lukerchenko N, Chara Z, Vlasak P. 2006. 2D Numerical model of particle-bed collision in fluid-particle flows over bed. *Journal of Hydraulic Research IAHR* **44(1):** 70-78.

Lukerchenko N, Piatsevich S, Chara Z, Vlasak P. 2009a. 3D Numerical model of spherical particle saltation in a channel with a rough fixed bed. *J. Hydrol. Hydromech.* **57(2):** 100-112. DOI: 10.2478/v10098-009-0009-x.

Lukerchenko N, Piatsevich S, Chara Z, Vlasak P. 2009b. Numerical model of spherical particle saltation in a channel with a transversely tilted bed. *J. Hydrol. Hydromech.* **57(2):** 182-190. DOI: 10.2478/v10098-009-0017-x.

Lukerchenko, N. 2010. Discussion of “Computation of the particle basset force with a fractional-derivative approach” by F. A. Bombardelli, A. E. González, and Y. I. Niño, *Journal of Hydraulic Engineering*, ASCE, **136(10):** 853-854.

Maxey MR, Riley JJ. 1983. Equation of motion for a small rigid sphere in a nonuniform flow. *Physics of Fluids* **26:** 883-889.

Matsumoto S, Saito S. 1970a. On the mechanism of suspension of particles in horizontal pneumatic conveying: Monte Carlo simulation based on the irregular bouncing model. *Journal of Chemical Engineering of Japan* **3:** 83-92.

Matsumoto S, Saito S. 1970b. Monte Carlo simulation of horizontal pneumatic conveying based on the rough wall model. *Journal of Chemical Engineering of Japan* **3:** 223-230.

Mei R, Adrian RJ, Hanratty T. 1991. Particle dispersion in isotropic turbulence under Stokes drag and Basset force with gravitational settling. *Journal of Fluid Mechanics* **225:** 481-495.

Mei R, Adrian RJ. 1992. Flow past a sphere with an oscillation in the free-stream velocity and unsteady drag at finite Reynolds number. *Journal of Fluid Mechanics* **237:** 323-341.

Mei R. 1994. Flow due to an oscillating sphere and an expression for unsteady drag on the sphere at finite Reynolds number. *Journal of Fluid Mechanics* **270:** 133-174.

Michaelides EE. 2006. Particles, bubbles and drops: Their motion, heat and mass transfer, World Scientific Publishing Co: Hackensack, New Jersey, USA.

Mordant N, Pintot JF. 2000. Velocity measurement of a settling sphere. *European Physical Journal B* **18:** 343-353.

Moreno PA, Bombardelli FA, González AE, Calo VM. 2011. Three dimensional model for particle saltation close to stream beds, including a detailed description of the particle interaction with turbulence and inter-particle collisions. In: *Proceedings of World Environmental and Water Resources Congress,* ASCE 2011: Palm Springs, CA, USA; 2075-2084.

Moreno PA, Bombardelli FA, 2012. 3D numerical simulation of particle-particle collisions in saltation mode near stream beds. *Acta Geophysica* **60**: 1661-1688.

Nikora V, Heald J, Goring D, McEwan I. 2001. Diffusion of saltating particles in unidirectional water flow over rough granular bed. *Journal of Physics A: Mathematical and General* **34(50)**: L743-L749.

Nikora V, Habersack H, Huber T, McEwan I. 2002. On bed particle diffusion in gravel bed flows under weak bed load transport. *Water Resources Research* **31(6)**: 1081.

Niño Y, García M, Ayala L. 1994. Gravel Saltation. 1. Experiments. *Water Resources Research* **30 (6):** 1907-1914.

Niño Y, García M. 1994. Gravel saltation. 2. Modeling. *Water Resources Research* **30(6):** 1915-1924.

Niño Y, García M. 1998a. Experiments on saltation of sand in water. *Journal of Hydraulic Engineering ASCE* **124(10):** 1014-1025.

Niño Y, García M. 1998b. Using Lagrangian particle saltation observations for bed-load sediment transport modelling. *Hydrological Processes* **12:** 1197-1218.

OldhamY, Spanier M. 1974. The fractional calculus, *Academic*: New York, USA.

Parker G. 2004. 1D sediment transport morphodynamics with applications to rivers and turbidity currents, e-book, *Natl. Cent. For Earth Surf. Dyn.*: Minneapolis, Minn. (Available at http://hydrolab.illinois.edu/people/parkerg/)

Press WH, Teukolsky SA, Vetterling WT, Flannery BP. 1992. Numerical recipes, Cambridge University Press: New York, USA.

Prosperetti A, Tryggvason G. 2007. Computational Methods for Multiphase Flow, *Cambridge University Press:* Cambridge, UK.

Rubey WW. 1933. Settling velocities of gravel, sand and silt particles. *Am. J. Sci*. **25:** 325-338.

Sagan C, Bagnold RA. 1975. Fluid transport on Earth and aeolian transport on Mars. *Icarus* **26:** 209-218.

Schmeeckle M, Nelson J, Pittlick J, Bennett J. 2001. Interparticle collision of natural sediment grains in water. *Water Resources Research* **37:** 2377-2391.

Schmeeckle MW, Nelson JM. 2003. Direct numerical simulation of bedload transport using a local, dynamic boundary condition. *Sedimentology* **50:** 279-301.

Scotti A. 2006. Direct numerical simulation of turbulent channel flows with boundary roughened with virtual sand paper. *Physics of Fluids*. **18:** 031701.

Sekine M, Kikkawa H. 1992. Mechanics of saltation grains II. *Journal of the Hydraulic Division ASCE* **104:** 1303-1321.

Shabani B, Yeganeh A, Wang SSY. 2005. Two-phase flow simulation of bed-load transport in three dimension with MBS-3D model. In: *Proceedings of the XXXI IAHR Congress*. Seoul, South Korea.

Shen N, Tsuji T, Morikawa Y. 1989. Numerical simulation of gas-solid two-phase flow in horizontal pipe. *Japan Society of Mechanical Engineering* **55:** 2294.

Shiller L, Naumann A. 1933, Uber die grundlegenden Berechungen bei der Schwerkraftautbereitung. *Ver. Deut. Ing.* **77:** 318-325.

Sommerfeld M. 1992. Modelling of particle-wall collisions in confined gas-particle flows. *International Journal of Multiphase Flow* **18:** 905-926.

Sommerfeld M, Huber N. 1999. Experimental analysis and modelling of particle-wall collisions. *International Journal of Multiphase Flow* **25:** 1457-1489.

Takeuchi K. 2004. Importance of sediment research in global water system science. In: *Proceedings of the 9th International Symposium of River Sedimentation*: Yichang, China, Vol. (1-4): 10-18.

Tanaka T, Tsuji Y. 1991. Numerical simulation of gas-solid two-phase flow in a vertical pipe: On the effect of inter-particle collision. In: D. Stock, Y. Tsuji, J. Jurewizc, M. Reeks, and M. Gautam, eds., *Gas-Solid Flows*, FED-121, ASME; 123-128.

Tatom FB. 1988. The Basset term as a semi-derivative. *Applied Scientific Research* **45:** 283-285.

Thorne CR, MacArthur RC, Bradley JB. 1988. The physics of sediment transport by wind and water. *Collection of hallmark papers by R. A. Bagnold. American Society of Civil Engineers*.

Tsuji Y, Oshima T, Morikawa Y. 1985. Numerical simulation of pneumatic conveying in a horizontal pipe. *KONA* **3:** 38-51.

Tsuji Y, Morikawa T, Tanaka T, Nakatsukasa N, Nakatani M. 1987. Numerical simulation of gas-solid two-phase flow in a two-dimensional horizontal channel. *International Journal of Multiphase Flow* **13:** 671-684.

Tsujimoto T, Nakagawa H. 1983. Stochastic study on successive saltation by flowing water. In: *Proceedings of the 2nd International Symposium on River Sedimentation*: Beijing, China; 197-201.

Turton R, Levenspiel O. 1986. A short note on the drag correlation for spheres. *Powder Technology* **47:** 83-86.

van Hinsberg MAT, Boonkkamp JHMT, Clercx HJH. 2011. An efficient, second order method for the approximation of the Basset history force. *Journal of Computational Physics* **230(4):** 1465-1478.

Wang H, Fan W, Yun C. 2004. Indicators and impact analysis of sediment from the Changjiang Estuary and East China Sea to the Hangzhou Bay. *Acta Oceanologica Sinica*. **23(2):** 297-308.

White BR. 1982. Two-phase measurements of saltating turbulent boundary layer flow. *International Journal of Multiphase Flow* **8:** 459-473.

Wiberg P, Smith JD. 1985. A theoretical model for saltating grains in water. Journal of *Geophysical Research* **90:** 7341-7354.

Yalin MS. 1977. Mechanics of sediment transport, Second Edition, *Pergamon Press Inc*: New York, USA.

Yamamoto Y, Potthoff M, Tanaka T, Kajishima T, Tsuji,Y. 2001. Large-eddy simulation of turbulent gas-particle flow in a vertical channel: effect of considering inter-particle collisions. *Journal of Fluid Mechanics* **442:** 303-334.

Yeganeh A, Gotoh H, Sakai T. 2000. Applicability of Euler-Lagrange coupling multiphase-flow model to bed-load transport under high bottom shear. *Journal of Hydraulic Research* **38 (5):** 389-398.

Yeganeh A, Shabani B, Gotoh H, Wang SSY. 2009. A three-dimensional distinct element model for bed-load transport. *Journal of Hydraulic Research* **47(2)**: 203–212.

Yen BC. 1992. Sediment fall velocity in oscillating flow. *Water resources Environmental Engineering Resources*. Report 11. Dept. of Civil Eng. University of Virginia.